Part III

Numerical Results: Investigation of the Hydrodynamics of Dense and Dilute Flows

Chapter 8

Dynamic Study of 2-D Bubbling Gas-Solid Fluidized Bed

In this Chapter[1] , finite element simulations of bubbling gas-solid fluidized beds were performed using the two-fluid granular temperature model. A study was carried out to establish the number of equations necessary to describe the dynamics of this fluidized bed. In order to investigate the bubbles' behavior and shape, several simulations were performed using differing numerical resolution. The main purpose of these investigations is to analyze, through numerical simulation, the dynamics of fluidized beds and to show how the application of deterministic chaos theory may be used to obtain the real dimensionality, or the number of degrees of freedom, of a simulated fluidized bed. Moreover, this type of statistical information can be used to quantify the similarities between experiment and simulation results.

[1]This chapter was published in the Powder Technology 128:56-77. C. C. Pain, S. Mansoorzadeh, J. L. M. A. Gomes, C. R. E. de Oliveira (2002), *A Numerical Investigation of Bubbling Gas-Solid Fluidized Bed Dynamics in 2-D Geometries*

8.1 Introduction

The widespread applications of fluidized beds in industry and the demand for improvements in fluidization efficiency have increased the need for accurate fluidization modelling. Although this poses a considerable challenge, due to the complexity of fluidization physics, computer hardware development and advances in numerical methods are now providing the necessary means to investigate the validity of several modelling approaches. By comparing numerical simulations with experiments, these modelling approaches can be validated and used with confidence to aid design and operation of fluidized beds.

Historically, the first attempt at modelling the hydrodynamics of fluidization was made by Davidson [194], who assumed that the solid phase surrounding the bubble is in irrotational motion. He used a potential function, for the solid phase, to simulate a spherical bubble. Following his work, various gas-particle modelling approaches were developed by other researchers such as Jackson [195], Soo [39] and Pritchett *et al.* [196]. However, these models lack experimental validation [74].

Numerical approaches to model the hydrodynamics of fluid particle systems can be divided into two categories: discrete and continuous models. The first comprise of tracking individual particles subjected to the hydrodynamic forces exerted by the fluid phase. For a dilute particle phase, particle-particle interactions can often be ignored. Hu [36] used an adaptive meshing two-dimensional finite element method in order to simulate a dilute fluidized bed without explicit particle interaction modelling - although particles were prevented from overlapping. On the other hand, for a dense particle phase, particle-particle interactions must be considered. The hard and soft sphere models were developed to model particle interactions [7, 32, 197]. Despite the significant computation time required to track individual particles in discrete models, researchers have not been discouraged from using this approach in fluidized bed applications [20, 102].

The two-fluid model (TFM) [39, 198], in which the fluid and particulate phases are assumed to behave like two inter-penetrating continua, are most commonly used for the fluidized bed simulations. A comparison between simulation results for formation of

a single bubble, obtained from discrete and continuous models, can be found in [197]. Further discussion of modelling the formation of bubbles can be found in [74, 199, 38, 40, 200, 201]. Some useful predictions have been made using the TFM approach. Kuipers *et al.* [40] and Gidaspow *et al.* [202] modelled the wall-to-bed heat transfer by measuring the effects of the rising bubbles on the thermal energy diffusion. Bouilard *et al.* [74] and Lyczkowski *et al.* [203] discussed the voidage distributions in fluidized beds with immersed obstacles. The similarity between the binary collisions of gas molecules and the particle-particle collisions led to the development of the granular temperature model [204, 205, 85, 135, 72, 83, 84, 206], which is based on the analogy with the kinetic theory of gases. Ding & Gidaspow [41] developed this model for two-phase flow by introducing the interstitial fluid and its associated interphase forces. Other fluidized bed numerical simulations, based on the granular temperature model, were described by Cao & Ahmadi. [207] and by Samuelsberg & Hjertager [136].

The chaotic characteristics of fluidized beds have been investigated by a number of researchers. Bouilard *et al.* [74] used deterministic chaos theory to analyze pressure fluctuations in a circulating fluidized bed (CFB). They calculated the correlation dimension of the bed, which was in the range of 1.5-1.9, indicating that the dynamics of the fluidized bed may be captured by a 2-D modelling method. Ryuji *et al.* [208] also used chaos theory to analyze the motions of bubbles and particles in a two dimensional gas-liquid-solid fluidized bed. They used a narrowed He-Ne laser beam to provide data from the experiment and to calculate the correlation dimension and Kolmogorov entropy as a function of the superficial gas velocity. They reported that the correlation dimension for the gas phase was higher than that for the solid phase. This implies that the gas phase has more degrees of freedom than the solid phase. Huilin *et al.* [43] also calculated the correlation dimension, the Kolmogorov entropy and the Lyapunov exponents of a CFB using the measured pressure and gamma-ray measured porosity time series. Using deterministic chaos theory they concluded that the dynamics of the CFB has two degrees of freedom and only two independent variables suggesting that the porosity and the relative velocity, can be useful to describe the dynamics of the system. Other related studies can be found in [209, 45, 74].

The chapter describes the results of the numerical modelling of gas-solid fluidized beds. This modelling is based on a transient, mixed finite element discretization described by Pain *et al.* [78] which is used to solve the multi-phase equations (see Chapter 2) with a discontinuous finite element representation of the granular temperature and continuity equations, and a Petrov-Galerkin discretization of the momentum equations. These set of equations are solved with an Arnoldi-iteration method. The resulting scheme has proved to be stable, which can allow the use of relatively large time steps (even if maximum packing is approached), and has attractive accuracy and efficiency features. The flexibility of the finite element approach enables simulations in geometrically complex beds to be performed.

The main aim of this chapter is to present the analysis of the dynamics of fluidized beds and to illustrate the application of chaos theory to investigate, numerically, the real dimensionality, or the number of degrees of freedom, of a fluidized bed. Comparisons between numerical results and experimental data, where available, are made, together with discussion of a number of phenomena which have been observed during the simulations, such as the rise and eruption of bubbles at the bed surface. The effect of the finite element computational grid is studied by investigating the convergence of the power spectrum with grid size. Chaos theory is used to analyze the bed behavior. The application of the chaos theory to estimate the extent of theoretical and experimental data needed to develop useful design and flow property correlations is also discussed.

A 2-D gas-solid fluidized bed is modelled, involving incompressible, isothermal mixtures with no phase exchange. In the studied case the gas (air), at room temperature, enters from the bottom of the bed and exits at the top, while the solid phase (spherical particles) circulates inside the bed. The physical properties of both phases and boundary conditions used in the numerical simulations are described at Section 8.2. Some numerical results and comparisons with experiments and an analysis of the features related to the first rising bubble which is released are discussed at Section 8.3. In Sections 8.4-8.6, the power spectra of the simulations are used to help establish grid convergence; in addition grid sensitivity is analyzed in the light of chaos theory, which may be used to characterize the flow regime. The effect of the walls on the flow and the vortex formation are analyzed

in Section 8.7.

8.2 Physical Characteristics and Boundary Conditions

The experimental fluidized bed configuration was designed by Lin *et al.* [3]. It comprises of a 13.8 cm diameter cylindrical column, containing glass Ballotini beads, with diameters in the range of 0.42-0.60 mm, and a static bed height of 11.3 cm. In this work, a particle diameter of 500 μm which density of 2.5 g.cm^{-3} was assumed. Inlet superficial velocity of air at room temperature was set as 64.1 cm.s^{-1} ; this value corresponds to 18% of the terminal velocity. A time step of 0.2 ms was adopted for the simulations. Five detectors were placed at different points within the bed to monitor the simulated instantaneous void fraction. The modelled fluidized bed and the detector positions are shown in Figure 8.1(a).

Boundary conditions applied to the modelled particulate and gas phases are summarized as follows. At the top of the domain, no normal flow and zero shear stress conditions were applied to the solid phase, all components of the stress tensor were set to zero. For the gas phase, zero shear stress was applied. This allowed gas to leave the domain unhindered. At the inlet boundary, the gas volume fraction was set to unity for inflowing material. At the vertical walls, a shear stress was prescribed, obtained from Blasius' equation [101], with a length scale equal to the static height of the bed. Wall boundary conditions for the particulate phase described in [80] were used in this simulation.

Samuelsberg & Hjertager [136] reported that results obtained from a modelling restitution coefficient of 0.995 for the glass beads matches experiments. On the other hand, Cody *et al.* [210] and Goldschmidt *et al.* [103] stated a value, for this coefficient, from 0.9 to 0.97 for glass beads of 300μm of diameter. Kharaz *et al.*[104] measured experimentally this coefficient and found a value of 0.97. In this work, in order to minimize numerical dissipations, a restitution coefficient value of 0.995 was used. Although this value may make the simulations more viscous than the experimental device [136], it was chosen because the numerical simulations of Samuelsberg & Hjertager suggested that a large restitution coefficient would lead to more accurate results. A wall restitution coeffi-

cient of 0.75, a friction factor of 0.2 and a maximum packing factor of 0.62 were used in the present calculations.

Based on the particle size and the density differences between particles and air, the solid phase is classified as a Geldart B powder group [211]. For this group, bubbling starts at the minimum fluidization velocity [212], i.e., $u_{mb} = u_{mf}$. A value of 19 cm.s^{-1}for the minimum fluidization velocity was obtained from the second form of the Thonglimp correlation [6],

$$u_{mf}Re_{mf} = \left[31.6^2 + 0.0425GaM\nu\right]^{0.5} - 31.6 \tag{8.1}$$

where $M\nu$, is density ratio defined as

$$M\nu = \frac{(\rho_s - \rho_g)}{\rho_g} \tag{8.2}$$

and Ga, Fr and Re_{mf} are the dimensionless Galileo number, Froude number and Reynolds number at minimum fluidization condition:

$$Ga = \frac{d_s^3\rho_g^2 g}{\mu_g^2} \quad Fr = \frac{u_{mf}^2}{gd_s} \quad \text{and} \quad Re_{mf} = \frac{\rho_g u_{mf} d_s}{\mu_g} \tag{8.3}$$

In the simulations presented here, both phases are considered incompressible. The two-fluid granular temperature equations are used with gas-phase pressure terms appearing in both gas and solid phases. The gas-solid friction and drag coefficients are calculated from a modified Ergun equation [11] for a solid volume fraction greater than 0.2, and by a swarm-corrected single particle drag law for volume fractions less than 0.2.

8.3 Numerical Results

The numerical simulation in 2D, axi-symmetric and cartesian geometries were performed. Quadrilateral elements provided a bi-linear variation of velocity and piece-wise-constant variations of volume fraction, pressure and granular temperature.

The computed time-averaged, solid flow, pattern in a fluidized bed in r-z geometry using a 13×20 finite element mesh is shown in Figure 8.2(a). On average, particles are seen to ascend at the center and descend near the wall. This behavior is consistent with the experimental results reported by Lin *et al.* [3] which are shown in Figure 8.2(b). The simulation agrees qualitatively with the experiment in this respect.

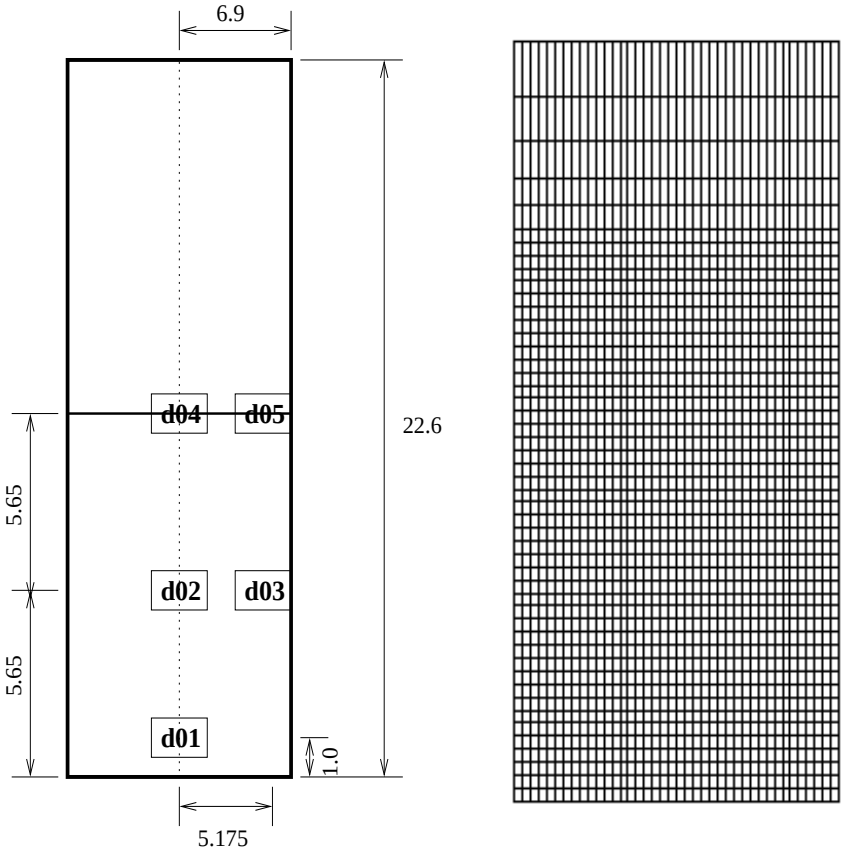

(a) (b)

Figure 8.1: Gas-Solid fluidized bed configuration : (a) schematic of the simulations conducted which is similar to the experiment carried by Lin *et al.*[3] and the detector positions used in the simulations performed here - all distances are in cm; (b) 40×44 mesh used to discretise the domain in 2D cartesian geometry.

The time-averaged height of the experimental bed is about 20 cm, which converges well with the simulated bed height as shown in Figure 8.3(a).

Discrepancies between the experiment and prediction results may be due to the experimental dynamics being three-dimensional, while two-dimensional axi-symmetric and cartesian coordinates were used for the simulations described in this work. In order to introduce heterogeneity into the bed, a small random perturbation was added to the initial particle volume fraction distribution. This enables the symmetry to break early into the simulations.

Differences in boundary conditions may give rise to additional discrepancies between experiments and numerical simulations. Furthermore, while an uniform inlet gas velocity was enforced in the simulations, it is very difficult to obtain this uniform velocity profile in experimental devices. Indeed, other workers [211, 195] have emphasized the importance of a uniform inlet velocity and its effect on the system's behavior. A non-uniform inlet velocity creates a pressure drop in the cross-stream wise direction and, therefore, the velocity profile and the volume fraction distribution will differ from those obtained with a uniform velocity.

There will also be differences between experiment and calculation in the initial loading of the fluidized bed. Twenty-five seconds of real time simulation were performed using the mesh shown in Figure 8.1(b), and the following fields within the domain were calculated : volume fraction, granular temperature, velocity vectors and gas pressure. Figure 8.3(a) shows the modelled time-average volume fraction of particles during 20 seconds (the first five seconds were neglected). This indicates that, in the time-average sense, particles have higher concentration near the wall than at the center of the bed. Modelled average granular temperatures of particles are shown in Figure 8.3(b) and indicate that the bed's granular temperature is higher near the top than in the other parts of the bed. The change in the direction of motion of particles near the top of the bed creates a particle shear stress, and this is the main source of granular temperature. In addition, the passage of bubbles mainly through the bed center generates a relatively large time averaged granular temperature near the bed center as depicted in Figure 8.3(b).

Dynamical simulation of the bed begins impulsively. As a result, a large bubble is

produced which moves upwards, releasing at the bed surface. After the eruption of this first large bubble, whose radius is comparable with the diameter of the fluidized bed, new bubbles form near the bottom of the bed and rise towards the free surface. In order to show the structure of the first large bubble, a sequence of images are depicted in Figure 8.4. It illustrates the rise of this bubble and the resulting expansion of the bed. After the bubble's eruption, the bed's height contracts. Velocity vectors associated with these images are shown in Figure 8.5. The flow of particles around the bubble is similar to that of true liquids past a two-dimensional bluff body, an analogy that was first used by Davies &and Taylor [213]. A pair of vortices behind the bubble can be seen in the velocity vectors plots, which also show that particles are falling near the wall. The figures also show the dilute particles inside the bubble are descending.

In order to illustrate the coalescence of bubbles within the bed, a sequence of images are shown in Figure 8.6. The raising bubbles take the form of a hemisphere, in which the lower and flat part, is called the wake of the bubble. As seen in these figures, a 'lower' bubble accelerates vertically and enters the wake of 'an upper' bubble, so that coalescence occurs from bellow.

8.4 Power Spectra Analysis

To illustrate how the solid volume fraction changes with time, void fraction fluctuations at different sample points (detectors), as shown in Figure 8.1(a), are plotted in Figure 8.7. The first large peaks in these figures correspond to the formation and eruption of the first large bubble, described previously. As can be seen from this figure, the void fluctuation amplitude is larger in the center (detectors 2 and 4) than at the corresponding heights near the wall (detectors 3 and 5). These figures also show a larger amplitude at the detector 5, indicating that the voids grow as they approach the surface of the bed. Detector 1, placed at 1 cm above the distributor, shows the smallest oscillation in amplitude due its location at the region near the bubble formation. Figure 8.7(f) shows the voidage fluctuation in the center of the bed at 0.25 cm above the distributor. The smaller amplitude seen in this figure is due to the proximity of the detector, just above the distributor.

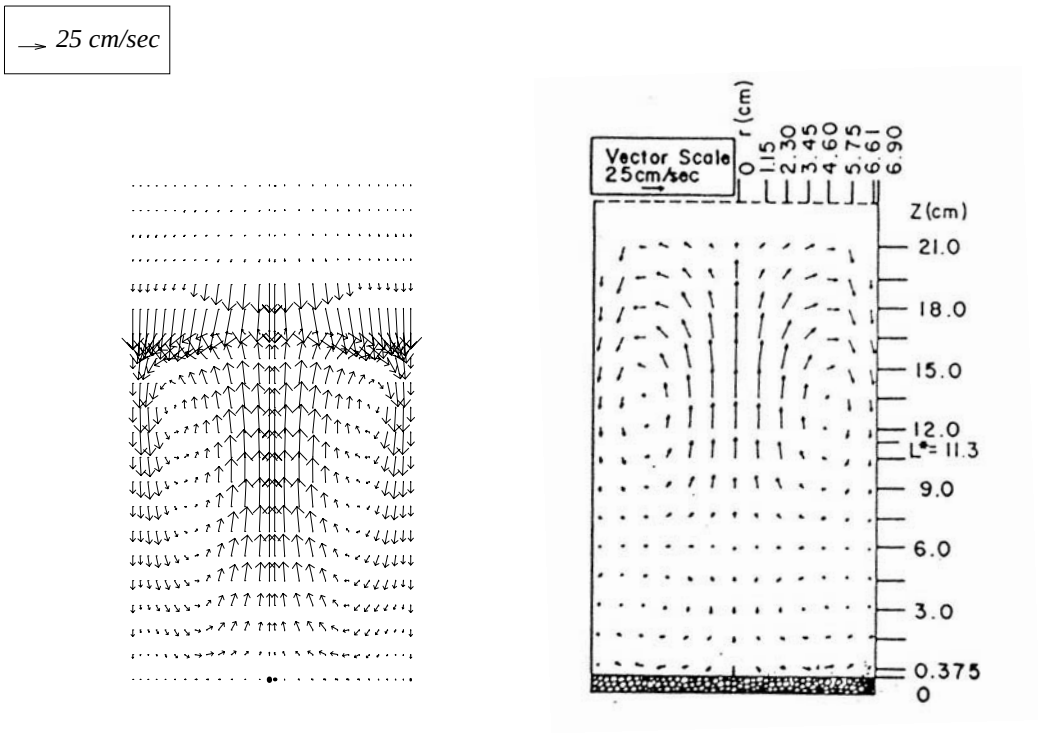

(a) (b)

Figure 8.2: Bubbling fluidized bed: (a) time-averaged velocity vectors of the particles, calculated in cylindrical coordinates; (b) velocity vectors obtained from the experiment.

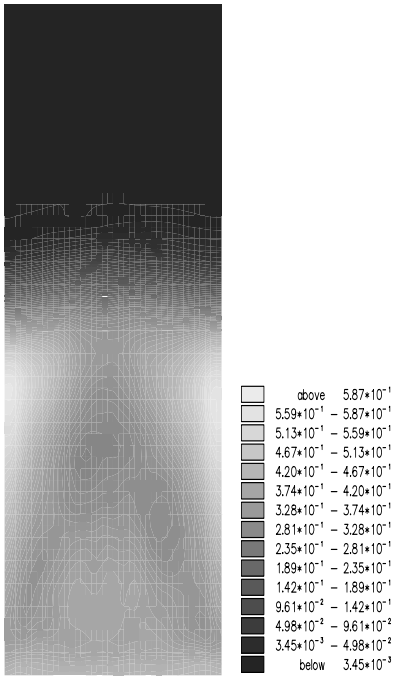

(a) solid volume fraction

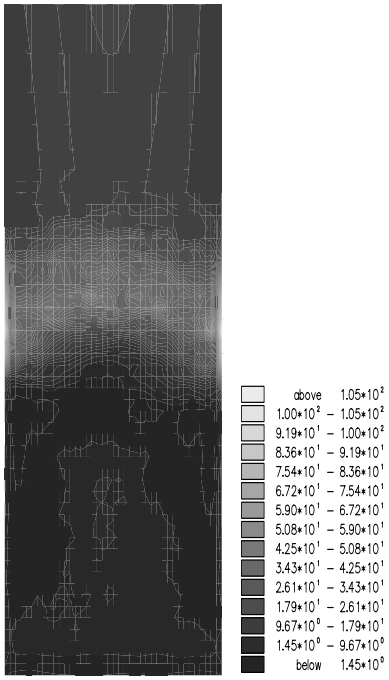

(b) granular temperature

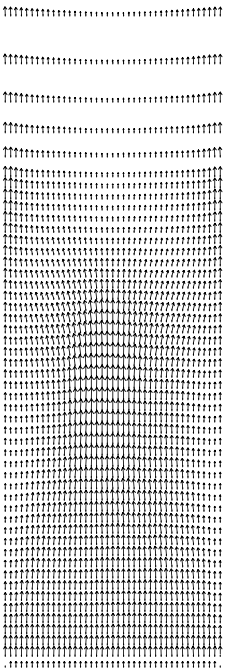

(c) gas velocity

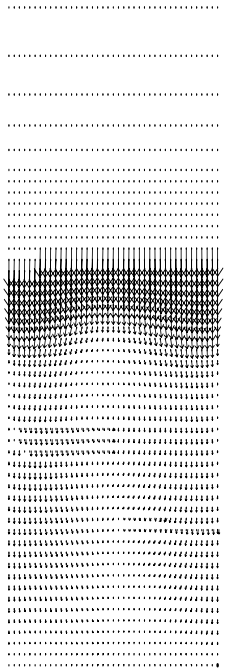

(d) solid velocity

Figure 8.3: Bubbling fluidized bed modelled in 2-D cartesian coordinates: (a) time-averaged volume fraction of particles. On average, particles have higher concentration near the walls than near the center. (b) time-averaged granular temperature (cm^2s^{-2}). The granular temperature near the top of the bed is higher than in other regions of the bed. Time-average gas and solid phase velocity vectors diagrams (c) and (d), respectively. The maximum velocity of the glass beads and air are 110.00 and 154.2 $cm.s^{-1}$, respectively.

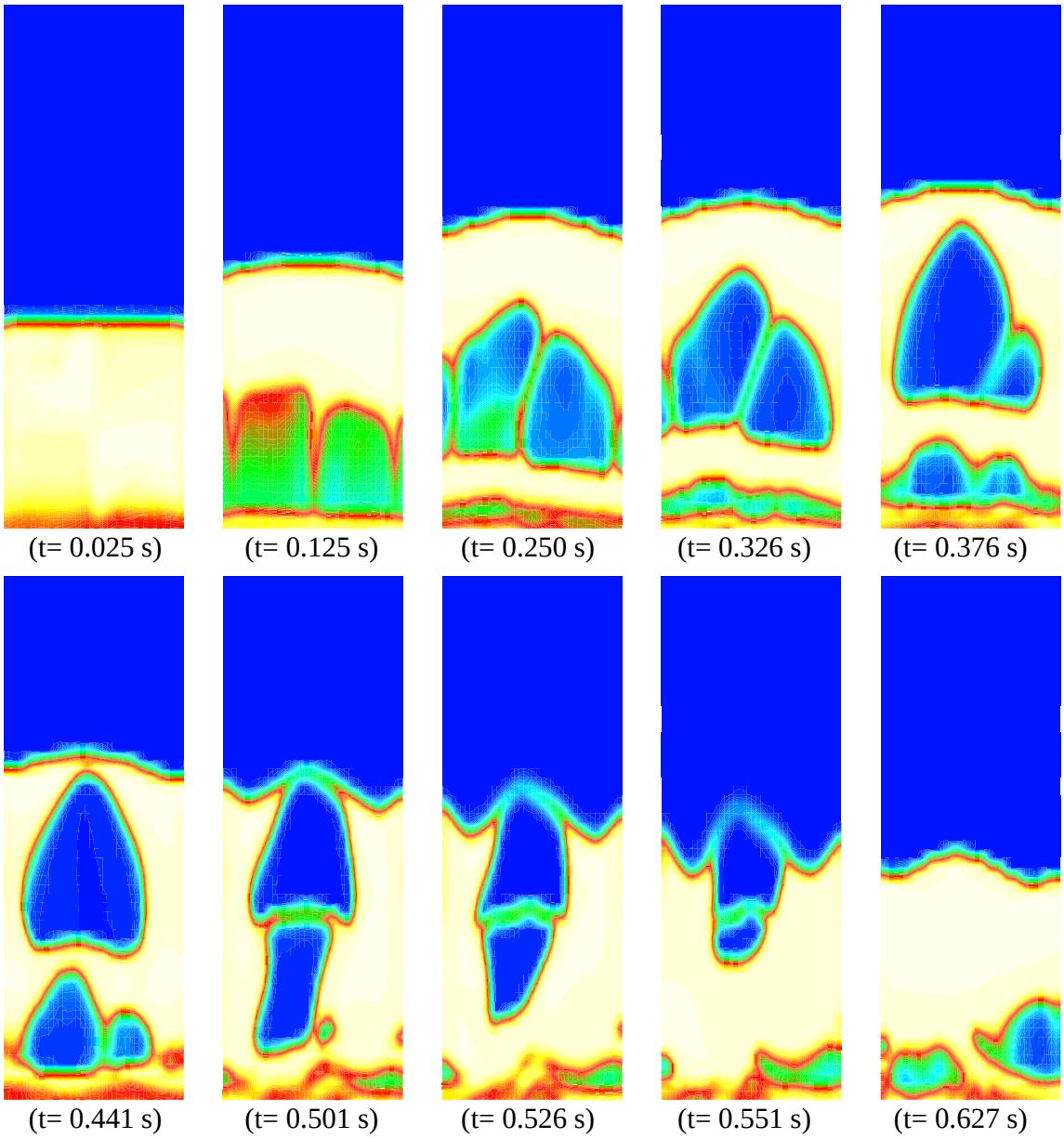

Figure 8.4: Distribution of the solid volume fraction for a simulated bubbling fluidized bed - the mesh used for this simulation was 40×44. At the beginning of the simulation a large bubble forms, rises and erupts at the surface of the bed. As a result, the bed height expands and then contracts.

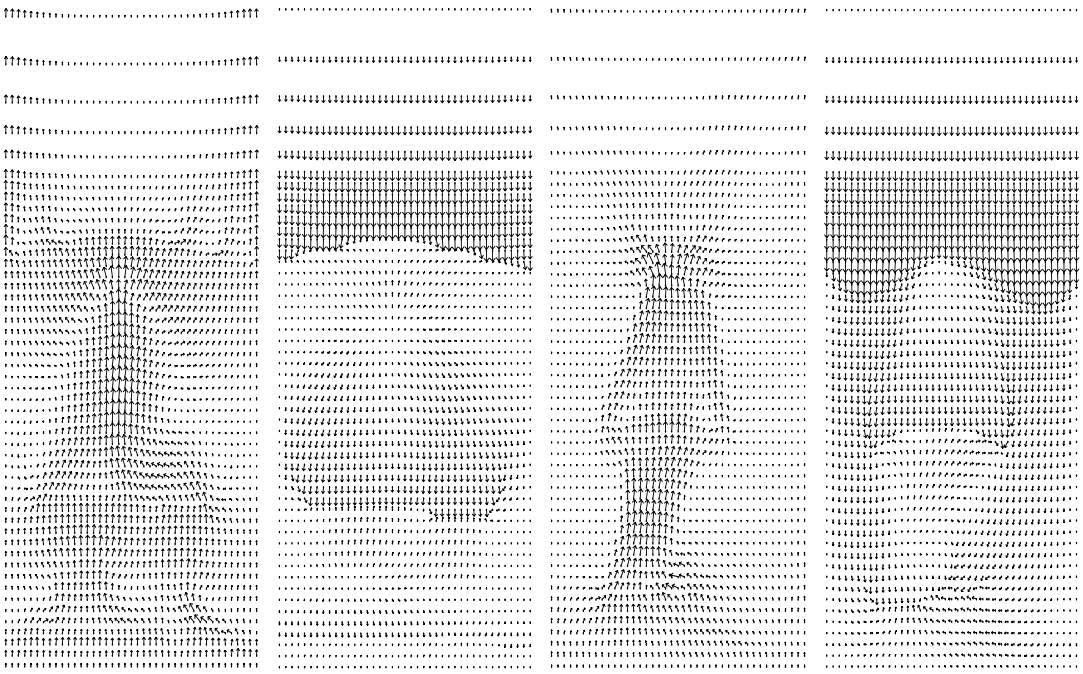

(a) (b) (c) (d)

Figure 8.5: Velocity vectors of glass beads(b,d) and air (a,c) at t=0.376 s and t=0.501 s, respectively. The maximum velocity of the glass beads are 127.0 and 124.84 cm.s^{-1} and for the gas flow are 285.0 and 505.0 cm.s^{-1}, at t=0.376 s and t=0.501 s, respectively.

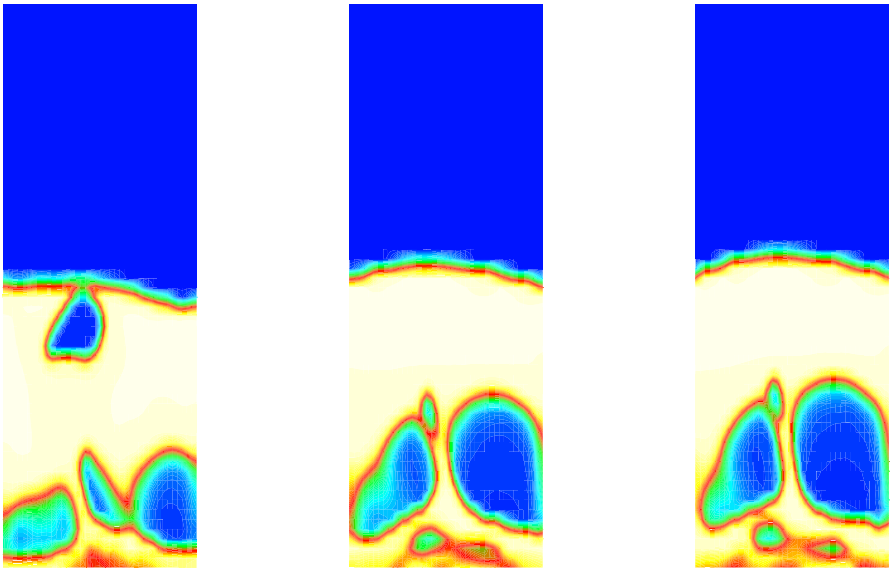

(t=21.29s) (t=21.39s) (t=21.41s)

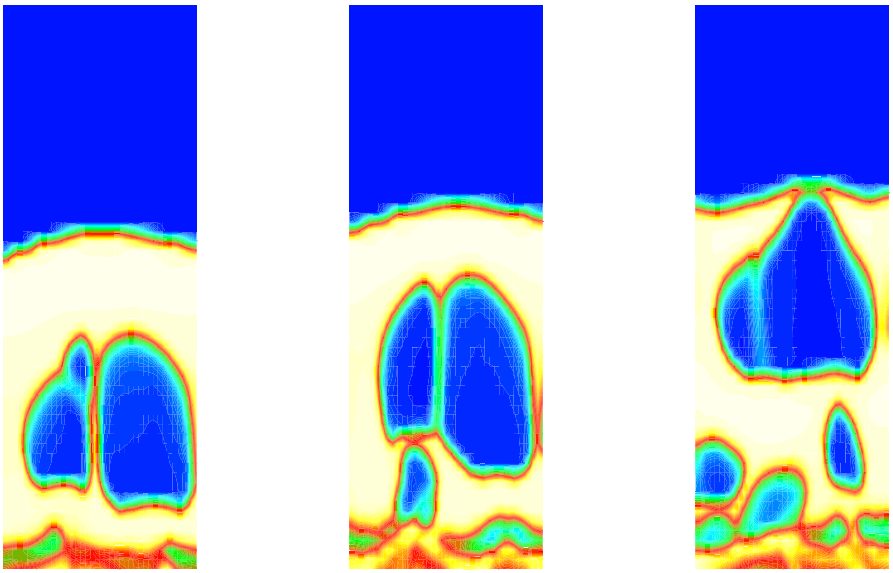

(t=21.49s) (t=21.59s) (t=21.79s)

Figure 8.6: Sequence of bubbles' coalescence phenomena in a simulated bubbling fluidized bed. The mesh used has 40×44 elements.

As reported in Section 8.3, the simulations described in this work were performed for 25 seconds with a time step size of 2.0×10^{-4}. The first five seconds of simulation were neglected, therefore all the effects due to the impulsively initialization were disregarded. The Fast Fourier Transform (FFT) method was used to calculate the power spectra of the gas volume fraction of this set of data points. The power spectra of the time-series shown above are depicted at Figure 8.8. The dominant frequencies obtained from these pictures reveals that they vary with the position in the bed, moreover, as can be seen, they assume values from 1.5-6.0 Hz within the bed. From Figure 8.8, two main conclusions can be drawn; firstly the detectors placed in the center of the bed have dominant voidage frequencies associated with them that are higher than the observed at the detectors near the wall and at the same height; secondly, the closer to the distributor the detector is placed the higher the dominant frequency. The sample points placed near the walls have dominant voidage frequencies associated with them smaller than those at the same height in the center of the bed. These smaller values are due to the train of rising bubbles in the center path of the bed which makes the frequency spectrum in the vicinities of the wall less susceptible to small changes in volume fraction. In fact, this could be observed either in the animations displayed at the ACMG homepage[2] or in the void fraction time-series of Figures 8.7. To investigate the dynamics in the wall's neighborhood, the power spectrum of the void volume fraction time series, at detectors 3 and 5 were analyzed (Figure 8.8). These figures show that the dominant frequencies in the regions near the walls (approximately 2 Hz) are smaller than the corresponding frequencies obtained from sample points located at the same height in the center of the bed. These smaller frequencies are related to the center-preferred movements of bubbles. Furthermore, the bubble waves seem to play an important role in the other less dominant frequency components. The effect of the walls on the flow dynamics is the focus of Section 8.7.

The influence of the time window size used to obtain the power spectra of the void fraction at detector 1 is shown in Figure 8.9. These spectra were obtained over the final 20, 15 and 10 seconds of simulation (the first 5 seconds were taken off in order to avoid discrepancies due to the impulsively initializing the simulation). It can be seen that the

[2] http://julia.ese.imperial.ac.uk

dominant frequency varies by less than 1% throughout the time ranges. In fact, the larger the time window the more the dominant frequency peaks shift slightly to the right. Figures 8.9(d)-(f) show the time-average solid volume fraction averaged over 20, 15 and 10 seconds, respectively.

8.5 The Effect of Grid Size

The grid size is considered an important parameter in problems involving numerical solutions. The mesh plays an important role in the numerical resolution and also determines the computational effort. Figure 8.10 shows the eruption of the first bubble using a course mesh of 13×20, for the same conditions used to generate the fine mesh results shown in Figure 8.4. It can be seen that in the course mesh results, the first bubble is represented by a large wave since the bubble boundary is smeared. Therefore, in order to investigate the effect of the grid resolution on the solutions, the simulation was repeated using the following grids: 13×20, 40×20 and 40×32, where the first and second numbers are the number of uniformly spaced elements in the x and y-directions, respectively. The power spectra of the void fraction, obtained from detector 1 over the final 20 seconds of simulations, were compared for different grid sizes. In this way, the influence of the grid size upon the numerical solution can be evaluated.

Initially, the power spectra of the 13×20 and the 40×20 grids were compared. As can be seen in Figure 8.11(a), when the number of elements in the x-direction was increased, the dominant frequency (around 5 Hz) was only slightly shifted to the right, indicating that the number of elements in this direction is probably adequate to solve the solution. The number of elements was then increased in the y-direction from 20 to 32, and the resulting spectra shown in Figure 8.11(b). As can be seen, the peak shifts to the right, which indicates that the mesh was not sufficiently fine in y-direction. The grid resolution was further increased again from 32 elements in the y-direction to 44 and the power spectra were compared. A shift to the right in the power spectra was observed in Figure 8.11(c) indicating that there may still be room for improvement of numerical resolution. However, further increases in resolution were not pursued because of the computational

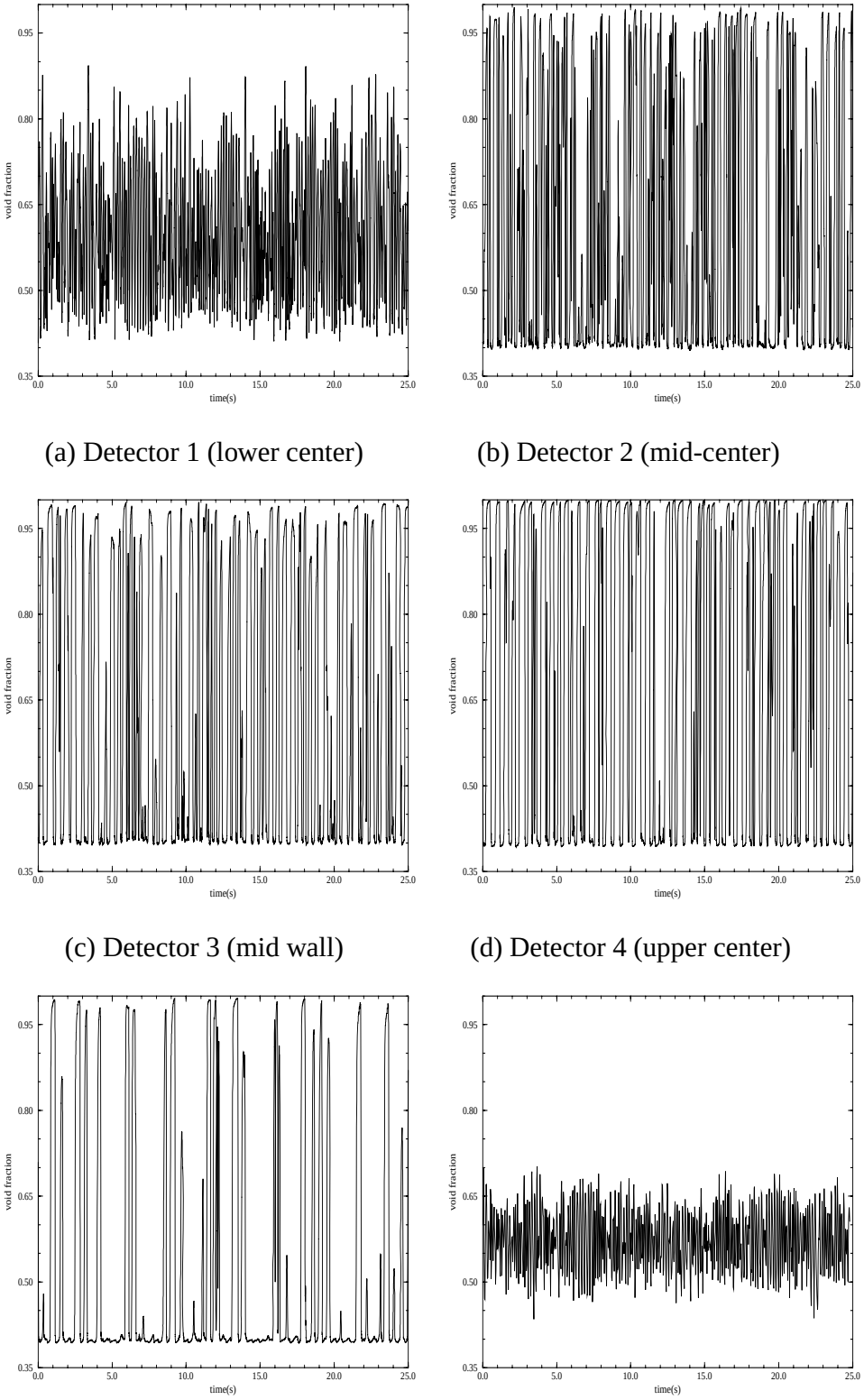

(a) Detector 1 (lower center)

(b) Detector 2 (mid-center)

(c) Detector 3 (mid wall)

(d) Detector 4 (upper center)

(e) Detector 5 (mid wall)

(f) Sensor just above distributor

Figure 8.7: Void fraction time-series during 25 seconds of simulation at 5 detectors placed at various points within the bed. Position related to (f) is placed in the center of the bed at 0.25 cm above the distributor

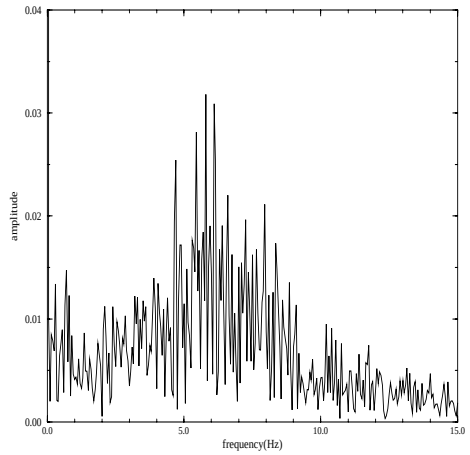

(a) Detector 1 (lower center)

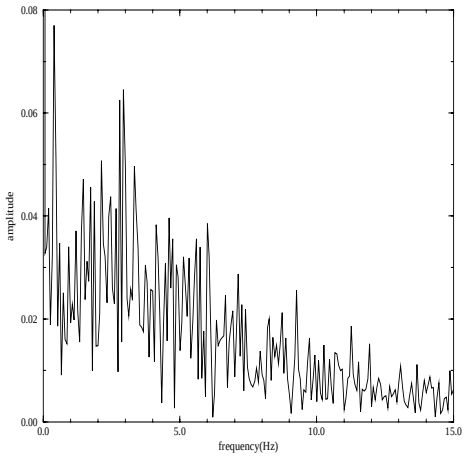

(b) Detector 2 (mid-center)

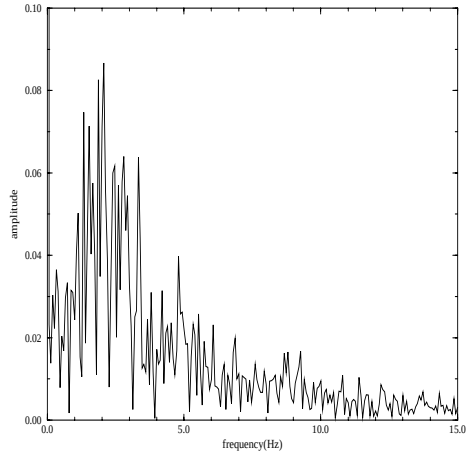

(c) Detector 3 (mid wall)

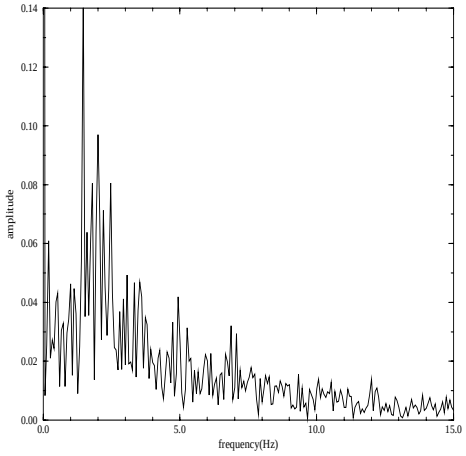

(d) Detector 4 (upper center)

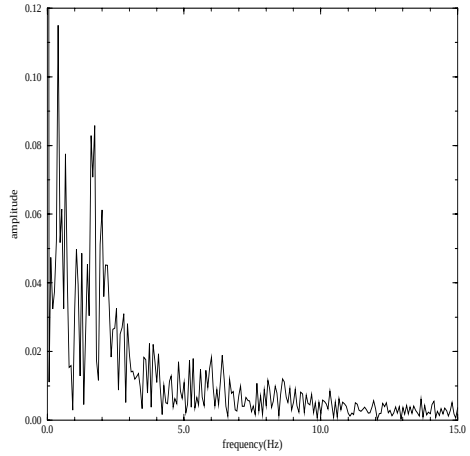

(e) Detector 5 (mid wall)

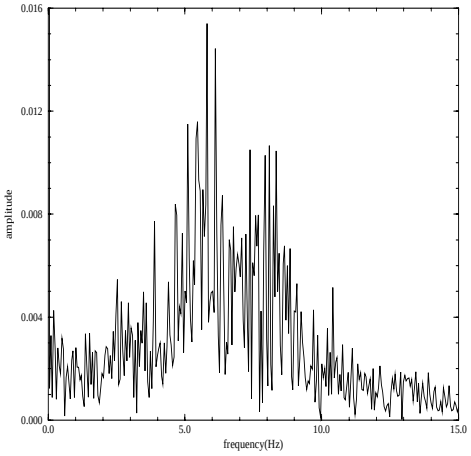

(f) Sensor just above distributor

Figure 8.8: Power spectra of void fraction fluctuations at different detectors.Position related to (f) is placed in the center of the bed at 0.25 cm above the distributor

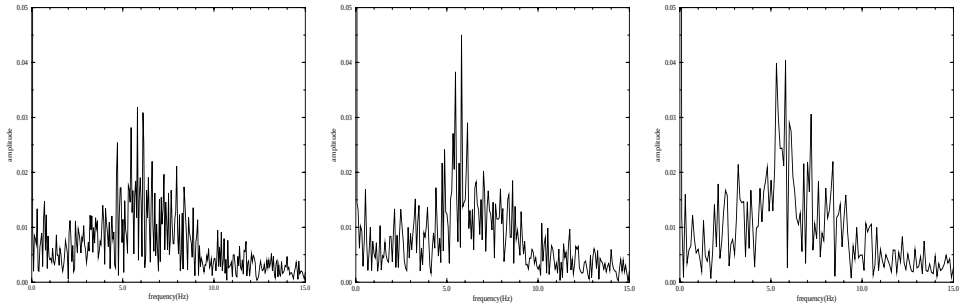

(a) Δt=20 s (b) Δt=15 s (c) Δt=10 s

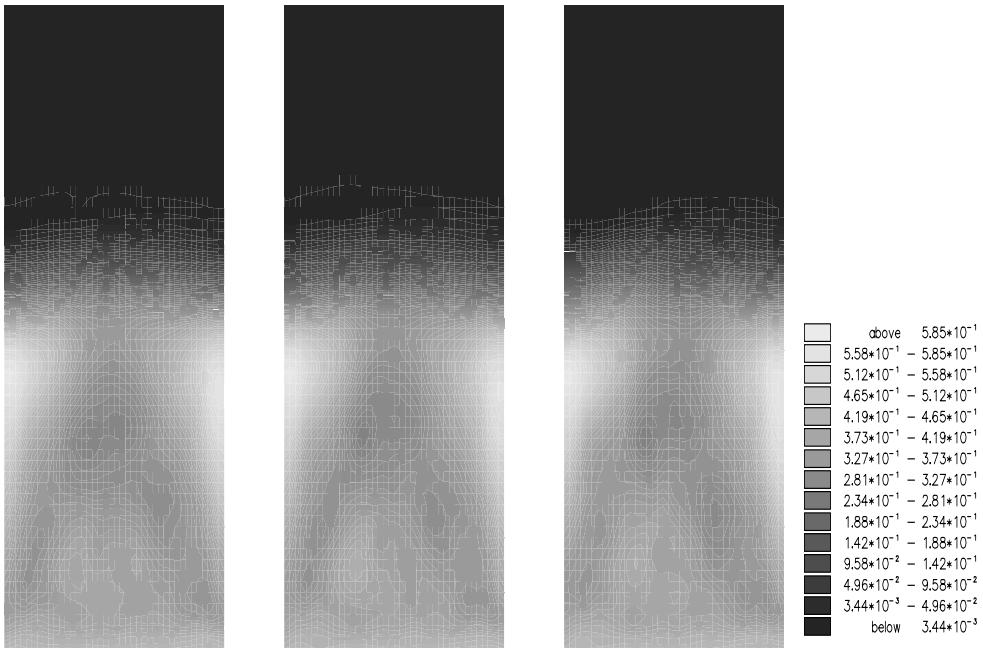

(d) Δt=20 s (e) Δt=15 s (f) Δt=10 s

Figure 8.9: Power spectra of void fraction fluctuation at detector 1 and corresponding time-average solid volume fractions. The time interval used to generate the frequency spectra and the averaged volume fractions are indicated under the figures.

demands. This lack of numerical convergence led us to use all four numerical solutions in the analysis of the next section.

8.6 Investigation of Hydrodynamics of the Fluidized Bed using Chaos Theory

In this section, some statistical parameters, such as the maximum likelihood estimation of the correlation dimension (D_{ML}) and the Kolmogorov entropy (K_{ML}), the Lyapunov exponent and the non-linearity test are used to help analyze the chaotic behavior of the simulated fluidized beds. A review of these dynamical parameters was reported by Johnsson *et al.* [113].

The correlation dimension of an attractor identifies the spatial correlations between points on the attractor, i.e., it is related to the spatial complexity of the attractor in state-space. In fact, it can be defined as a measure of the spatial homogeneity in the state space. Moreover, the correlation dimension is obtained from the correlation integral which is described as the probability that two points on the attractor are within a cell of size *l*. The correlation integral is usually obtained from the Grassberger-Procaccia method which calculates the density of the attractor in phase space from:

$$C(l) = \frac{1}{N(N-1)} \sum_{i,j=1, i \neq j}^{N} \Theta\left(l - |\underline{x}_i - \underline{x}_j|\right) \tag{8.4}$$

where x_i and x_j are the embedded points in the vector time series, N is the number of points, Θ is the Heaviside step function defined as

$$\Theta(\mu) = \begin{cases} 1 & for \quad \mu \geq 0 \\ 0 & for \quad \mu < 0. \end{cases} \tag{8.5}$$

Van der Stappen *et al.* [149] reported that for small length scales, the correlation integral and the correlation dimension (D_l) are related as

$$C(l) \approx l^{D_l}. \tag{8.6}$$

D_l can be calculated from either the slope of the linear part in the log-log plot of the

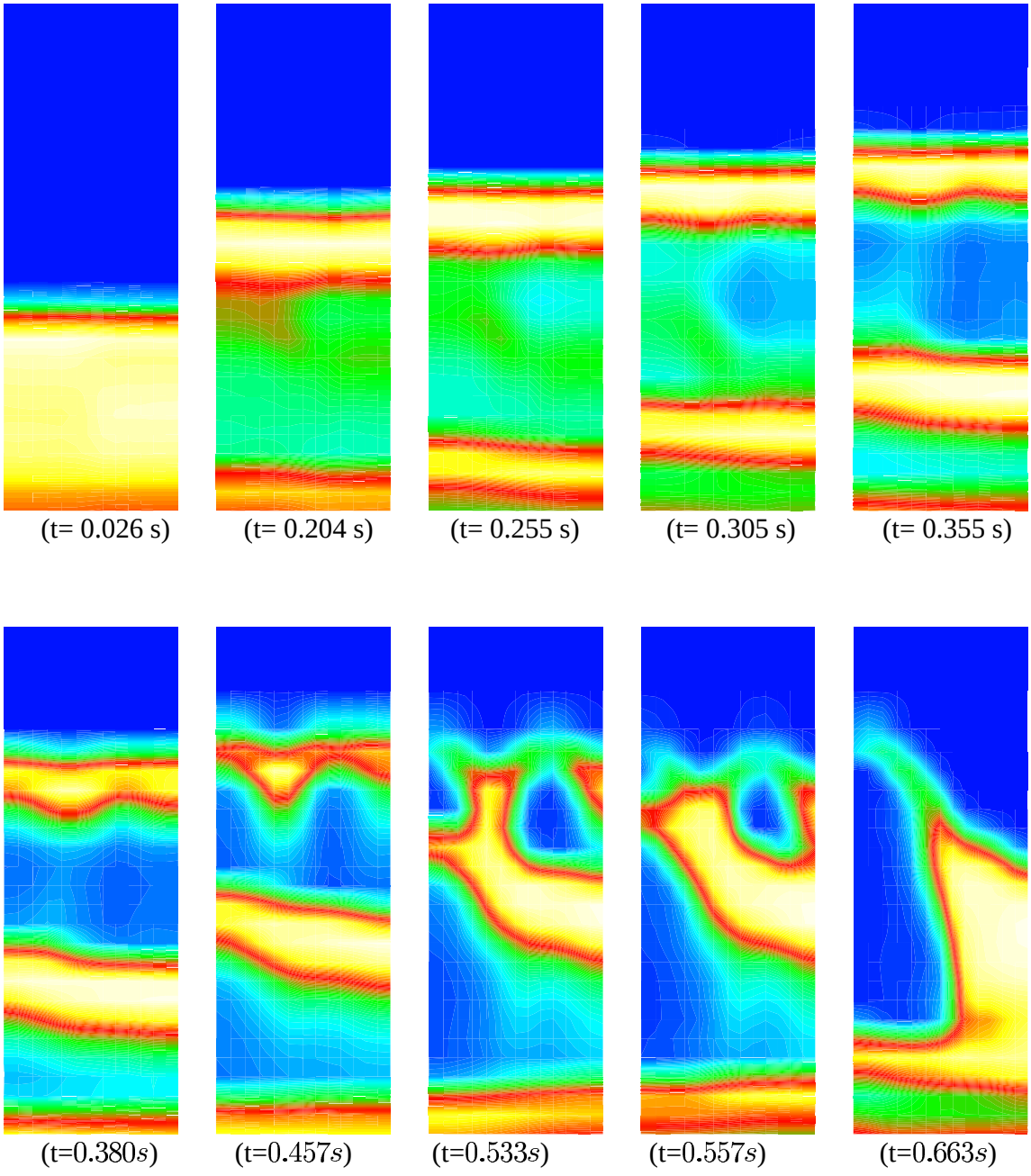

Figure 8.10: Distribution of volume fraction of particles for a bubbling fluidized bed simulated using a 13×20 grid. The first bubble, also reported at Figure 8.4, rises as a large wave due to low numerical resolution.

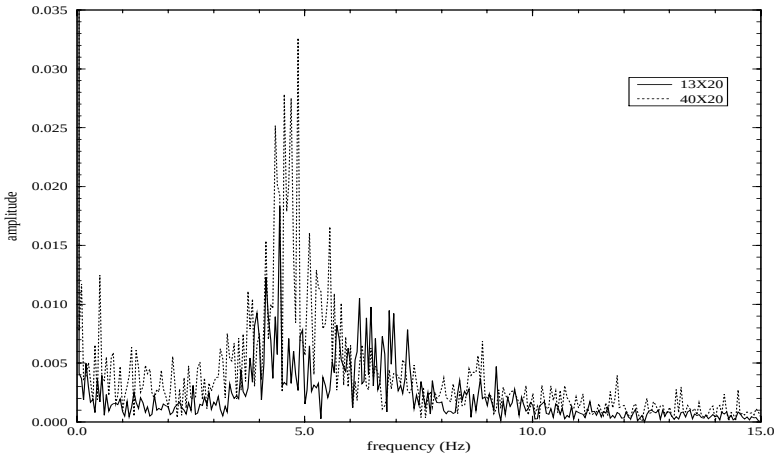

(a) Power spectra of the 13×20 and 40×20 grids.

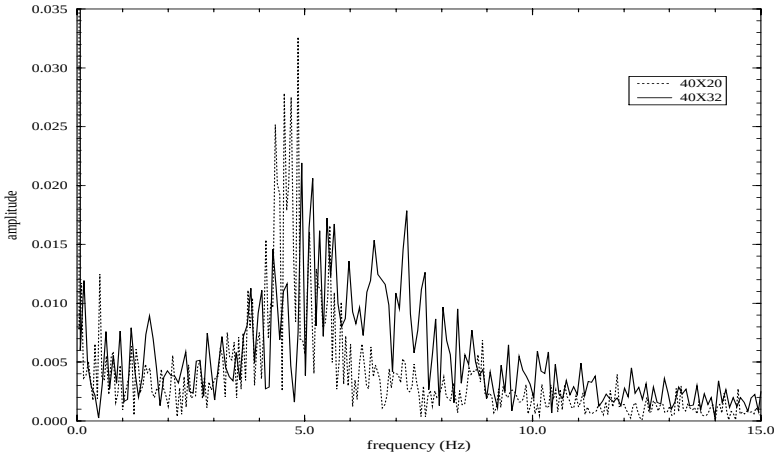

(b) Power spectra of the 40×20 and 40×32 grids.

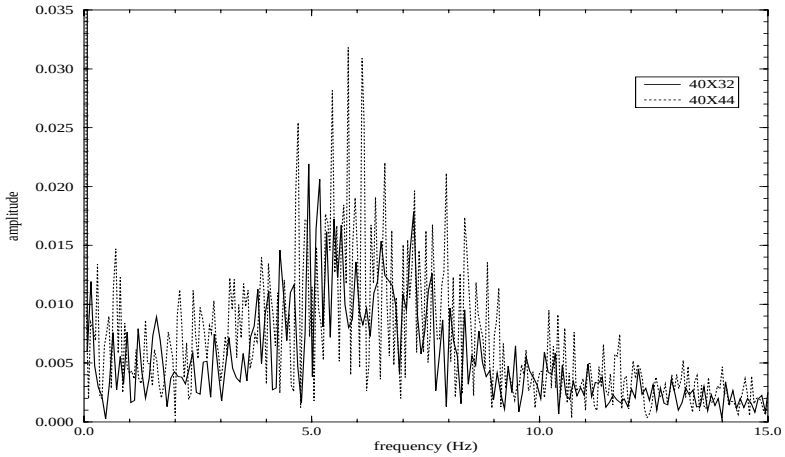

(c) Power spectra of the 40×32 and 40×44 grids.

Figure 8.11: Power spectra of bubbling fluidized bed for several grid sizes at detector 1.

correlation integral versus distance, *l*, or by fitting $C(l)$ to l at small length scales using any non-linear surface fitting method.

In order to show the low-order attractor dimension, the logarithm of the correlation integral, $logC(l)$, was plotted against the logarithm of the relative distance, $log\frac{l}{l_0}$ (see Section 5.6.3 and [47, 143]), for several embedding dimensions obtained from the voidage fluctuation time-series of the 40×44 grid simulation. As can be seen in Figure 8.12(a), as the embedding dimension is increased a relatively constant slope of about 1.8 is obtained, which indicates a low-order attractor dimension equal to 2.

According to Takens [214], if the underlying state space of a system is d dimensional, then $2d+1$ embedding space dimensions are sufficient to capture completely the dynamics of the system. However, as Hilborn [49] reported, for dissipative systems the effective dimensionality is that of the system attractor, in this case $\sim$1.8. Therefore an embedding dimension greater than or equal to 5 is adequate to capture the dynamics of the system. According to Huilin *et al.* [43], having a dimension less than 2, it proves that the hydrodynamics of this fluidized bed is governed by two independent variables, which could be chosen to be the void fraction and the slip velocity. As Huilin *et al.* explained, there is also an upper limit to the number of variables required to describe the dynamics of the system, $2d+1$, in this case 5 variables, which consists of two components of the velocity in each phase and a void fraction. This implies that, at most, 5 differential equations are necessary to describe the system. They emphasized the importance of the drift flux model, in which only two variables, namely void fraction and slip velocity, need to be considered for small circulating fluidized beds. For larger diameter fluidized beds, where cross flow phenomena are important, the flow should be expressed as a function of the void fraction and the three components of the slip velocity.

These arguments demonstrate the potential of chaos theory to determine the number of variables that a modeler should use to develop useful design correlations.

The concept of the Lyapunov exponents was developed to characterize the stability of linear and non-linear systems. They are defined as the logarithms of the absolute value of the eigenvalues of the linearized dynamics averaged over the attractor [47]. A negative exponent suggests a local average rate of contraction whereas a positive value indicates

a local average rate of expansion. Many researchers have been using the spectrum of Lyapunov exponents as a measure of the effect of perturbing the initial conditions of a dynamic system.

The Kolmogorov entropy is defined as the sum of the positive Lyapunov exponents of chaotic systems [49], therefore a positive Kolmogorov entropy indicates that at least one of the Lyapunov exponents is positive, showing that the system is chaotic. For periodic data, i.e., completely predictable, the entropy is equal to zero. On the other hand, the entropy of purely random data is infinite, and systems with deterministic chaotic dynamics have entropies between the limits of the random and periodic. The Kolmogorov entropy is formally defined as a measure of the rate of information loss along the attractor or as a measure of the degree of predictability of points along the attractor given an arbitrary initial point [150]. Therefore, the Kolmogorov entropy is the best way to estimate the rate of generation of information of a system and can be used to characterize the time dependent behavior of fluidized beds.

Although chaotic systems usually have infinite fractal correlation dimension, a non-integer value can not be considered as a definite proof of the characteristic dynamics of a system. In fact, the integer number greater than the correlation dimension is usually related to either the dimension of the true state space or the number of degrees of freedom of the signal.

In this work, the maximum-likelihood estimation of the correlation dimension (D_{ML}) and the Kolmogorov entropy (K_{ML}), as presented by Schouten et al.[150, 149], were processed by means of the RCHAOS software package [147]. The D_{ML} is mathematically defined as :

$$D_{ML} = \left[\frac{1}{M} \sum_{i=1}^{M} -\ln \left(\frac{l_i}{l_0} \right) \right]^{-1} \tag{8.7}$$

where M is the sample size of interpoint normalized distances $r_i = l_i/l_0$. The distances l_i are normalized by the maximum scaling distance, l_0. The maximum-likelihood estimation of the Kolmogorov entropy is described as :

$$K_{ML} = -f_s \ln \left(1 - \frac{1}{\bar{b}} \right) \tag{8.8}$$

with

$$\overline{b} = \frac{1}{M}\sum_{i=1}^{M} b_i. \tag{8.9}$$

b_i is the number of sequential pairs of points on the attractor in which the interpoint distance is greater than the specified maximum interpoint distance, l_0. Thus, $\overline{b}$ is the average value of the set of b_i, $\forall i = \{1, 2, ..., M\}$ in the sample with sample size M. f_s is the sampling frequency. The K_{ML} is measured either as $bits/s$ or as $bits/cycle$, which are related to the loss of information in real time units and within an average cycle in the time series, respectively.

The surrogate analysis [113] is a tool for evaluating the non-linearity of a set of data points. Firstly, the phases of the Fourier transform of the original time series are randomly shuffled and then the inverse transform is applied to generate a surrogate time series that has the same autocorrelation as the original time series. If the original time series is non-linear, then after this procedure the surrogate data series dynamical parameters should be different from the former's data set. If there is not any difference in such parameters then the former time series can not be considered as non-linear or chaotic. The average difference between the original time series and the surrogate time series is described by the average number of standard deviations of the surrogate series, Z_{avg}.

In the algorithm reported by Johnsson *et al.* [113] the Z_{avg} value should be less than -3, and the low the value of Z_{avg}, the lower the probability that the original time series was generated by a linear stochastic process. However, Z_{avg} greater than -3 does not necessarily mean that the time series is not chaotic, but the dynamic parameters obtained by the surrogate time series can not be unequivocally related to chaotic systems.

Johnsson *et al.* used the aforementioned parameters to describe the chaotic behavior of fluidized beds using a time series achieved from pressure fluctuations. Moreover, they suggested that the dynamical parameters should be used to characterize the flow regime during a numerical simulation. They reported some ranges for the maximum-likelihood estimation of the correlation dimension and the Kolmogorov entropy and the average surrogate time-series value. According to them, for low velocity slugging regimes the D_{ML} should be around 2.0, whereas for high velocity turbulent regime, its value should

be up to 6.0. For bubbling regimes the maximum-likelihood estimation of the correlation dimension should be around 5.0. Therefore, as a measure of the complexity of the attractor in state-space, the D_{ML}, can be use to characterize the complexity of the regime and the evolving bubbles. Indeed, the D_{ML} and the Z_{avg} should be used to analyze the non-linearity since it is expected that systems with high dimension are difficult to set apart from stochastic systems. The calculated D_{ML} and Z_{avg} of the fluidized bed described in previous sections are shown in Tables 8.1 and 8.2, respectively.

Although the Z_{avg} are, in most cases, greater than -3, the time series can not be claimed, definitely, as non-linear. Indeed, the maximum-likelihood estimation of the correlation dimension in all sample points of all grids reveal that the flow can be considered as bubbling. This flow behavior is confirmed by the void fraction distribution during the time series. Johnsson *et al.* reported that a time-series can be assumed as definitively non-linear if Z_{avg} and D_{ML} are less than -3 and 6.5, respectively. Figure 8.12(b) shows, for all 5 detector positions (and this includes the information shown in Tables 8.1 and 8.2) that most of the points lie within this range.

The maximum-likelihood estimation of the Kolmogorov entropy is more directly related to the macrostructure of the flow than the other dynamical parameters. Thus it can be used to characterize the flow regime, its value, in $bits/cycle$, for the aforementioned grids and sample points is depicted in Figure 8.13. This figure shows that the macroflow becomes more complex as the grid is refined. Moreover, the K_{ML} is sensitive to the position of the detector, i.e., the higher the sample point is located, the higher the value of K_{ML}. This may be directly related to bubble coalescence phenomena as reported by Nguyen *et al.* [215], indeed, at the lower positions the train of rising bubbles in the center of the bed trends to merge into large bubbles. These can only be observed at the detector located in the top of the bed height.

8.7 Investigation of Wall Effects

As described at Section 8.3, the bed walls play an important role in the bubbling regime. In this section some of the dynamical parameters previously reported are used to

Grid	Det. 1	Det. 2	Det. 4
13×20	5.23	5.40	4.95
20×20	5.90	5.62	3.00
40×20	5.54	4.98	3.81
40×44	4.71	3.94	2.19

Table 8.1: Predicted maximum-likelihood estimation of the correlation dimension (D_{ML}) at the detectors placed in the center of the fluidized bed (Figure 8.1 (a)) for the simulations conducted with the 13×20, 20×20, 40×20 and 40×44 grids.

Grid	Det. 1	Det. 2	Det. 4
13×20	1.04	1.74	0.10
20×20	-1.89	-1.64	-2.91
40×20	-2.94	-1.80	-3.40
40×44	-3.04	-4.27	-6.59

Table 8.2: Predicted average number of standard deviations of the surrogate series (Z_{avg}) at the detectors placed in the center of the fluidized bed (Figure 8.1 (a)) for the simulations conducted with the 13×20, 20×20, 40×20 and 40×44 grids.

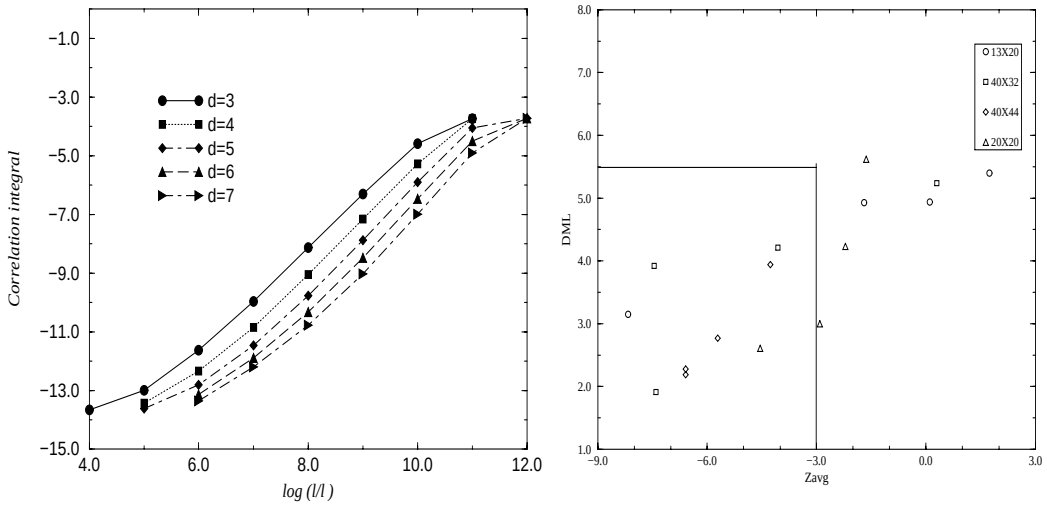

(a) (b)

Figure 8.12: (a) Log-log plot of the correlation integral versus relative distance (in the Euclidian sense) between volume fractions for the 40×44 grid bubbling fluidized bed at detector 2. (b) $Z_{avg} - D_{ML}$ plot for different grids at several positions.

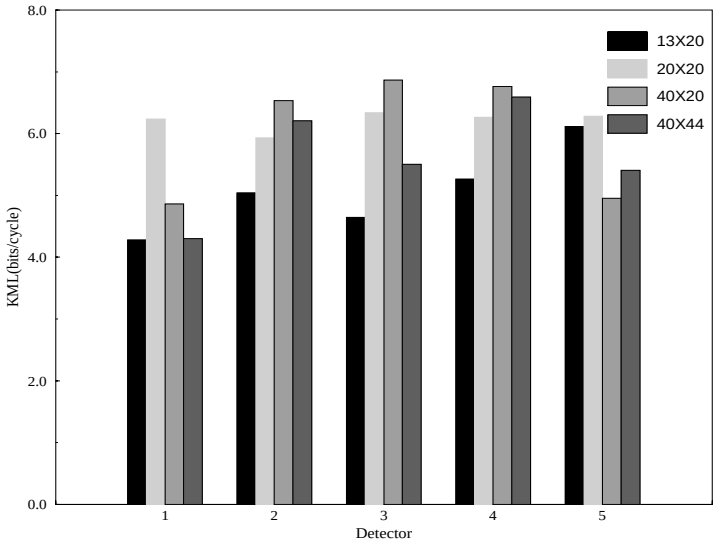

Figure 8.13: Maximum-likelihood estimation of the Kolmogorov entropy, in $bits/cycle$, at all detectors for the 13×20, 20×20, 40×20 and 40×44. Note that K_{ML} increases with height of detector.

analyze the flow behavior at the wall vicinities.

In order to study the influence of the walls on the behavior of the flow, a simulation was performed in a 2-D fluidized bed consisting of a column of width of 24 cm in which spherical glass beads of 500μm of diameter and a density of 2.5g.cm^{-3} are fluidized. The static bed height is 12 cm. The width of the column was increased relative to the height of the bed in order to assess the effect of the walls in the bed dynamics. All the boundary and initial conditions described for the bed at Section 8.2 were used in this simulation. However, an inlet gas (air) velocity of 100 cm.s^{-1} at room temperature (approximately five times the minimum fluidization velocity) was used in this numerical experiment. A time step of 2.0×10^{-4} seconds was adopted.

The minimum fluidization velocity for this system, which is classified as Group B of Geldart powders, is about 19.5 cm/s. As the Froude number is greater than unity, this bed, like most gas-particle fluidized beds, operates in an aggregative state in which bubbles play a major part in the dynamical behavior.

In the time-average sense, the concentration of particles near the wall is higher than that in the other regions of the bed (see [11]) and the time-averaged velocity vectors of the solid and the gas phase indicate that the gas velocity in the regions with lower concentration of particles is larger. In addition, a larger solid velocity is detected in the regions near the walls. Moreover, in a time-average sense, particles circulate by descending near the wall and ascending in the other regions of the column. A different behavior can be observed in a small region near the top and center of the bed. Although the symmetry is broken at the beginning of the simulation and the subsequent flow has no line of symmetry, in the time-average sense the flow has a symmetrical shape. The time-averaged granular temperature distribution indicates that, due to higher shear stress of particles near the top of the bed, the granular temperature of particles is higher at the top than in other regions of the bed.

The bubbles' coalescence effect was previously reported by Pain *et al.* [11]. In this case, the simulation was conducted in a relatively wide fluidized bed so as that the effect of the walls on the shape of the bubbles is negligible. The bubbles take the form of a hemisphere, in which the lower part of this hemisphere, the flat part, is called the wake

of the bubble. As a lower bubble accelerates vertically and enters the wake of the upper bubble, coalescence occurs. The gas phase moves with a high velocity through regions with lower concentration of particles; most gas flows through bubbles.

In the corners of the fluidized bed, particles descend near the walls and rapidly change direction as they approach the bottom of the bed. This effect was earlier reported by Wirth [12], who showed that the falling particles near the wall are decelerated by the upstream gas flow. This kind of 'flow colision' results in a circular/elliptical movement of either the gas or the particles stream directions. Indeed, the vorticity effects, observed at these figures, near the bottom corner of the fluidized bed is strongly related to the rising bubbles, i.e., while the bubbles are ascending, they catch some particles in their bottom hemisphere, the particles trends to occupy the voidage left by the bubble arising. This movement forces the particles flow downward to modify their direction and later to other directions due to other rising bubbles. In fact, the large particle vorticity in the bottom corners acts as a source of voidage, as reported by Gidaspow [38], from which bubbles are born.

8.8 Conclusions

Using the two-fluid-granular temperature model, fluidized beds have been simulated numerically. The gas, air at room temperature, enters from the bottom of the fluidized beds and exits from the top, while particles circulate inside the bed. In the fluidized bed simulated, which was operating in a bubbling regime with particles in group B of Geldart classifications, the time-averaged velocity vectors, obtained from the simulations, were qualitatively consistent with the corresponding velocity vectors seen in published experimental results. In addition, the simulated time-average bed height matches the experiment.

Grid convergence tests carried out as part of this simulation showed that, by increasing the number of elements, higher frequencies appear in the power spectra. In general, because of the chaotic behavior of the system, a refined grid is necessary to achieve a reasonable convergence.

To show that this system is chaotic, the correlation dimension, the Kolmogorov entropy and the Lyapunov exponents were calculated and it was shown that this system is chaotic with a low-order dimension, $\sim$1.8. As a conclusion, according to [43], at most 5 equations are necessary to describe the system, e.g, four equations for two components of velocity, in 2-D, for two phases, and one equation for the void fraction.

In order to investigate the effect of walls on the behavior of flow, the bubbles dynamics in the vicinities of the wall were analyzed. It was observed that the corners of the bed are among the locations where bubble formation starts. This can be attributed to the forces acting on the particles that are changing direction near the corners and creating regions of high vorticity, from which bubbles are born.

Chapter 9

Mixing Dynamics of Particle Clusters in Risers

9.1 Introduction

Fluidization technology is a trillion dollars business used in a wide range of chemical, biochemical, nuclear and energy generation processes [4]. In particular, gas-solid fluidized beds play an important role in a wide-range of industrial applications due to their high operational efficiency in chemical conversion, heat and mass transfers and particle mixing [4, 61]. Fluid catalytic cracking (FCC) technology is one of the most powerful fluidization technologies worldwide and is applied to the conversion of oil into low molecular-weight molecules such as gasoline.

Kersten *et al.* [216] (see also [217]) showed that bubbling fluidized beds can also be used to obtain energy from the pyrolysis of biomass as a cleaner energy resource. Kaneko *et al.* [20] investigated the polymerization of gas-phase olefins using 1000 μm diameter Ziegler-Natta catalyst particles. They simulated the conversion through the soft-sphere discrete element model (DEM), in which approximately 28000 particles were individually tracked in space-time in a 2-D domain. The use of DEM in the simulation of coupled particle-fluid flow has attracted great attention due to exponential increases in computational resources. However the maximum number of particles in such simulations is still

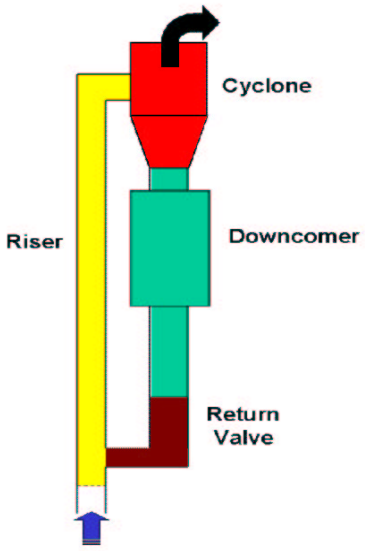

Figure 9.1: Schematics of a circulating fluidized bed.

limited by computational power. The two-fluid model (TFM) was used by Chaouki *et al.* [218] to study the catalytic oxidation of natural gas for the synthesis of ethylene in turbulent fluidized bed reactors. In their model, natural gas and air are fed into a reactor containing fine particles of catalyst (MgO with mean diameter of approximately 120 μm) and the flow can be categorized into three regions: (i) a single phase homogeneous bed, (ii) a two-zone bed with a dilute flow in the core and an emulsion zone in the annulus and (iii) a turbulent bed oscillating between slugging and homogeneous expansion. Such complex structures have the advantage of allowing fast gas-solid exchanges and additional conversion of reactant in the freeboard [4]. Circulating fluidized beds (CFB) are loop-systems commonly used in several industrial processes (Chapter 1). They are composed by a vessel, called riser, in which the entrained solids rise upward. At the riser exit, particles are captured and separated from the gas in a cyclone. The solids then pass via a standpipe back to the base of the riser for re-injection (Figure 9.1). Circulating fluidized beds are always operated in the regimes beyond bubbling fluidization, although they are often associated with operation in the fast fluidization regime.

The optimization of CFBs operations, in particular their chemical conversions and geometric configurations, have already been exhaustively investigated by a number of re-

searchers (see [16, 219, 220]. For instance: Levenspiel [53] reported the chemical kinetics in gas-solid reactor model, from packed beds to fast CFBs; Harris [221] investigated the influence of the exit geometry of CFBs on pressure fluctuations; Kehlenbeck *et al.* [16] experimentally studied the behavior of a CFB used in the pilot plant for the gasification of biomass, and proposed some expressions to correlate particle properties and the CFB performance.

Similarly, the modelling of the gas phase hydrodynamics and the dispersion of particles in CFBs has received a great deal of attention from the scientific community [222, 223, 224]. However, such investigations have made no particular distinction of the hydrodynamics in different parts, such as the downcomer, the riser, the cyclone, the measuring bed and the slow bed among others. While such work can lead to the operational optimization of emulsion and dilute flows in fluidization equipment, it does not contribute to the understanding of cluster motions, gas phase turbulence and other transport phenomena that should be studied individually.

The fluid dynamics investigations in CFBs have been focused on the cluster motion in the riser section, as it is here that the processes important to most industrial applications, such as solid segregation and mixing (due to radial gas mixing), and heat and mass transfer, take place. Glicksman *et al.* [223, 222, 225] investigated the radial solid flux in CFBs using a Lagrangian model and verified substantial interactions between the gas flows and cluster of particles bouncing through several cross-sections. Such interactions were mainly due to the gas phase turbulence and have strong influences on the wall-bed heat flux. Fligner *et al.* [226] developed a model which correlates the behavior of the radial density profile and the radial concentration in riser reactors operating under industrial conditions. Risers usually consist of two hydrodynamical regions: (i) an emulsion phase transported upwards by a dilute gas flow in the core zone and (ii) downwards particle flows in the annulus zone. However, Malcus *et al.* [227] experimentally investigated the radial solid flux in dense regions of CFBs, and noticed that at the bottom region of risers, particles may flow upwards near the wall. Such particle flow reorientation was also reported by Pain *et al.* [11] and by van der Stappen *et al.* [44] for fluidized beds operating under bubbling conditions, but with downwards particles forced to move up-

wards in the bottom region in the wall zone. Nieuwland *et al.* [228] used a 1-D model to study the steady-state hydrodynamics of fully developed flow in an axi-symmetric riser. Although their model did not take into account particle collisions model, the calculated axial velocity profile of the solid phase agreed with experimental data.

Numerical simulations involving cluster formation and motion in risers have received a great deal of attention due to the increase in available computer power [38, 229]. Tanaka *et al.* [224] used an Eulerian-Lagrangian model to investigate cluster structures and motion in a 3-D lab-scale riser and compared the radial concentration and velocity with those obtained experimentally. Although they agreed qualitatively, their model overestimates the number density of clusters and the clusters' shape did not match with the images provided by the laser-sheet visualization equipment. Helland *et al.* [229] used a similar approach to model 3-D risers focusing on the influence of inelastic particle collisions on the cluster density. They reported that low dispersion of particles during inelastic collisions (controlled by the particle-particle restitution coefficient) decreases the local porosity and enhances solid phase concentration fluctuations. A similar behavior was previously reported by Goldschmidt *et al.* [103] in their study concerning dense flows in bubbling fluidized beds. Neri & Gidaspow [8] investigated the gas-particle flow in 2-D risers operating with FCC particles (Geldart A particles with diameter of d_p=75μm) at several solid throughflow rates by using the two-fluid granular temperature model. Their careful study regarding radial solid concentration, solid flux oscillations and time-averaged solid concentration led to reliable values for the granular temperature (and consequently the solid viscosity) as a function of physical system parameters. They compared the dynamic behavior of such simulated risers, in cylindrical and cartesian coordinates, with experimental results. Their results suggested that the solid velocity profile can be described by a high upward flow in the core region, and a downwards and upwards stream can be observed near the wall region [4]. In addition, the granular temperature, as a measure of the mean particle agitation, is higher in the core and smaller near the walls.

In this chapter, numerical simulations of 2-D and 3-D risers operating at standard temperature and pressure are conducted in the two-fluid granular temperature model framework using the finite-element CFD code, FLUIDITY [78, 11]. The influence of the

collisional-energy dissipative parameters, such as particle-particle, particle-wall and friction coefficients on the granular hydrodynamics are also analyzed. Moreover, the formation and break-up of clusters within the domain is investigated through analyzing the spatial/temporal power spectra density. The regime flow is also studied with deterministic chaos theory. Although the TFM was used to model the gas-solid flow, passive tracers in the form of zero mass Lagrangian particles were added to the system to investigate the motion of particles and their influence on the bouncing clusters.

9.2 Description of the Numerical Experiments

In this work, numerical simulations conducted in 2-D and 3-D cartesian geometry were performed. Glass Ballotini particles with diameters of 500 μm along with air were fed into the domain at a constant throughflow rate and inlet gas velocity. After the initial loading of particles, a quasi steady-state is reached from which the analysis described here was performed. Initial conditions and general configurations used in the simulations are described in Table 9.1. In the 2-D simulation, a riser of diameter 15.24 cm and of height 100.0 cm is loaded with particles at a throughflow rate of 40.0 kg.m^{-2}.s^{-1}. The inlet superficial gas velocity was 4.0 m.s^{-1}. The 3-D simulation was conducted in a riser of diameter of 7.62 cm, and a height 100.0 cm. Physical properties of both phases are described in Table 9.2.

As a boundary condition, zero shear stress conditions were applied to the solid phase at the top of the domain,. Wall boundary conditions for the particulate phase described in [80] were used in these simulations. Air, at standard temperature and pressure, was modelled as a compressible Newtonian fluid, assuming ideal gas behavior. In addition, both the fluid and solid phases are free to leave the domain through the top boundary.

9.3 2-D Numerical Simulations

In this section, the numerical results obtained from 2-D simulations are analyzed and the influence of dissipative energy parameters on the granular flow dynamics is inves-

2-D riser diameter (m)	0.1524	2-D riser height (m)	1.00
3-D riser diameter (m)	0.0762	3-D riser height (m)	1.00
Inlet gas velocity ($m.s^{-1}$)	4.00	Solid throughflow rate ($kg.m^{-2}.s^{-1}$)	40.00
Initial porosity	0.03	Initial temperature and pressure	20.0^{o}C 1 bar
Particle-particle restitution coefficient (e_{pp})	0.97	Particle-wall restitution coefficient (e_{wp})	0.90
Friction coefficient (μ)	0.14		
2-D Grid (0.1524×0.10 m)	20×131	3-D Grid (r= 0.0381; z=0.10 m)	10×10×60 (1664 elements)

Table 9.1: General systems configurations and initial conditions.

	Solid Phase	**Gas Phase**
Density ($kg.m^{-3}$)	2.66×10^{3}	ideal gas law
Particle Diameter (m)	5.00×10^{-4}	–
Dynamic Viscosity ($kg.m^{-1}.s^{-1}$)	–	9.99×10^{-9}

Table 9.2: Physical properties of the solid (glass Ballotini particles) and gas (air) phases.

tigated. In addition, the formation and breakup of clusters are studied through power spectra density of pressure and voidage fluctuations.

All the simulations were initialized with a uniform solid volume fraction of 0.03. Although the simulations were performed over 175 seconds of riser operation, only the final 28 seconds were used to analyze the dynamics at a statistically steady state. This time-window was chosen based on the power spectra densities (PSD) of the time series of the voidage fluctuations, recorded at several detectors placed within the domain. The time series analysis described in the remainder of this section were performed using the data obtained from the 28 seconds time window. All the results shown here were obtained from simulations using particle-particle, wall-particle restitution coefficients and friction coefficients of 0.97, 0.90 and 0.14, respectively. In Section 9.3.3, the influence of energy dissipative parameters on the hydrodynamics is investigated by changes in the particle-particle and the wall-particle restitution coefficients (see Table 9.3). However simulations presented in Sections 9.3.1 and 9.3.2 are performed with the energy dissipative parameters described in Table 9.1.

9.3.1 Testing for Stationarity

In the transient regime, the initial loading of particles and their large concentration in the upper region of the risers results in strong oscillations in the particle concentration and redistribution in the remainder of the domain. During this regime, the riser content becomes increasingly dense until the quasi steady-state regime is reached. All analysis on the dynamics is performed after such a regime is reached. Thus, stationarity tests were performed on the time series of voidage fluctuations to ensure that the dynamical results obtained were statistically steady.

Despite extensive efforts to improve the results obtained from numerical simulations by the development of new numerical techniques, comparisons of such results and those obtained from experiments are still difficult, since only statistical quantities can be properly compared [43, 44]. As the granular flow in fluidized beds is chaotic, dynamic analysis has been applied to time series of either voidage or pressure fluctuations to identify flow

regime (e.g. bubbling and slugging bed). Reviews of chaos theory can be found in [47] (see [113] for a overview of the dynamic tools applied to the study of fluidized beds). One of the first works published on chaos theory applied to fluidized beds, by Baskakov *et al.* [140], associated pressure fluctuations with bubbles flowing around pressure transducers. Huilin *et al.* [43] used pressure fluctuation data, obtained from a lab-scale CFB, to calculate the correlation dimension, which can be defined as a measure of the spatial homogeneity of an attractor. They used the correlation dimension to infer the *real dimensionality* of a system and to establish the number of differential equations that are needed to describe a system. They also used Lyaponov exponents to determine how chaotic different fluidization regimes can be.

Dynamic systems that display chaotic behavior can only be analyzed through statistical methods. The set of differential equations used to describe such systems are time-dependent. However, the solution eventually tends to become time-independent, i.e., reaches stationarity. Once stationarity is reached, statistical analysis can be performed. Many researchers have addressed the issue of establishing when stationarity has been reached, from which statistical analysis can be performed.

Stationarity is defined as a property in which the mean and the variance of a given time series do not change over a period of time. This means that the dynamic properties of the systems underlying signal must not change during that period of time, and over short time intervals, the variance should not vary significantly [142]. Stationarity is classified into weak stationarity, which has a constant mean and variance, and strong stationarity, where all higher-order moments are constant.

Several statistical tests for stationarity have been proposed in the literature [142, 143]. In most of these tests, a set of parameters (for example, power spectrum, mean or variance) are calculated using different segments of the time series. The parameters are evaluated and if the variation among them is significant, i.e., beyond an estimated deviation, the time series is assumed to be nonstationary. Kennel [144], however, used the information obtained from time distribution of points in a state space to infer stationarity. His method investigates the geometry of orbits in state space by quantifying nonstationarity from the properties of nearest neighbors in state space. Schreiber [145] tested for stationarity by

checking for compatibility of nonlinear approximations to the dynamics in different segments of the time series.

In this work, the power spectra density (PSD) of several fragments of data of solid volume fraction fluctuations were calculated. The dominant frequency and overall behavior of the set of PSDs were compared, and if no large shift to any side was found, the dynamics were assumed to have reached stationarity.

Power spectra densities of solid volume fraction fluctuations of 2-D simulations were calculated from data collected at several positions within the domain during 174.37 seconds. This set of data was split into six fragments, and the PSDs of each were calculated (Figure 9.2). These PSDs were obtained from a detector placed near the wall and at 30.0 cm above the inlet region.

Three dominant frequencies are present: 0.5, 1.0 and 4.0 Hz. Although the larger dominant frequencies are very similar, at approximately 4.0 Hz, shifts towards lower and higher frequencies occur, i.e., 5.0 Hz for a time-window of 50.73$\leq t \leq$69.98 s, 3.0 Hz for 70.05$\leq t \leq$94.99 s, 3.5 Hz for 98.0$\leq t \leq$142.85 s and, 4.1 and 3.9 Hz for 146.37$\leq t \leq$159.87 s and 160.0$\leq t \leq$174.37 s, respectively. These small shifts in the latter two time-windows indicates that the system has reached stationarity. Therefore, in the remaining of this work, all the analysis are conducted within the last time-window (146.37 $\leq t \leq$ 174.37 seconds).

9.3.2 Formation and Breakup of Clusters of Particles

After the initial particle loading, when the riser contents become denser, a quasi steady-state regime is reached and a quasi-periodic established behavior. Particles move upwards and can either leave the domain, or fall in the near wall region. As they fall, they may collide with rising particles and form particle clusters which vigorously move upwards and downwards. As the clusters fall and crash against the bottom region, the particle clusters break up and splash onto the opposite wall, passing through the center line of the riser and promoting strong recirculation and mixing. Such behavior is shown in the sequence of frames in Figure 9.3.

The cluster motion may also be observed through the investigation of the time-averaged

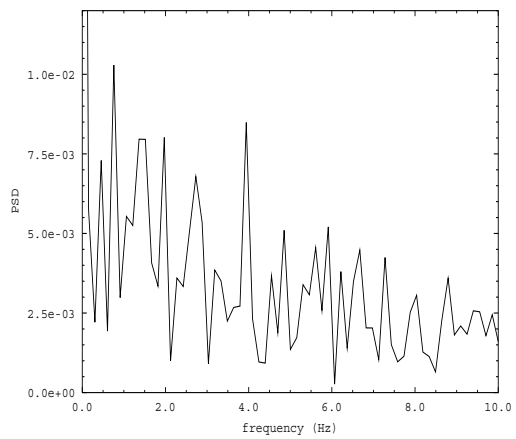

(a) $0.00 \leq t \leq 6.60$ s

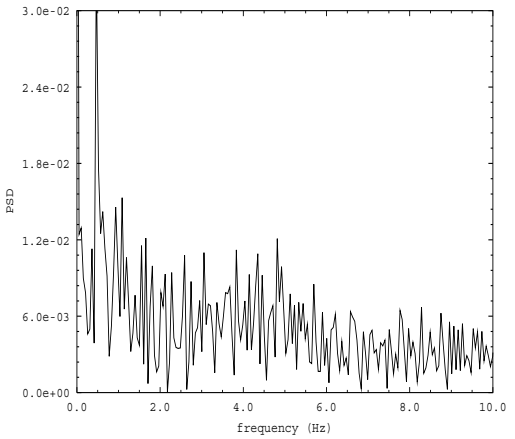

(b) $50.73 \leq t \leq 69.98$ s

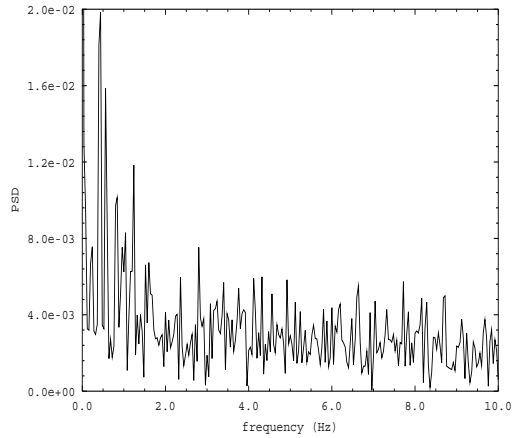

(c) $70.05 \leq t \leq 94.99$ s

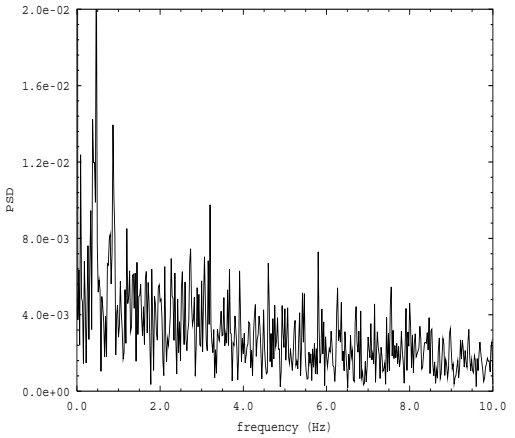

(d) $98.00 \leq t \leq 142.85$ s

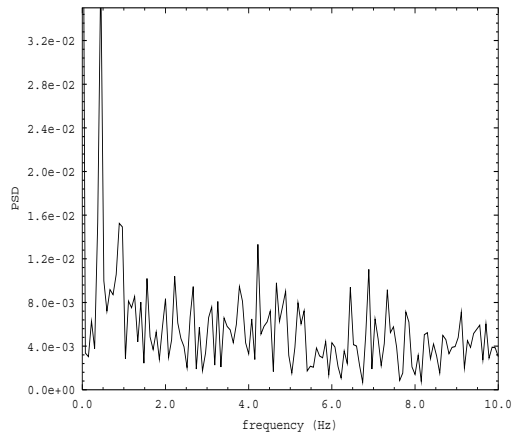

(e) $146.37 \leq t \leq 159.87$ s

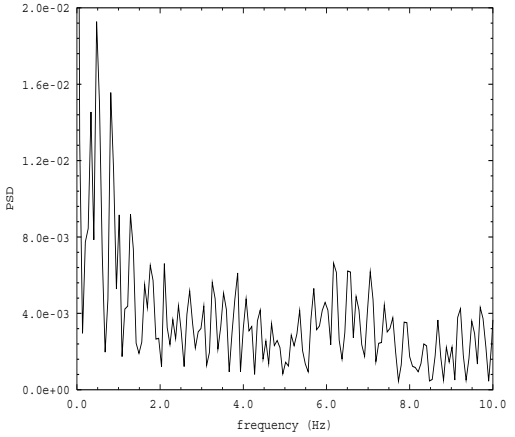

(f) $160.00 \leq t \leq 174.37$ s

Figure 9.2: 2-D Riser: testing for stationarity (Table 9.1). The PSD of solid volume fraction fluctuations obtained from a detector placed in the wall region at 30.0 cm above the bottom of the riser.

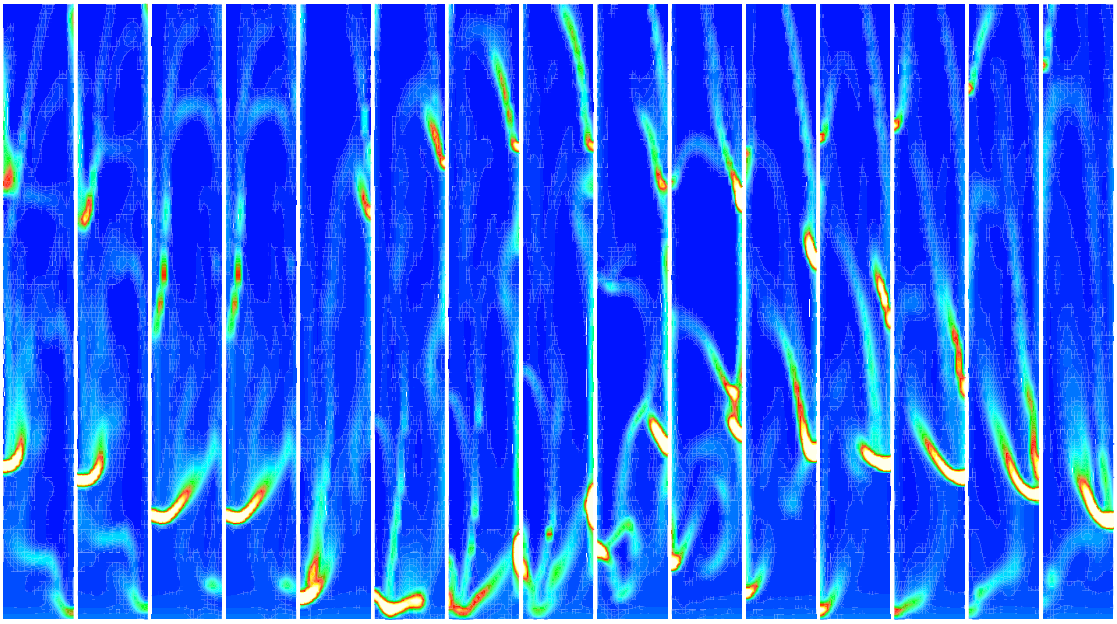

Figure 9.3: 2-D Riser: Snap-shots of the formation and break-up of clusters. The solid volume fraction distribution is drawn every 0.1 seconds, starting at 155.2 seconds ($e_{pp} = 0.97,\ e_{wp} = 0.90,\ \mu = 0.14$).

solid volume fraction, solid vertical velocity and granular temperature shown in Figures 9.4, 9.5(a) and 9.6, respectively. At 1.0 cm above the bottom inlet boundary, a flat solid velocity profile can be seen due to the uniform solid throughflow rate. However as the distance from the inlet boundary increases, larger solid velocities in the core region and lower (and eventually negative) velocities in the wall region are observed. Such time-averaged behavior agrees with the experimental results reported by Neri & Gidaspow [8] (and also in [4, 229, 10]) in which particle annular flows were noticed.

As indicated by the time-averaged granular temperature at the wall and central regions, shown in Figures 9.6(a) and (b), respectively, increased uniform kinetic energy dissipation occurs near the wall. Since the core region has a lower particle concentration, the time-averaged granular temperature is lower than in the wall region. However, in the upper regions, i.e., at the exit zone, large granular temperatures may be seen in the core region. In addition, the bouncing of particles at the exit zone may lead to either particles falling back into the domain or leaving it unhindered. The overall results obtained from this simulation qualitatively agree with the granular flow behavior reported by Huilin *et al.*

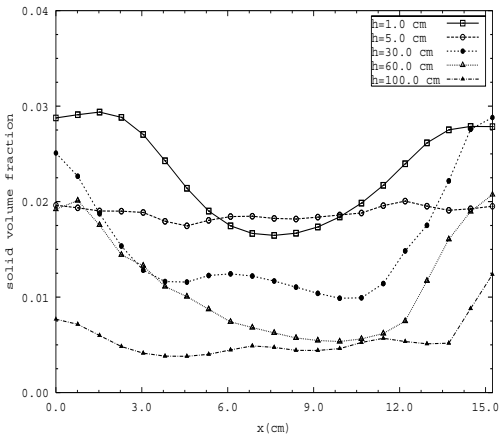

Figure 9.4: 2-D Riser: Time-averaged solid volume fraction at several heights along the domain (Table 9.1).

[10], in which a core-annular structure characterizes the flow, i.e., in a time-averaged sense, particles are concentrated in the wall region (see Figure 9.4), whereas in the core, larger velocities promote fast particle transport.

Most of numerical studies of risers dynamics were conducted after a quasi-steady state was reached. However, establishing this regime is still an issue, due to the high computational costs associated with such long simulations. Therefore, most of the analysis available in the literature used data obtained after 20-50 seconds of simulation [226, 8]. Although all analysis in this work was performed after stationarity was reached, a brief comparison between the particle flow behavior in the first 108 seconds (Figure 9.7) and in the last 10 seconds (Figure 9.8) of numerical simulation was conducted. The results shown in these figures were obtained from a cross section at a height of 30.0 cm above the bottom inlet boundary. A uniform solid volume fraction can be observed (Figure 9.7(a)) although large peaks in the wall region at two snapshots (60.20 and 96.24 seconds) may represent a transient behavior or a cluster passing through the region. However, as indicated by Figure 9.7(b), there are no significant increases in the granular temperature for these snapshots (except at the start up of the simulation, where a flat granular temperature profile is observed due to the initial conditions). The vertical solid and gas velocities (Figures 9.7(c) and (d), respectively) have, however, similar magnitudes.

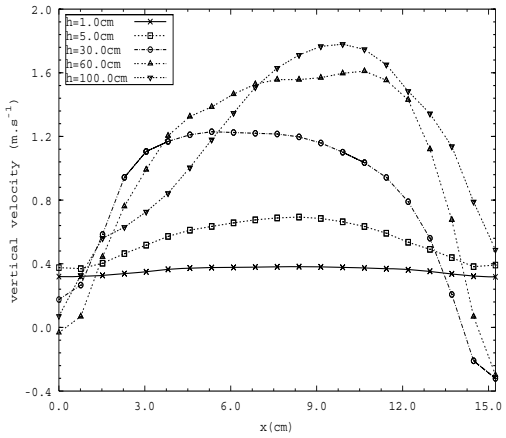

(a) v8

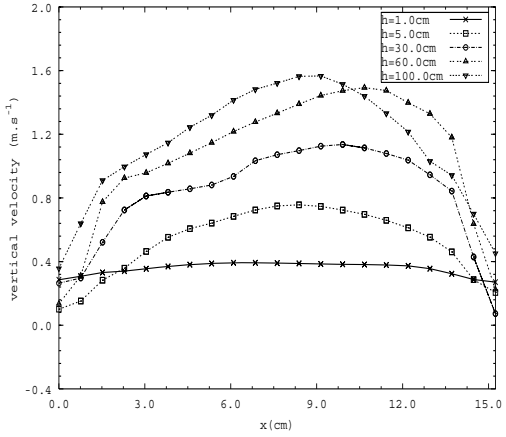

(b) v9

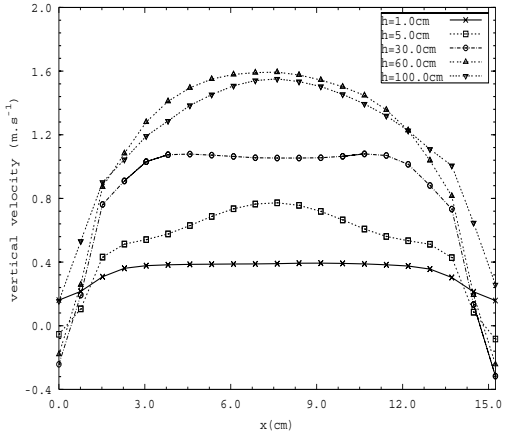

(c) v10

Figure 9.5: 2-D Riser: Time-averaged solid vertical velocity at several heights along the riser (Table 9.3).

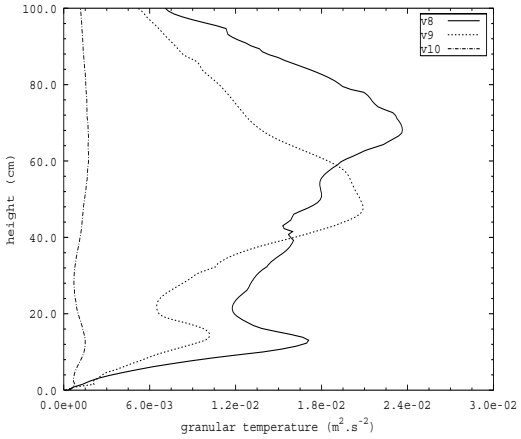

(a) wall region

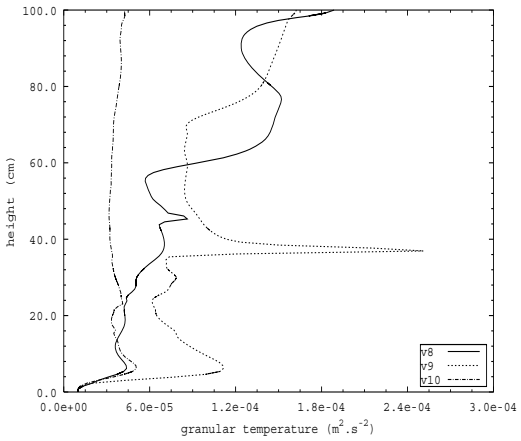

(b) center

Figure 9.6: 2-D Riser: Time-averaged granular temperature at the (a) wall region and at the (b) center (Table 9.3).

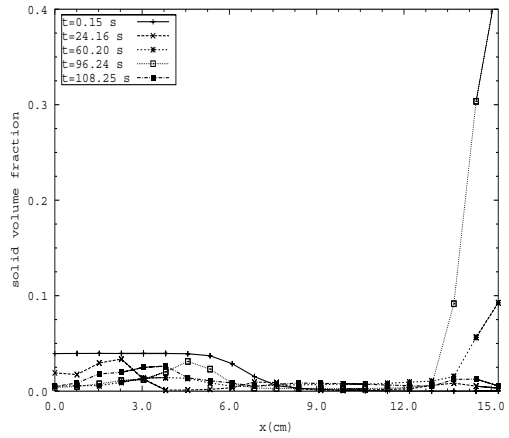

(a) solid volume fraction

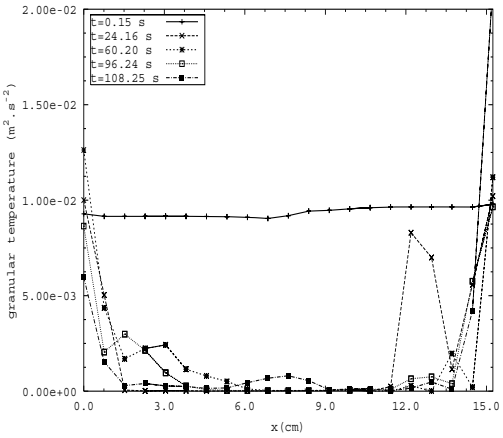

(b) granular temperature

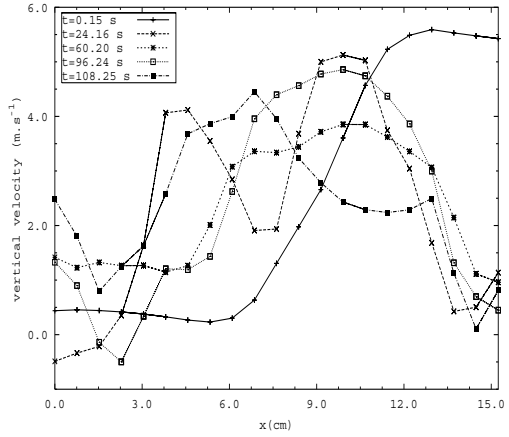

(c) vertical gas velocity

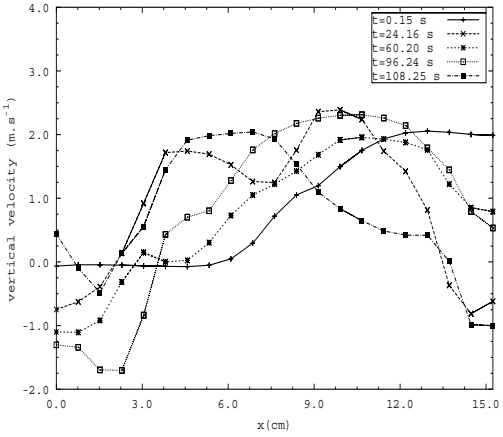

(d) vertical solid velocity

Figure 9.7: 2-D Riser: Several fields within the first 108 seconds of simulation at 30.0 cm above the bottom inlet boundary (Table 9.1).

The time-averaged solid volume fraction shown in Figure 9.4 reveals a larger particle concentration in the wall region than at the core. Such behavior is not as clear in the solid volume fraction snapshots shown in Figure 9.8(a), due to the large nonuniformity of the flow during the motion of the clusters. However, it is observed through the PSD (Figure 9.9) of voidage fluctuations measured at four detectors located at 30.0 and 80.0 cm above the bottom inlet boundary. They were placed at the wall and center regions. The detector located at 30.0 cm above the bottom inlet boundary and in the center region (Figure 9.9(a)) exhibits a dominant frequency of approximately 1.0 Hz, and a second large peak between 3.5 and 4.0 Hz. At the same height, but in the wall region (Figure 9.9(b)) the dominant frequency is 0.5 Hz and the second largest peak is between 2.0 and 2.5 Hz, i.e., approximately half of that observed at the center region. A similar behavior is noticed for the PSD obtained from detectors placed at a height of 80.0 cm above the bottom inlet boundary (Figures 9.9(c) and (d)). The larger voidage fluctuation dominant frequencies in the core of the risers are due to the expansion of clusters from a high packing condition to a more misty configuration away from the wall $(0.01 \leq \varepsilon_s \leq 0.30)$. This may be observed from a series of graphs, at different instances in time, of the particle concentration against granular temperature in the wall and core regions, at 30.0 cm above the bottom inlet boundary, Figures 9.9(e) and (f).

9.3.3 Influence of Energy Dissipation Parameters

Goldschmidt *et al.* [103] numerically investigated the hydrodynamics behavior of bubbling fluidized beds using particle-particle restitution coefficients in the range of 0.73 to 1.00, and compared the results obtained from these simulation with experimental results. They reported that the smaller the restitution coefficient, the more rapidly the energy dissipates through the system. Therefore, as the particle-particle restitution coefficient decreases, the fluidization becomes more vigorous, i.e., as the particle collisions become less ideal (more inelastic), more energy is dissipated. Since the particles tend to become packed in the densest regions of the bed, sharper gas volume fraction contours and larger bubbles occur here. In order to investigate the influence of the dissipative energy parameters in gas-particles dilute flows, a set of 2-D simulations were conducted using different

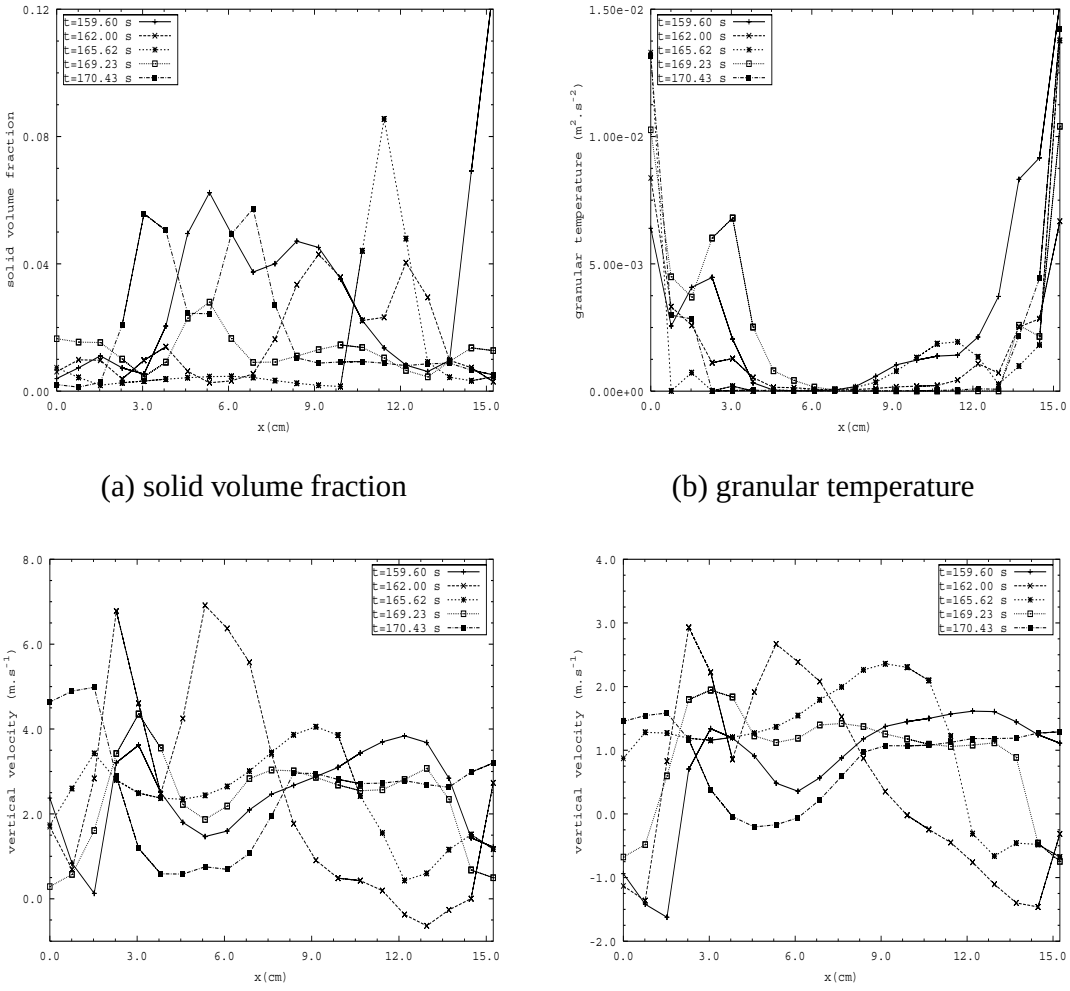

(a) solid volume fraction

(b) granular temperature

(c) vertical gas velocity

(d) vertical solid velocity

Figure 9.8: 2-D Riser: Several fields within the last 10 seconds of simulation at 30.0 cm above the bottom inlet boundary (Table 9.1).

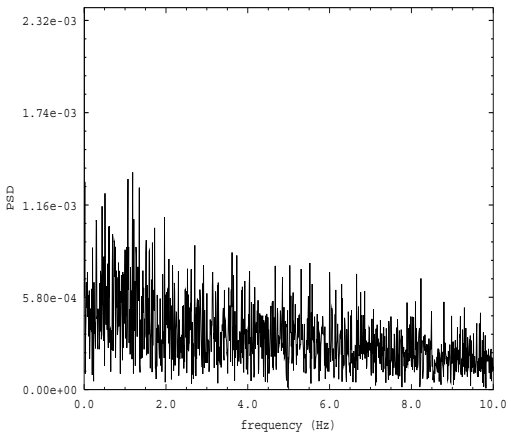

(a) PSD: central region (3.81,30.0)cm

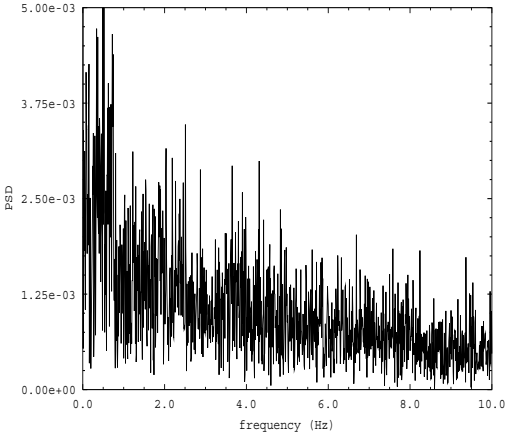

(b) PSD: wall region (0.00,30.0)cm

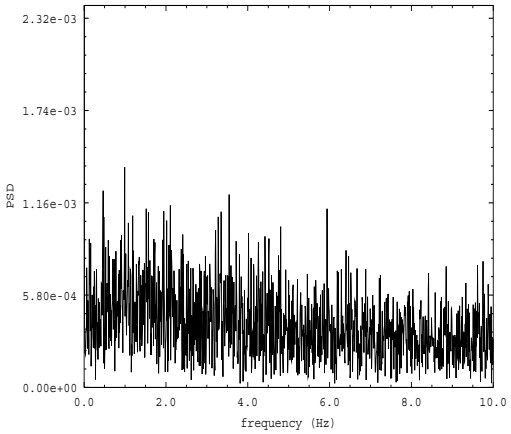

(c) PSD: central region (3.81,80.0)cm

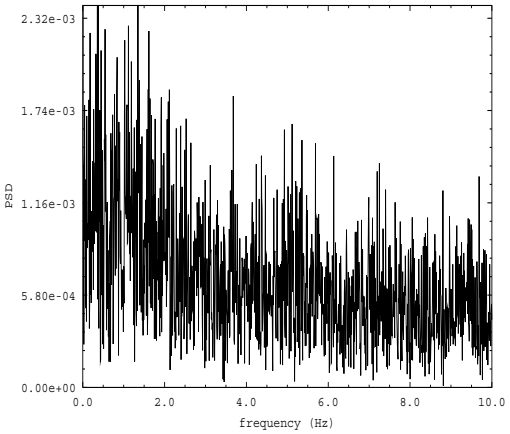

(d) PSD: wall region (0.00,80.0)cm

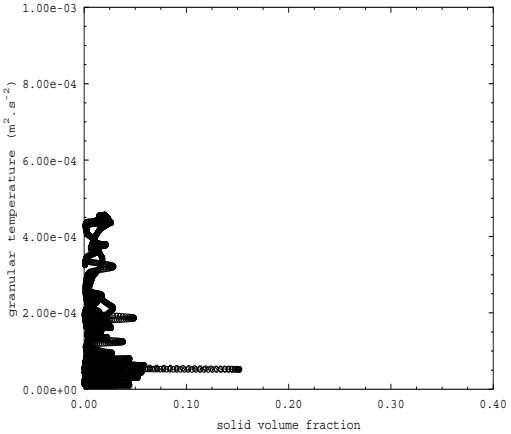

(c) central region

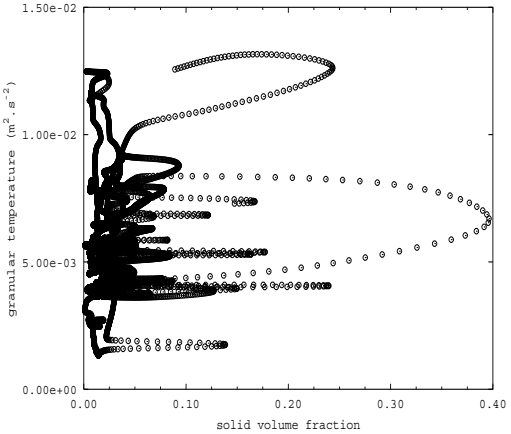

(d) wall region

Figure 9.9: 2-D Riser: (a-d) PSD of voidage fluctuation at the central and wall regions and (e-f) solid volume fraction *versus* granular temperature during 160.0≤174.3 seconds at 30.0 cm above the bottom inlet boundary (Table 9.1).

	e_{pp}	e_{pw}	μ
case v8	0.97	0.90	0.14
case v9	0.97	0.90	0.10
case v10	0.90	0.90	0.14

Table 9.3: Collision-energy dissipative parameters used in this work: particle-particle (e_{pp}), wall-particle (e_{pw}) and friction (μ) coefficients.

values for these parameters, as described by Table 9.3.

In dilute flows, however, lower particle-particle restitution coefficients lead to lower energy dissipation, as expressed by the time-averaged granular temperature shown in Figures 9.10(d) and (f). Such behavior occurs due to the low particle concentration typically found in risers ($0.01 \leq \varepsilon_s \leq 0.33$), which leads to larger granular temperatures. The granular temperature is zero in a situation where there are no particles, however it increases as the particle concentration rises, and vanishes as the particle concentration reaches maximum particle packing, where a small mean distance between the particles results in additional particle-particle collisions with lower kinetic energy dissipation [9, 8]. Therefore, in dilute flows, large volume fractions do not lead to large granular temperatures (Figures 9.10(a,c,d,f) and 9.6). In these figures, it is seen that a smaller particle-particle restitution coefficient results in larger particle concentrations and larger granular temperatures. The friction coefficient has a similar, but less pronounced effect on the flow behavior as the restitution coefficient, see Figures 9.5 and 9.10.

9.4 Investigation of Cluster Motion in 3-D Cylindrical Risers

The cluster motion in a 3-D geometry is investigated in a cylindrical riser that is 7.62 cm in diameter and 100.0 cm high (Figure 9.11(a)). Particles of diameter of 500 μm with a density of 2660 kg.m^{-3}, and air, at standard temperature and pressure, are fed into the riser with a solid mass flux of 40.0 kg.m^{-2}.s^{-1} and an inlet gas velocity of 4.0 m.s^{-1}

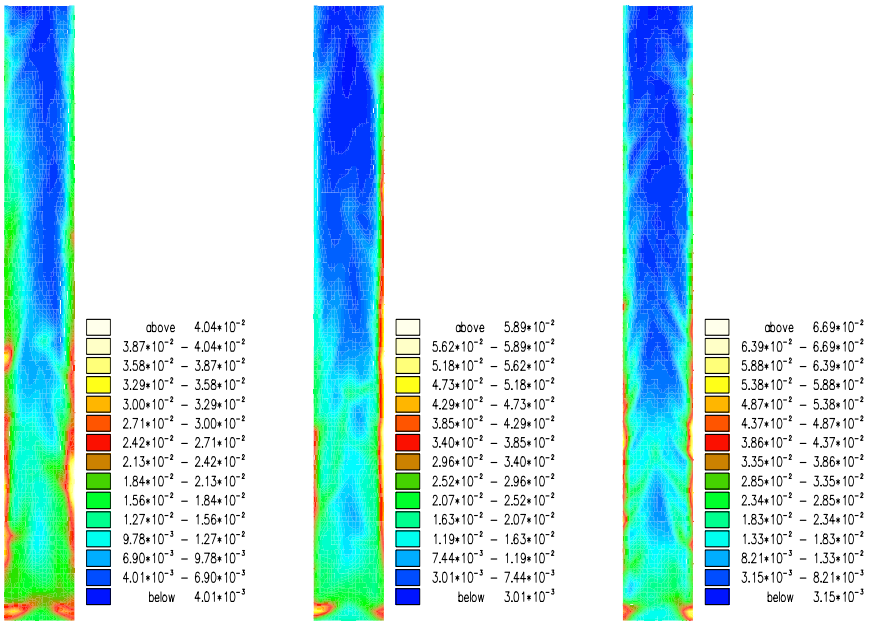

(a)v8 (b)v9 (c)v10

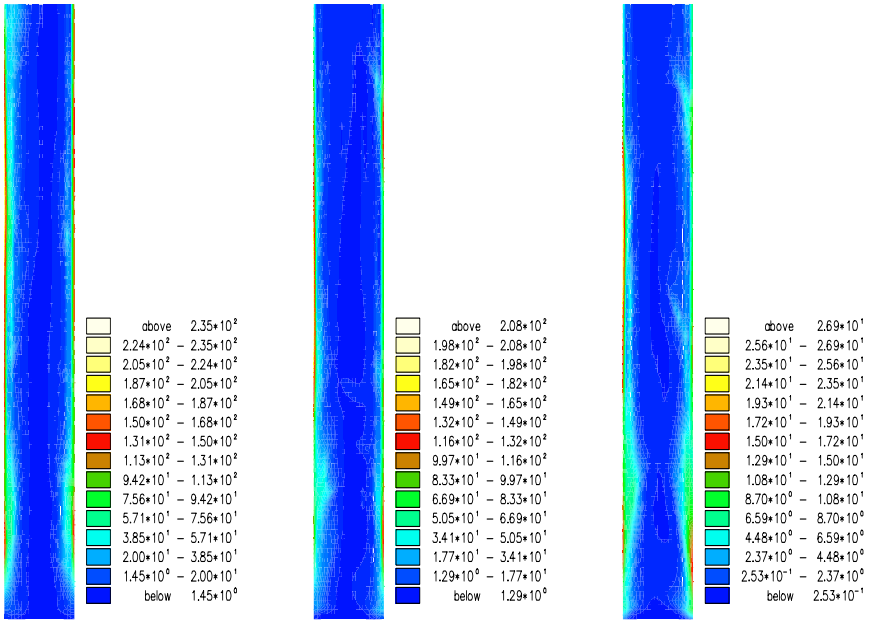

(d)v8 (e)v9 (f)v10

Figure 9.10: 2-D Riser: Time-averaged solid volume fraction and granular temperature $(\text{cm/s})^2$ for the three cases (Table 9.3), (a,d) case v8, (b,e) case v9 and (c,f) case v10, respectively. Turning the particle collisions more inelastic, $\left(e_{pp}^{v8} = 0.97, \;\; e_{pp}^{v10} = 0.90\right)$, lead to lower granular temperatures and a more vigorous flow. However, changes in the friction coefficient $(\mu^{v8} = 0.14, \;\; \mu^{v10} = 0.10)$ lead to relatively lower granular temperatures.

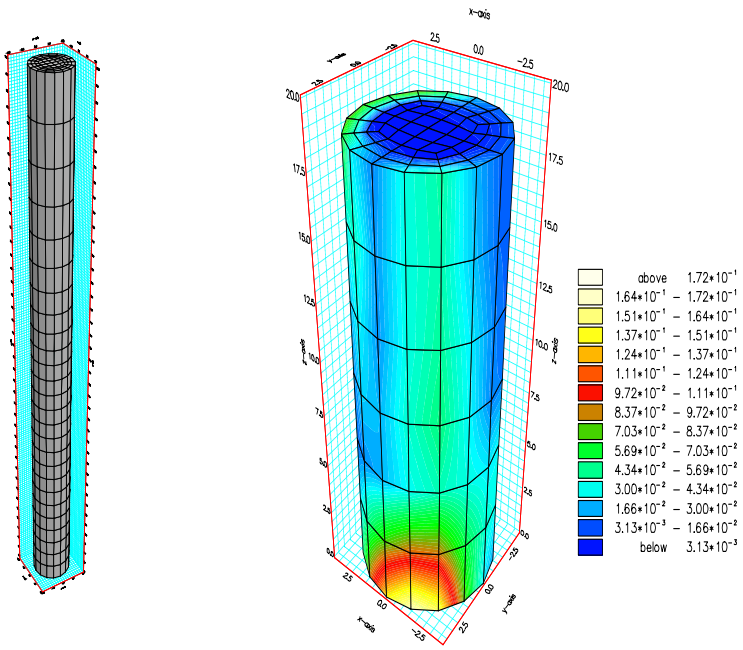

(a) schematic (b) solid volume fraction

Figure 9.11: 3-D Riser: (a) schematic (entire domain) with 1664 elements and (b) solid volume fraction at 156.0 seconds of simulation, only 20.0 cm of the domain above the bottom boundary region is shown.

(Table 9.2). The numerical simulation was performed over 168 seconds and the analysis conducted over the final 25 seconds of simulation.

The numerical results from the 2-D simulations qualitatively agreed with experiments in lab-scales risers as reported (Sections 9.3.2 and 9.3.3). In the simulations reported by Tanaka *et al.* [224], 'vertically elongated structures' similar to a parabola heading downwards, and having a thin tail upwards were observed. This description, matches the shape found in the simulations performed here, as shown in Figure 9.3. In the 3-D simulation, a similar shape in the vertical cross section of the riser at the wall region was also found (Figure 9.11(b)). In the horizontal cross section, however, several cluster shapes are reported in the literature, from spherical [230] to 'string-like' patterns [231]. In the simulation performed here, the clusters did not show a single shape in the horizontal cross section, varying from a 'quarter arc' shapes which rotate near the wall region, to

'string-like' shapes, in the core region (see Figure 9.12).

Particles commonly bounce and slip at the wall, forming a dilute disperse string-like structure in the core region. As they merge into relatively high-concentration clusters near the wall, they move upwards and downwards as shown in Figure 9.13. This set of pictures was obtained from a riser simulation in which the riser has a diameter of 0.1562 m and a height of 1.0 m and with a relatively fine mesh (27600 elements and 29341 nodes).

In order to visualize this particle motion, massless particles were introduced into the particle phase and tracked in time and space in a Lagrangian manner. The particle paths are calculated by integrating from a starting point through the time varying Eulerian velocity field. The integration was performed using a first order forward Euler time stepping, subsampling time between successive velocity fields. This approach is equivalent to performing a Lagrangian simulation with massless, non-interacting particles. The tracer particles were therefore rendered as spheres within the domain, with scalar and velocity values sampled at those locations from the original Eulerian solution. In the set of frames in Figures[1] 9.14 and 9.16, massless particles, representing the solid volume fraction distribution $(0.01 \leq \varepsilon_s \leq 0.31)$, are continuously fed into the domain from the bottom. These particles tend to agglomerate near the wall region and move, initially, upwards. Such preferable motion towards the wall region may be visualized through the radial distribution of particles in Figures 9.15 and 9.17. In this set of frames, the colours represent the initial radial position of particles. Thus, initially, the massless particles are uniformly distributed near the bottom region. As the simulation evolves in time, particles move preferentially towards the wall and agglomerate in the wall region. In addition, particle clusters seem to spin up and down near the wall region, due to large velocities, and mix as the simulation evolves in time.

The particle flow in the wall region is also investigated with the PSD of voidage fluctuations shown in Figures 9.18. Dominant lower frequencies in the range of 0.6 and 1.25 Hz were found in both the wall and core regions and at 25.0 and 50.0 cm above the bottom inlet boundary. Unlike the results obtained from the 2-D simulations (Figures 9.9(a)-(d)) in which the dominant frequencies in the core region were approximately twice the

[1] See also the animation in the attached CD-ROM.

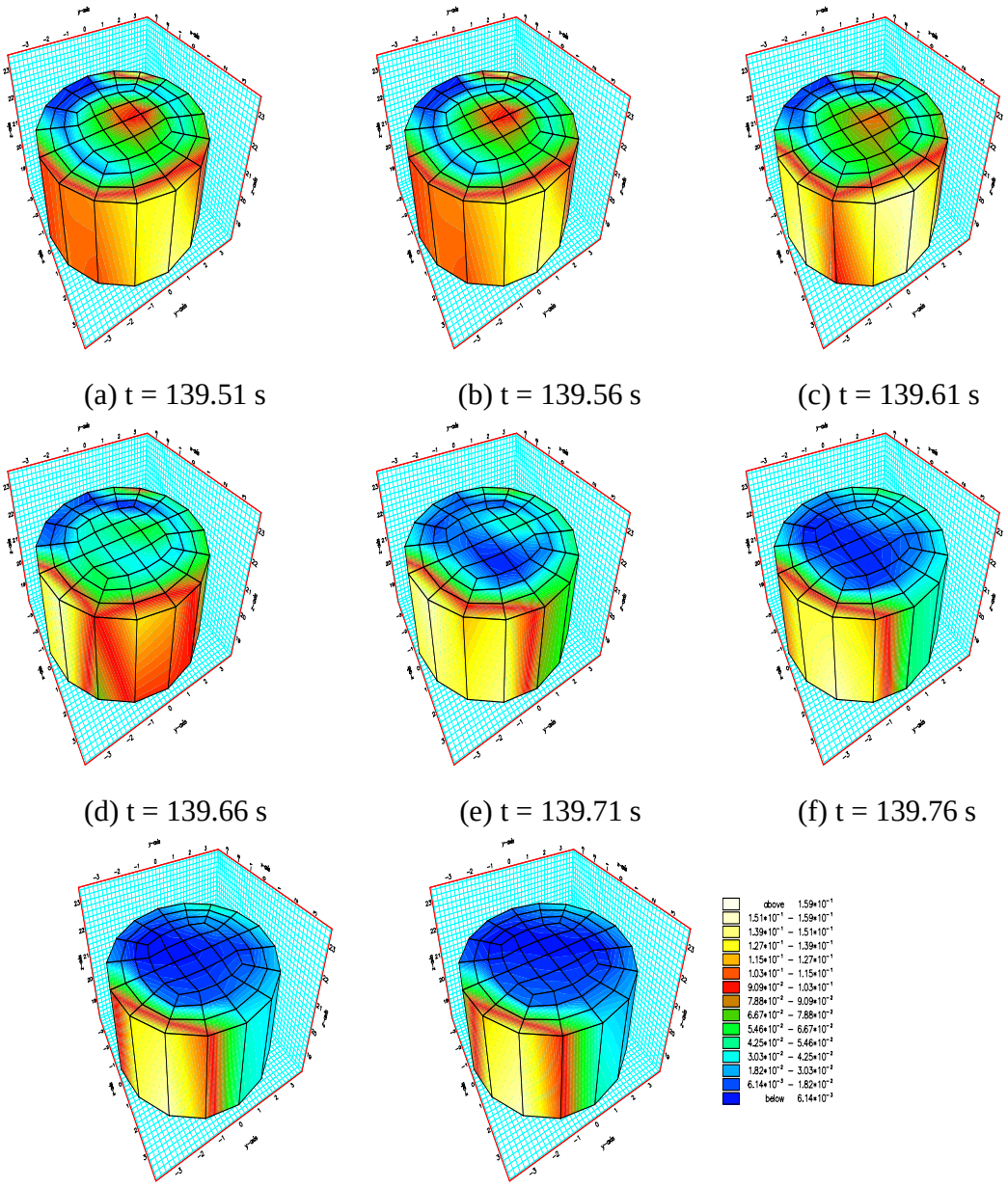

(a) t = 139.51 s (b) t = 139.56 s (c) t = 139.61 s

(d) t = 139.66 s (e) t = 139.71 s (f) t = 139.76 s

(g) t = 139.81 s (h) t = 139.86 s

Figure 9.12: 3-D Riser: Horizontal cross-sections showing the cluster motion (solid volume fraction) at a height of 23.0 cm above the bottom inlet boundary.

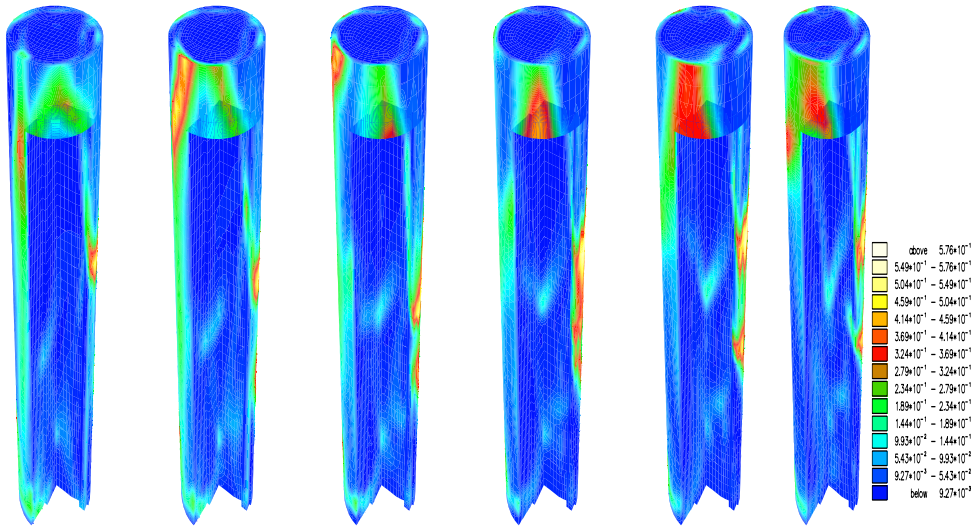

Figure 9.13: 3-D Riser: Set of frames drawn every 0.04 seconds starting at 3.38 seconds of the fine mesh simulation. The riser has a diameter of 0.1562 m and a height of 1.0 m, however, only the lower region, i.e., up to 0.03 m is shown. A slice is removed from the domain in order to visualize the cluster motion through the central region.

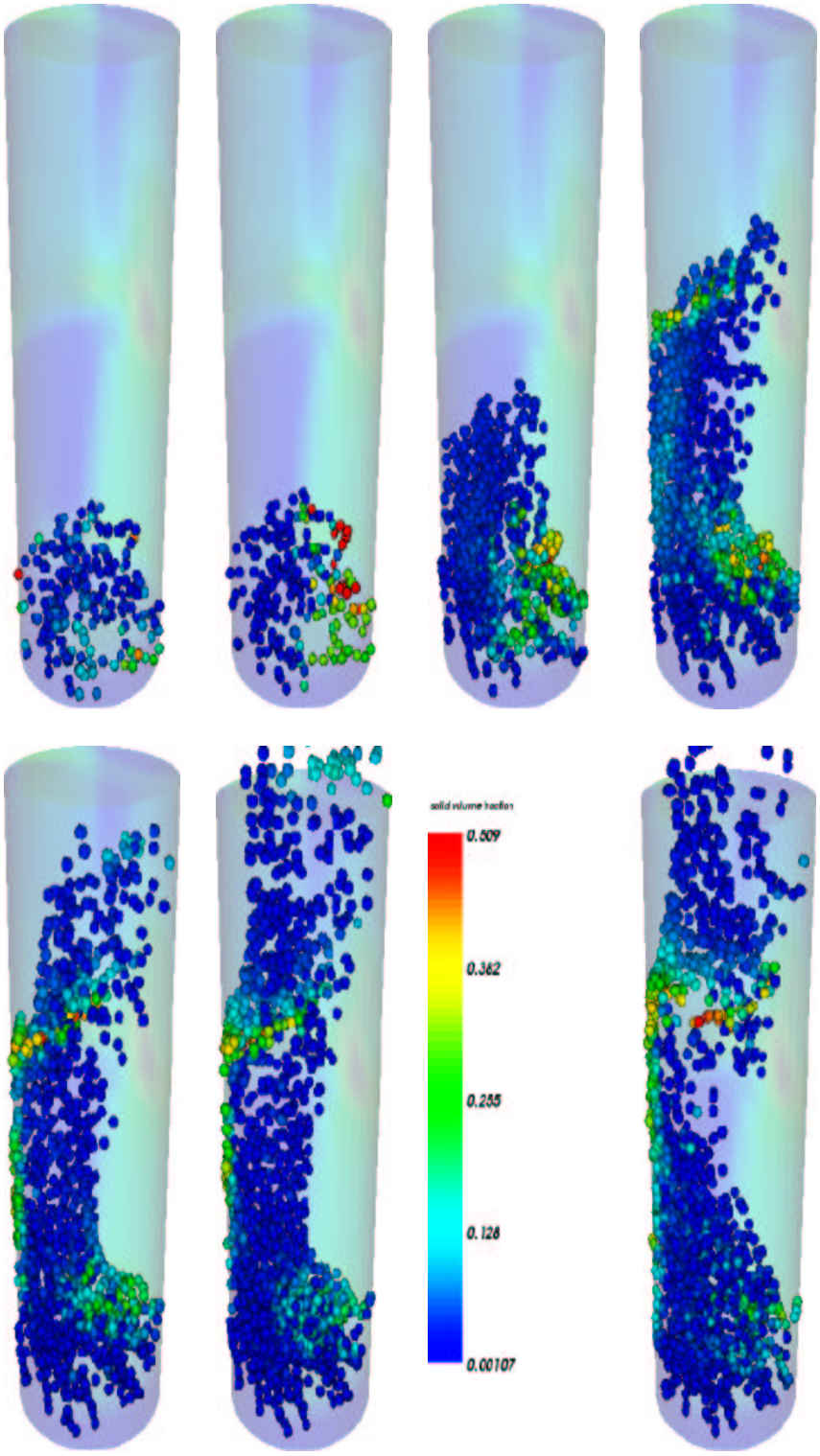

Figure 9.14: 3-D Riser: massless particles showing particles motion. This riser has a diameter of 0.1562 m and a height of 1.0 m. In this figure, however, just the lower half of the height is shown. The snapshots were drawn every 0.075 seconds starting from 0.025 seconds.

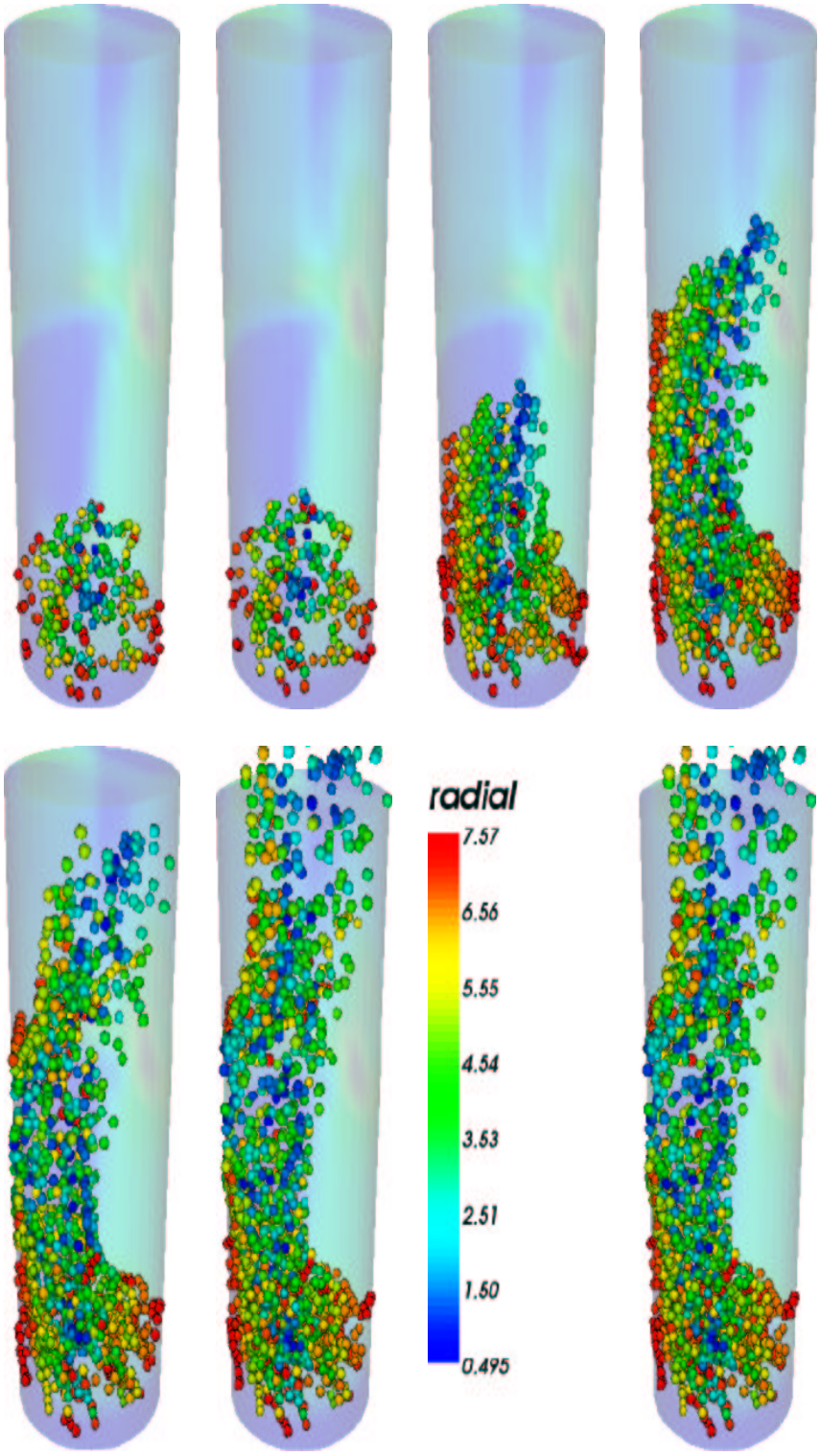

Figure 9.15: 3-D Riser: massless particles showing the distribution of particles along the radial axis. The colors represent the initial radial positions. This riser has a diameter of 0.1562 m and a height of 1.0 m. In this figure, however, just the lower half of the height is shown. The snapshots were drawn every 0.075 seconds starting from 0.025 seconds.

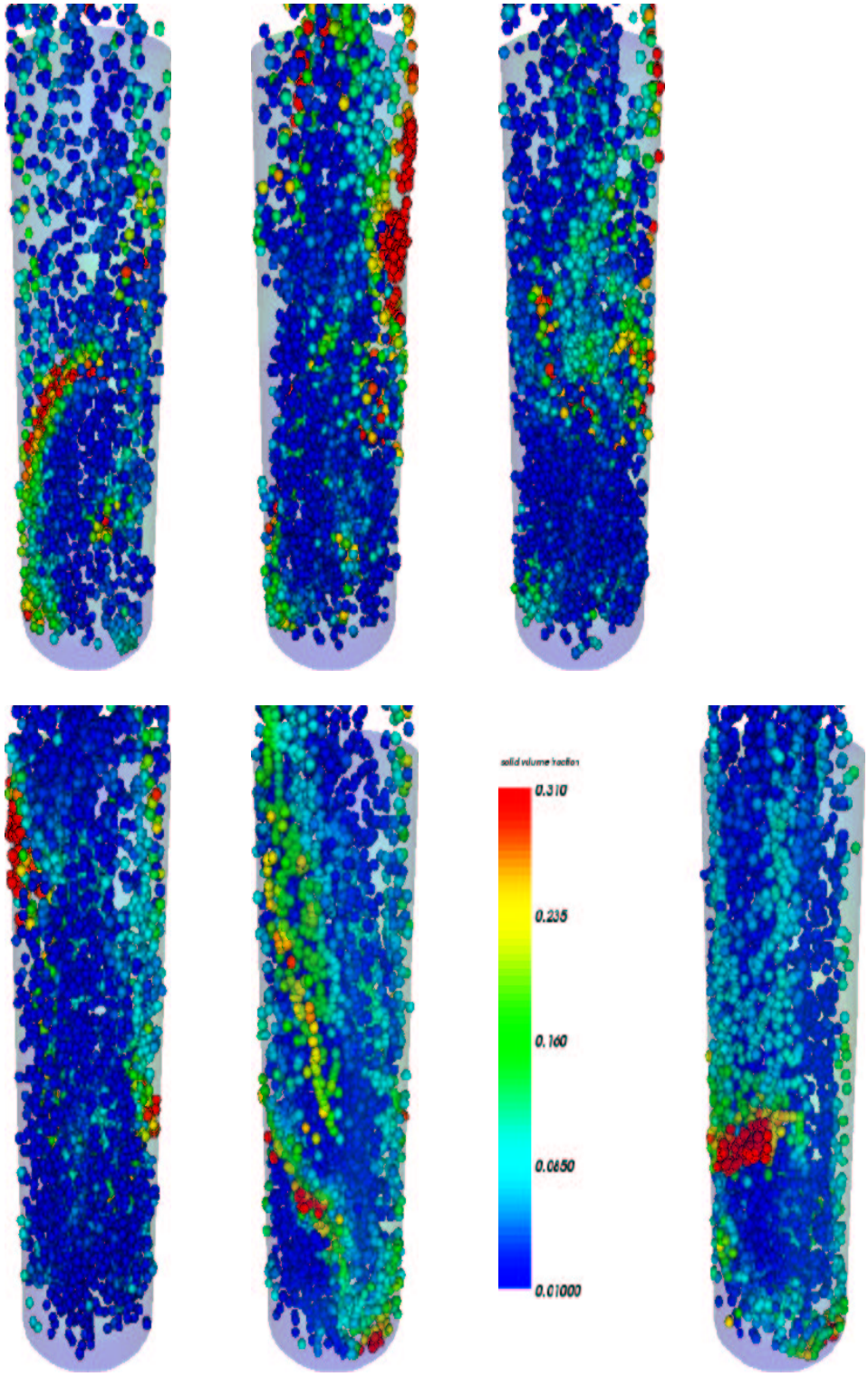

Figure 9.16: 3-D Riser: massless particles showing particles motion. This riser has a diameter of 0.1562 m and a height of 0.10 m. In this figure, however, just the lower half of the height is shown. The snapshots were drawn every 0.175 seconds starting from 3.37 seconds.

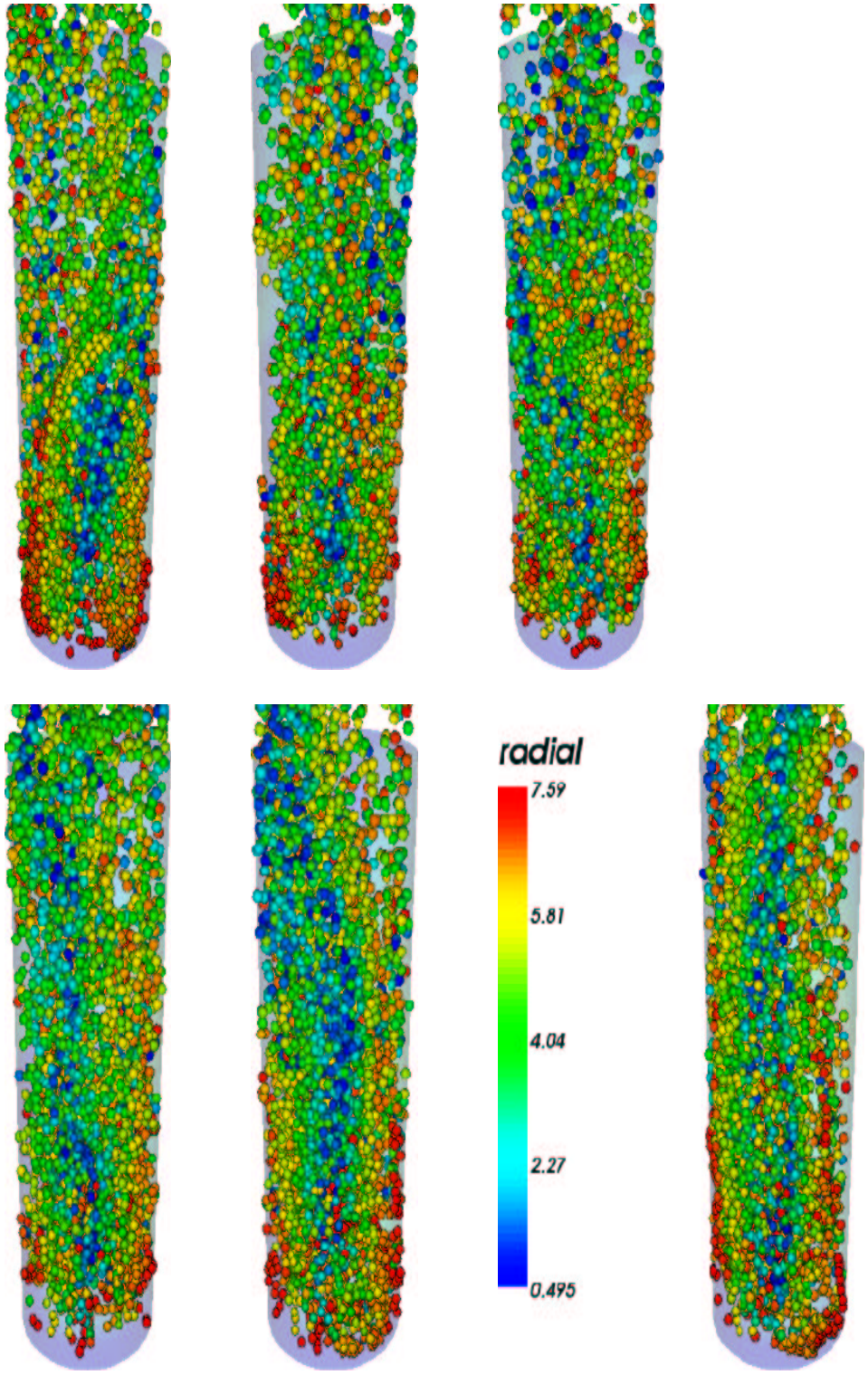

Figure 9.17: 3-D Riser: massless particles showing the distribution of particles along the radial axis. The colors represent the initial radial positions. This riser has a diameter of 0.1562 m and a height of 0.10 m. In this figure, however, just the lower half of the height is shown. The snapshots were drawn every 0.175 seconds starting from 3.37 seconds.

dominant frequency in the wall region, no proportionality between the PSD of voidage fluctuations was noticed in the 3-D simulation. This is possibly due to the lower numerical resolution obtained from the coarse mesh used in this simulation. However, in both 2-D and 3-D simulations, the amplitude of the PSD of voidage fluctuations at the wall region were larger than those at the core region. As the voidage in dilute flows does not show large fluctuations, the PSD sensitivity to cluster flows, with a solid concentration ranging from $0.01 \leq \varepsilon_s \leq 0.30$, is remarkably low. Therefore, solid vertical velocity was chosen to investigate the cluster motion within the domain. The PSD of the vertical solid velocities obtained from three detectors placed at 25.0 and 50.0 cm above the bottom inlet boundary distributed over the core and wall regions, are shown in Figure 9.19(b-d). The dominant frequency obtained from the detector, at the core and wall regions, was 1.00 and 0.50 Hz, respectively. Both PSDs also have secondary smaller peaks of 3.0 and 4.0 Hz (Figure 9.19(c)) and 1.75 and 2.5 Hz (Figure 9.19(d)) respectively. This qualitatively agrees with the PSD of voidage fluctuations obtained from the 2-D simulations, in which the dominant frequency in the wall region is half the dominant frequency found in the core region. In addition, the amplitude of the PSD obtained at the wall region was larger than the one obtained in the core region.

9.5 Investigating Flow Structure Through Chaos Theory

The solution of the partial differential equations that describe the coupled fluid-particle flows are time and space dependent, and very sensitive to initial conditions. Any small perturbation applied to the initial conditions leads to different solution; such behavior being a characteristic of chaotic systems [46, 47]. Deterministic chaos theory has been used by a number of researchers to establish flow regime and structure in both dense[45, 209, 215] and dilute flows [43, 232, 233]. The application to dense flows has been discussed in Sections 5.6 and 8.6.

The flow regime and macrostructure of CFBs has been investigated by Johnsson *et al.* [113] through pressure fluctuations obtained from transducers. Their work focused on the flow at the bottom region of a riser, in which, by controlling the solid mass flux

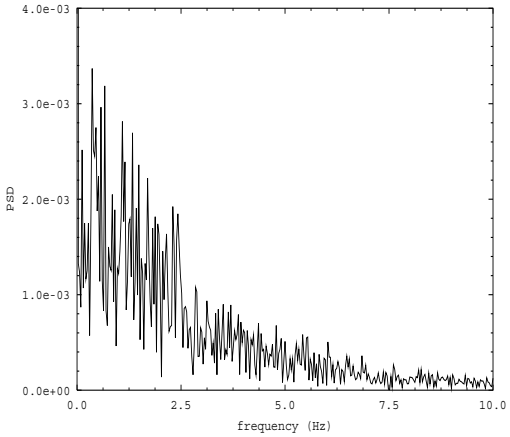

(a) central region (h = 25.0 cm)

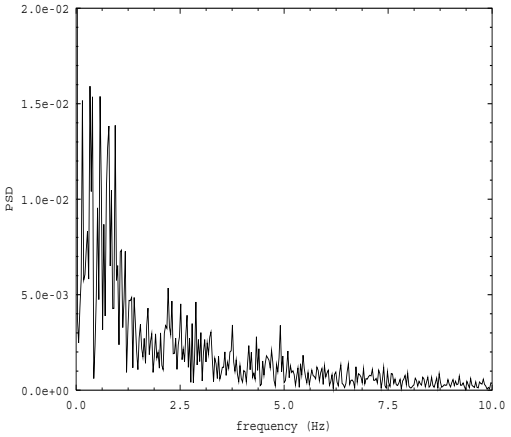

(b) wall region (h = 25.0 cm)

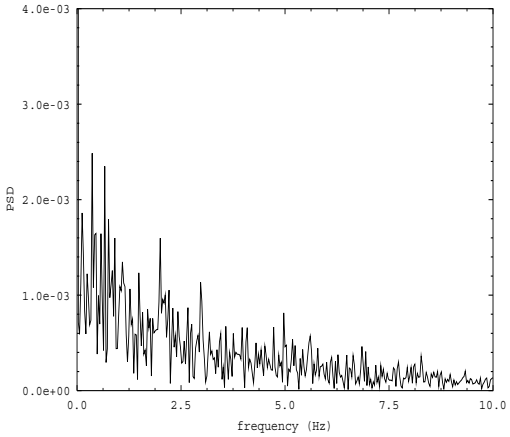

(c) central region (h = 50.0 cm)

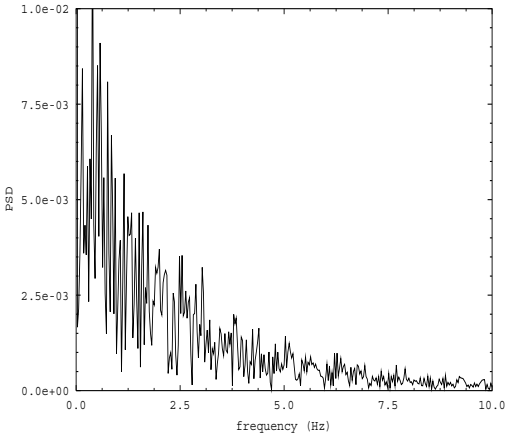

(d) wall region (h = 50.0 cm

Figure 9.18: 3-D Riser: PSD of voidage fluctuations at four detectors within the domain.

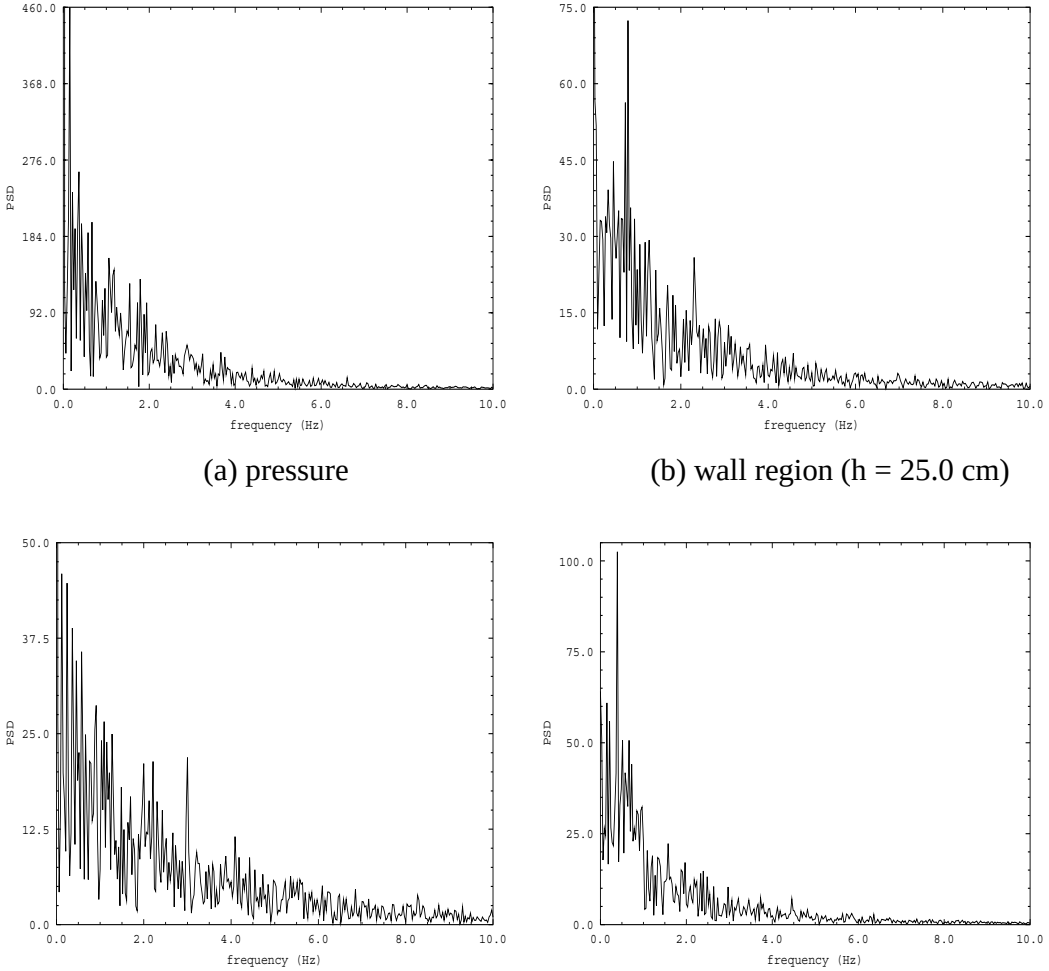

(a) pressure (b) wall region (h = 25.0 cm)

(c) core region (h = 50.0 cm) (d) wall region (h = 50.0 cm)

Figure 9.19: 3-D Riser: PSD of (a) pressure fluctuations at the center region at 5.0 cm above the bottom boundary and (b-d) vertical solid velocity fluctuations at 3 detectors.

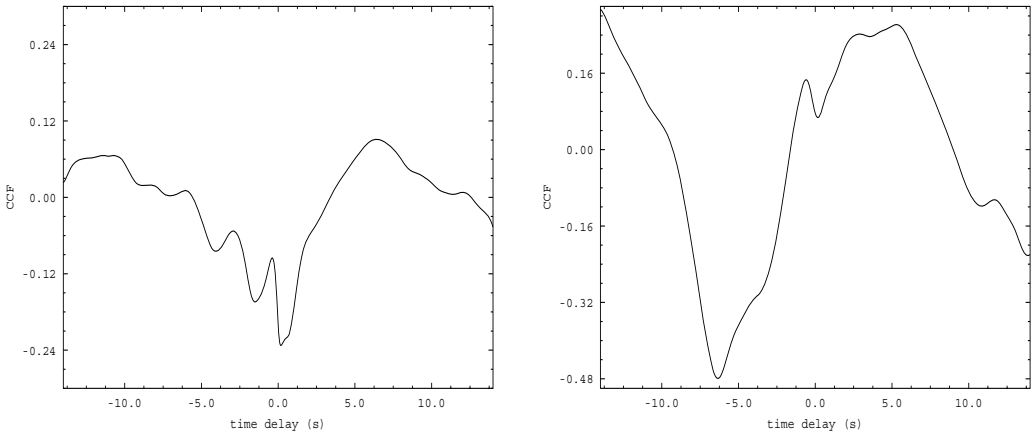

(a) central region (-0.42/1.50) (b) wall region (-0.65/2.57)

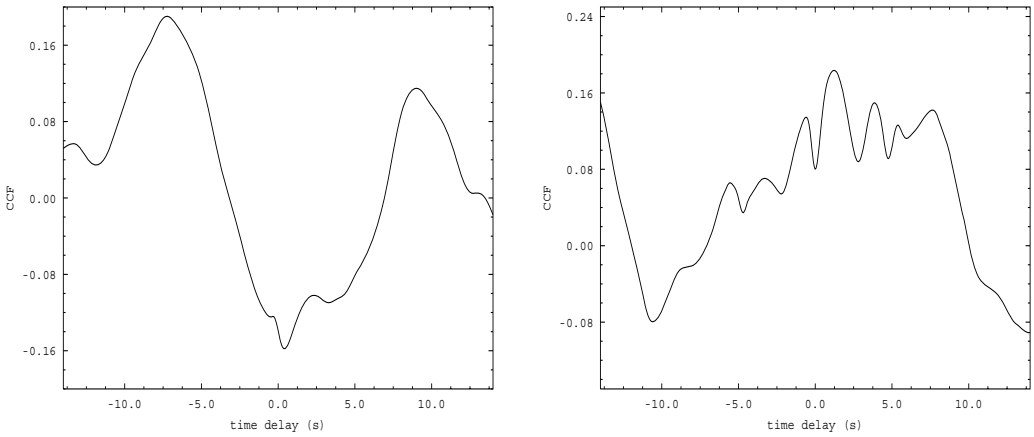

(c) central region (-0.27/2.26) (d) wall region (-0.65/1.27)

Figure 9.20: 2-D Riser: Cross-correlation of the voidage and gas pressure fluctuations at (a-b) 30.0 cm and (c-d) 80.0 cm above the bottom boundary (Table 9.1). The numbers in brackets represent, respectively, the negative and positive time-lag associated with the cross-correlation peaks near the zero time delay.

	Pc1-2D	Pw1-2D	Pc2-2D	Pw2-2D
D_{ML}	7.87	7.18	6.64	5.88
K_{ML}(bits/cycle)	5.61	6.80	4.69	5.35
	Pw3-3D	Pc4-3D	Pw4-3D	Vw4-3D
D_{ML}	9.01	7.69	7.25	4.89
K_{ML}(bits/cycle)	7.94	9.33	8.88	7.18

Table 9.4: Riser: Maximum likelihood estimation of the correlation dimension (D_{ML}) and Kolmogorov entropy (K_{ML}). P and V stand for pressure and voidage fluctuation, respectively, c and w represent central and wall regions and $1-4$ are 30.0, 80.0, 25.0 and 50.0 cm above the bottom boundary, respectively.

and inlet gas velocity, four regimes could be studied: multiple and single bubbling (with a constant inlet gas velocity), 'exploding bubble' (at low solid flux), and transport conditions (at large solid flux and large inlet gas velocity). They observed, in risers operating in the 'exploding bubble regime', i.e., with large voidages and under circulation conditions, a dominant frequency of approximately 1.3 Hz. Further small peaks were observed, however, they vanished in the region between 2.0 and 10.0 Hz. In flows operating in the transport regime, no dominant frequency was readily found, although a pronounced peak at 4.0 Hz was reported. Although the conditions used in the simulated 2-D and 3-D risers in this work are different from theirs, the overall behavior of the dominant frequencies found for the 2-D (Figure 9.9) and 3-D (Figures 9.18 and 9.19(a)) qualitatively agree, as the simulations performed here were conducted in a regime between the 'exploding bubble' and 'transport' regimes. The PSD of pressure fluctuations obtained from a detector placed at the central region and at 5.0 cm above the bottom boundary is shown in Figure 9.19(a). Periodic behavior can be observed, i.e., large peaks at every 0.5 Hz up to 6.5 Hz can be observed. Possible reasons for this periodic behavior include: a mass of particles passing through the center region due to either cluster collisions and bouncing off the wall, or low deflection by fresh particles that have just entered into the domain.

Although there are a number of advantages in using voidage measurements to in-

vestigate the hydrodynamics of dense and dilute flows, pressure measurements are more readily available from fluidization experiments. In dense flows, Sections 5.6 and 8.6, void fractions were used in the flow analysis through chaos theory. However in this chapter, pressure is used because it was found to be a more sensitive indicator of rapid regime changes and flow structures in dilute flows.

The cross-correlation function, CCF (see Section 5.6.2), is defined as a measure of the similarity between two different data sets: the input and output time series. It indicates the transfer function direction between the time series and the delay between input and output. The CCF of voidage and pressure fluctuations (Figure 9.20) indicates that between 0.27 and 0.65 seconds after a perturbation in pressure, a voidage perturbation occurs. However, as indicated by the negative CCFs peaks, feedback reactions from the output [141], i.e., voidage, are expected. The CCF of voidage and vertical solid velocities (Figure 9.21) shows that perturbations in voidage lead to velocity perturbations with a delay of approximately 0.10 seconds after a voidage perturbation, with no feedback reaction. This means that pressure fluctuations lead to voidage perturbations with possible feedback reactions. These voidages perturbations lead to oscillations in solid velocities.

The maximum likelihood estimation of the correlation dimension, D_{ML}, may be used as a measure of the complexity of the flow (see section 8.6), i.e., the lower the dimension, the less complex the macro-flow is. Johnsson *et al.* [113] reported that for turbulent flows or under turbulent-like conditions, the D_{ML} must be greater than 6.0. This agrees with the D_{ML} calculated for 2-D and 3-D risers, as indicated in Table 9.4.

The maximum likelihood estimation of the Kolmogorov entropy, K_{ML}, is a measure of the rate of information loss along the attractor, i.e., a measure of the degree of predictability of points along the attractor, given an arbitrary point [150]. Thus, the Kolmogorov entropy might be used to characterize the time-dependent behavior of fluidized beds [44]. Since it is associated with the complexity of the flow, the less complex the macroflow, the lower the K_{ML}. Johnsson *et al.* [113] reported that flows operating with large superficial gas velocities exhibit large K_{ML}. Their experiments showed that for turbulent flows or under turbulent-like conditions, the maximum likelihood estimation of the Kolmogorov entropy is above 5.0 bits/cycle. The results reported in Table 9.4 agreed with

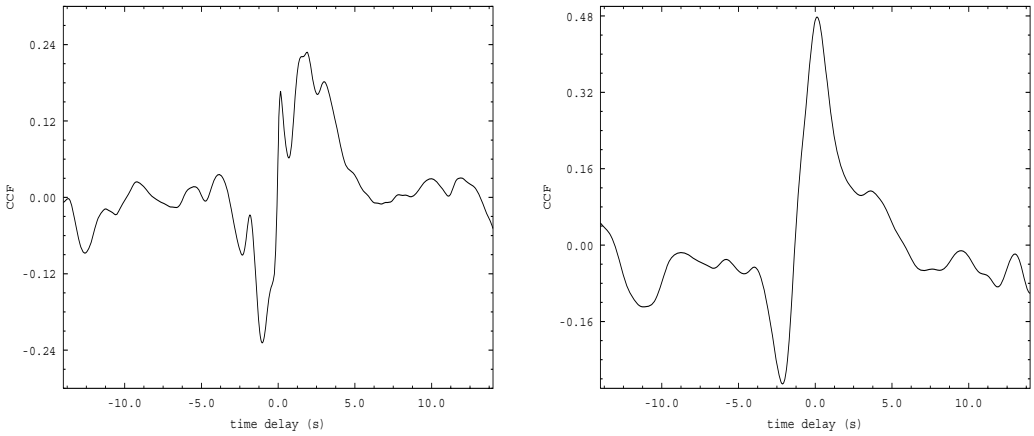

(a) central region (-1.85/0.14) (b) wall region (-3.98/0.11)

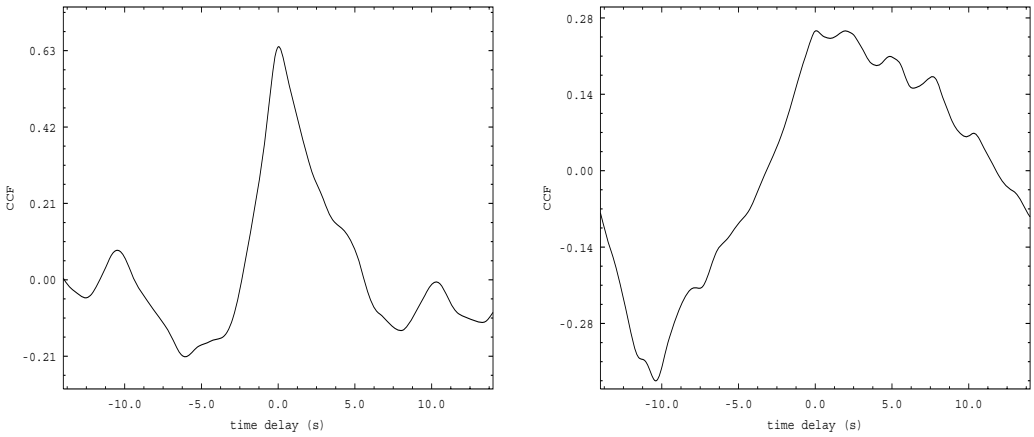

(c) central region (-4.26/0.036) (d) wall region (-6.06/0.039)

Figure 9.21: 2-D Riser: Cross-correlation of the voidage and vertical solid velocity fluctuations at (a-b) 30.0 cm and (c-d) 80.0 cm above the bottom boundary (Table 9.1). The numbers in brackets represent, respectively, the negative and positive time-lag associated with the cross-correlation peaks near the zero time delay.

their experimental results for both the 2-D and 3-D simulations, although an extremely large K_{ML} $(7.0 \leq K_{ML} \leq 9.33)$ was found in the 3-D simulations. This is possibly due to the coarse grid used in the simulations.

9.6 Conclusions

In this chapter, the flow dynamics of 2-D and 3-D risers in operational conditions is modelled by means of the Eulerian-Eulerian CFD code FLUIDITY. The conservative equations, i.e., continuity, momentum (for gas and solid phases) and fluctuation energy (for the granular phase), are solved. Space and time-dependent variables calculated are: solid volume fraction, granular temperature, velocities and pressure. The granular kinetic approach used here provides a means of modelling the dissipation of energy due to non-ideal particle-particle collisions.

Risers are characterized by annular flows in which relatively large particle concentrations $(0.01 \leq \varepsilon_s \leq 0.31)$ move, preferentially, near the wall region while in the core, a dilute particle-flow emulsion is observed. The velocity of particles in the core region are notably larger than those near to the wall. Near the wall, the particles may move upwards or downwards. Such motion may result in clusters of particles crashing into one another and moving towards the opposite wall. In this sense, energy dissipative parameters such as particle-particle and particle-wall restitution coefficients, play an important role, as they affect the collisions. The results obtained from 2-D and 3-D numerical simulations reported in this chapter qualitatively agree with experiments reported in the literature.

Massless particle tracers were continuously introduced into the bottom of the domain to investigate the mixing of particles during the numerical simulation. They have no effect on the dynamics and are used here only as a visualization tool. The particle paths are calculated by integrating from a starting point through the time-varying Eulerian velocity field. The splashing of particles into the walls were observed, as well as the spinning of the clusters during their upwards and downwards motion. In addition, the simulated cluster assumed random shapes when observed from horizontal and vertical cross-sections. In the vertical cross-section, a string-like ‘V’ shapes are observed whereas in the horizontal

cross-section, quarter-arc annular shapes were observed in the wall region and string-like shapes in the core region. These shapes agreed with those experimentally reported in the literature.

Finally, cross-correlation functions are used to establish the relationship between pressure and voidage fluctuations, as the former are more sensitive to changes in the flow macrostructure. Power spectra density, maximum likelihood estimations of correlation dimension and Kolmogorov entropy were used to characterize the flow regime and qualitatively compare the results with experiments from the literature.

Future work on risers will:

(1) implement and simulate the heat transfer in 3-D risers and validate the results with experiments and/or empirical correlations;

(2) improve the visualization technique applied to particle tracers in order to facilitate the observation of the particle mixing, and to establish the average residence time of particles as a function of the solid throughflow rates;

(3) conduct numerical simulation of lab-scale risers and investigate the mixing;

(4) extend the modelling to include chemical reactions and multisize particles.

Part IV

Conclusions

Chapter 10

Conclusions and Future Work

10.1 Conclusions

The main aim of this work is to model and investigate the heat and mass transfer in fluidized beds using the two-fluid granular temperature model. In order to achieve this aim, the set of conservative equations are solved using a high-resolution method which is globally second order accurate in space and time and the thermal effective conductivity is described as a function of the granular temperature. This ensures the consistency of the overall model which is based on the kinetic theory for dry granular flows.

This work consists of 9 chapters which describe the modelling of the heat and mass transfers in fluidized beds. In Chapter 2, the set of conservative equations that describe the multiphase flow are outlined. In addition, the closure laws that describe the density, rheology and thermal properties of the fluid and particle phases are summarized. The set of conservative and constitutive equations has been described in a number of fluid dynamics textbooks [39, 71, 70, 38], and may be summarized as follow:

(i) In gas-solid fluidization, the fluid phase is assumed compressible and behaving as an ideal gas. This assumption is valid for pressure and temperature conditions below the critical point;

(ii) The momentum transfer between the fluid and the solid phases is described by a hybrid expression in which for porosities lower 0.775 and larger than 0.825, the Ergun

equation [38] and the equation suggested by Wen & Yu [76] are used, respectively. In order to avoid discontinuities and sharp changes in the momentum transfer between the phases, a function was introduced in the region 0.775$<\varepsilon_f<$0.875, to smooth the curve;

(iii) In the model presented in this work, gas-phase turbulence has been neglected due to the uncertainty in turbulence model closures. Although the turbulence is important in the modelling of gas-particle flows, the model presented here performed well in the transient and in densely packed beds. However, this model may be largely improved using Sub-Grid Scale Model (SGS) [234] techniques that take into account small scale features such as gas and solid phases turbulences;

(iv) The interphase heat transfer coefficient was calculated through the Gunn correlation [56]. Although this expression is theoretically correct as it satisfies the asymptotic condition that the Nusselt number vanishes as the porosity tends to unity, an expression that takes into account particles collisions, such as the one suggested by Soo [39], may be introduced. Hence, such an expression, based on granular temperature would be entirely consistent with the overall model;

(v) Three expressions for the thermal conductivity coefficient $(\varepsilon_s\kappa_s)$ were tested in Chapter 3. One of them, used in [63, 34], calculates the $\varepsilon_s\kappa_s$ based on the physical properties of the emulsion of particles, whereas the other two expressions are based on the granular temperature. The main difference between the expressions based on granular temperature, Equations 2.27 and 2.29, relies on the formulation of Equation 2.29 in which the low-density and highly sheared flows may act in opposition. Hence, the influence of energy dissipation due to inelastic particle-particle and particle-walls collisions on the heat transfer may be taken into account. Although Equation 2.29 is more desirable than Equation 2.27, as it takes into account collisional effects, the numerical simulations show that it overestimates the energy dissipation as shown in Figures 3.4-3.7.

In Chapter 3, the heat transfer models in mono-disperse gas-solid fluidization are investigated and numerical results obtained from an empirical correlation and from an ex-

pression based on the kinetic theory of granular flows are compared with experiments. The simulations were conducted in 2-D geometries and focused on the heat transferred from a heated cylinder to the bed. The following conclusions may be drawn:

(i) The numerical results obtained from the standard (Equation 2.25) and the kinetic approaches (Equation 2.27) are very similar, however the kinetic approach is preferred as it is consistent with the overall two-fluid granular temperature model;

(ii) The heat transfer coefficients calculated from the numerical results match with experimental results obtained from the literature [235, 99] and with results obtained from experimental correlations (Equation 3.1);

(iii) The thermal energy model presented in this work was validated by comparing the time-dependent temperature obtained from a numerical simulation, performed over a long time period, with the analytical solution obtained from a simplified thermal energy equation. They showed good agreement and enhanced the confidence in the model;

(iv) Lower particle-particle restitution coefficients, i.e. more inelastic collisions, led to more vigorous fluidization as shown in Figures 3.15 and 3.16(b). Larger time-averaged bed heights, as observed in Section 3.4.1, are also a proof of the bed expansion due to a vigorous fluidization;

(v) Large solid concentrations may lead to low granular temperatures due to low particle agitation and relatively small particle mean free paths. However, low solid volume fractions $(\varepsilon_s < 0.01)$ do not lead to large granular temperatures as the probability of particle collisions is relatively low. Relatively low solid concentrations $(0.01 \leq \varepsilon_s \leq 0.31)$, however, result in large granular temperatures as reported in [10]. Thus, thermal energy is mainly transferred through the emulsion phase, as shown in Figures 3.12 and 3.13.

In Chapter 4, the wall-to-bed heat transfer is investigated using a solid phase effective thermal conductivity correlation based on granular temperature. The heat exchange in

the bubbles' wake is investigated by tracking the train of bubbles which rises along the heated wall of 2-D and 3-D fluidized beds. Large heat transfer coefficients were obtained in the rear region of bubbles due to relatively larger granular temperature there and intense particle circulation. The following conclusions may be drawn from this:

(i) In gas-solid fluidized beds, the thermal energy is preferentially conducted in the bubbles' wake. In this case, fresh particles were dragged into the wake of uprising bubbles, replacing hot particles and increasing the temperature gradient. Such replacement, which improved the solid circulation in the bubbles' wake, enhances the wall-to-bed heat transfer rates;

(ii) In highly packed regions, the heat transfer coefficient is small due to low granular temperatures, however, in dilute regions, i.e., in regions where the solid volume fraction is very low, the granular temperature is also low due to the low number of collisions. However, in the bubbles' wake, a relatively large solid concentration combined with large granular temperatures result in larger wall-to-bed heat transfer coefficients. The larger granular temperature and solid effective conductivity are also demonstrated by Hsiau [64, 67];

(iii) For 2-D simulations, time-averaged heat transfer coefficients of the order of 427 $W.m^{-2}.K^{-1}$ were found, whereas for 3-D simulations, the heat transfer coefficient was approximately 449 $W.m^{-2}.K^{-1}$. These results are in good agreement and although no reliable experimental data is available, local 2-D heat transfer coefficients reported by Kuipers *et al.* qualitatively agree with the snapshots shown in Figures 4.7, 4.9 and 4.21;

(iv) The results obtained in Chapters 3 and 4 enhance the confidence in the model proposed here. This motivates the performance of numerical simulations in more demanding high temperature and pressure conditions as those described in Chapters 5 and 7.

The dynamics of a conceptual nuclear fluidized bed is investigated in Chapter 5 in 2-D and 3-D geometries. In this chapter, a coupled high resolution multiphase gas-solid

Eulerian-Eulerian and neutron radiation model, simulated the deposition of heat energy into the nuclear fuel particles which were then cooled by the fluidizing helium gas. The excellent mixing properties of fluidized beds are shown in this system which results in the uniformity of the temperature distribution. The following conclusions may be drawn:

(i) The reactor can take over five minutes after startup to establish a quasi-steady state. It has been established that the low frequency oscillations observed in the power rate were caused by a heat loss (by the fluidizing helium) and heat generation (from nuclear fission);

(ii) It has shown that bubble generation and power are linked. The cross-correlation function (CCF) indicates that approximately 0.19 seconds after an increase in solid volume fraction, there is an increase in power in the bottom region near the wall region. As large bubbles rise, they travel upwards through the reactor, generating particle concentration waves. Such waves are responsible for negative time-delays;

(iii) The PSD of fission rate and voidage fluctuations indicate that power and bubbles are usually generated in the bottom corner region of the domain;

(iv) The flow regime in this system is characterized by changes between vigorous bubbling and slugging due to the strong mixing as large bubbles and power are generated in the bottom region of the bed;

(v) In order to help predict both the fission-power and temperature fluctuations, a simplified kriging interpolation was used to generate a surrogate fission-power time series. The dominant frequencies obtained from the PSD of the predicted surrogate and the original time series matches well. The gas temperature for both time series also agrees, this indicates that the simplified kriging interpolation is efficient and may accurately catch the underlying dynamics. In chaotic systems, as small perturbations in the input signal may lead to large effects in the output signal. Thus, this technique may be used to predict and, if necessary, to control the process parameters, such as temperature and pressure.

The vapor-liquid equilibria of water-steam is modelled in Chapter 6. In this chapter, the fluid phase is assumed compressible and the density is calculated from the hybrid experimental equation of state suggested by Haar *et al.* [173] and the cubic EOS due to Halbach & Chatterjee [174]. A numerical simulation involving water vaporization-condensation during the cooling of hot particles is conducted in Chapter 6. The following conclusions may be drawn:

(i) Water density decreases smoothly as the temperature and pressure rise;

(ii) Heat is mainly transferred by the hot particles that are displaced due to abrupt water vaporization (and further expansion), however boiling and condensing films resistance, which may have a large influence on the heat flux, was neglected in the present model and may be considered as a future work.

As a further application of the two-fluid model coupled with the phase change model, Chapter 7 describes the investigation of the dynamics of a coupled multiphase phase flow and neutron radiation problem in which spherical particles of a homogeneous mixture of Pu_{239} fissile isotope in SiO_2 and water. The simulations were performed with two initial over-pressures: 1.0 and 60.0 bars. The following conclusions may be outlined:

(i) As the system becomes super-critical, the release of energy raises the particle temperature, which rapidly vaporizes water, and so increases sharply the maximum gas pressure;

(ii) The hybrid equation of state, presented in Chapter 6, is robust and was successfully used in this 'tough' application, i.e., multiphase flow with rapid heating and phase changes.

The bubbles' shape and motion in gas-solid fluidized beds were investigated in Chapter 8. In addition, deterministic chaos theory was used to obtain the real dimensionality and to investigate flow regime. The following conclusions may be drawn:

(i) Due to the sharp solid concentration gradients in bubbling fluidized beds, a refined grid is necessary to achieve a reasonable convergence (i.e. the spatial solution be-

comes grid independent). Convergence of the mesh system may be determined through PSD of both voidage or pressure fluctuations;

(ii) The correlation dimension indicated that the system is chaotic with a low-order dimension of $\sim$1.8. Thus, at most 5 equations are necessary to describe the system, e.g, four equations for two components of velocity, in 2-D, for two phases, and one equation for the void fraction as already stated by Huillin *et al.* [43];

(iii) Bubbles are usually formed in the corners of the beds. This is due to the forces acting on the particles that are changing directions near the corners and creating regions of high vorticity. In a time-average sense, particles circulate by descending near the wall and ascending in the other regions of the column. Particles descend near the walls and rapidly change direction near the bottom of the bed, due to deceleration by the upstream gas flow. This 'flow collision' results in a circular/elliptical movement of both the gas and the particles;

(iv) In relatively wide fluidized beds in which wall effects on the bubbles' shape can be neglected, bubbles take the form of a hemisphere (see [11]). As a lower bubble accelerates vertically and enters the wake of the upper bubble, coalescence occurs [11].

The formation and breakup of clusters of particles in risers is investigated in Chapter 9. Power spectra density and the chaos theory are used to study flow regime and macrostructure in 'long'[1] numerical simulations both in 2-D and 3-D geometries. The conclusions are summarized a follows:

(i) Risers are characterized by annular flows in which relatively large particle concentrations $(0.01 \leq \varepsilon_s \leq 0.31)$ move, preferentially, near the wall region while in the core, the flow is mainly dilute $(\varepsilon_s < 0.01)$. The velocity of particles in the core region is larger than near to the wall. Near the wall, particles may move upwards or downwards and collide, being pushed towards the opposite wall. These flow behav-

[1] Long enough for a quasi-steady state regime to be reached.

ior characteristics are observed in the 2-D and 3-D numerical simulations performed here;

(ii) In dilute flows, lower particle-particle restitution coefficients lead to smaller energy dissipation, expressed by the time-averaged granular temperature (Figures 9.6 and 9.10);

(iii) The granular temperature is zero in a situation where there are no particles, however it increases as the particle concentration rises, and vanishes as the particle concentration reaches maximum particle packing. In this case, the mean free distance between the particles are smaller and thus the energy dissipation is lower;

(iv) The particles form string-like 'V' shape clusters, in the vertical cross-section. In the horizontal cross-section, however, rotating 'quarter arc' shapes in the wall region and a dilute string-like shapes in the core region were observed (Figures 9.12 and 9.13). These clusters shapes match with the shapes found in experiments available in the literature [224, 230, 231];

(v) Massless particle tracers were used as a visualization tool. These help observe the agglomeration of particles near the wall region and their subsequently motion upwards. In addition, particle clusters seem to spin up and down near the wall region, due to large velocities, and mix as the simulation evolves in time;

(vi) Cross-correlation functions are used to establish the relationship between pressure, void fraction and vertical solid velocities fluctuations as the former are more sensitive to changings in the flow macrostructure. Hence, it was observed that pressure fluctuations lead to voidage perturbations with possible feedback reactions, and voidages perturbations lead to oscillations in solid velocities. As these variables are strongly linked, dynamical analysis may be applied to any of them with no loss of information;

(vii) The maximum likelihood estimations of the correlation dimension and the Kolmogorov entropy obtained from pressure fluctuations of 2-D and 3-D simulations revealed that the riser flows are mainly turbulent or under turbulent like conditions.

10.2 Future Work

The author recommends that future work on fluidized beds should include:

1. Extend the model in order to take into account heat transfer due to radiation and chemical reactions;

2. Implement and simulate heat transfer of 3-D risers and validate with experiments and/or empirical correlations;

3. Improve the visualization technique applied to particle tracers to facilitate the particle mixing and establish the average residence time of particles as function of the solid throughflow rates;

4. Extend the model in order to take into account multisize particles flows;

5. Implement an equation of state for the solid phase, so that particles may melt, vaporize and deposit according to temperature and pressure;

6. Extend the model in order to take into account gas and solid turbulences in both large and small scales. Therefore, a submodel, such as the Sub-Grid Scale Model (SGS), in which small scales are taken into account may be incorporated in order to model turbulence that are important in dilute granular flows involving small particles at high velocities.

Appendix A

Derivation of the Simplified Analytical Model of the Thermal Energy Equation

A simplified model for the temperature field was obtained from the thermal energy equations (Eqn. 2.5-2.6). The analytical solution for this model was compared to the temperature field obtained from a numerical simulation as described in Section 3.3.

The thermal energy equation can be simplified to the following model:

$$\frac{d\left(\eta T_f\right)}{dt} + \psi\left(T_f - T^{(inl)}\right) = \Upsilon \tag{A.1}$$

with

$$\eta = \rho_s C_s V_s + \rho_f C_f V_f \qquad \text{and} \qquad \psi = \rho_f C_f v_f \overline{A}$$

where V_k and $\overline{A}$ are the volume of phase k and the cross-section area, respectively. Assuming that there is no source of energy, $\Upsilon = 0$, and defining φ as

$$\varphi = \frac{\psi}{\eta}$$

Hence, Eqn.A.1 can be rewritten as:

$$\frac{dT}{dt} + \varphi\left(T_f - T^{(inl)}\right) = 0 \tag{A.2}$$

By defining: $\hat{T} = T_f - T^{inl}$, Eqn.A.2 can be written as:

$$\frac{\partial \hat{T}}{\partial t} + \varphi\left(\hat{T}\right) = 0 \tag{A.3}$$

The analytical solution for this PDE is:

$$\hat{T} = \hat{T}^o \exp\left(-\varphi \Delta t\right)$$

substituting $\hat{T}$ into the above expression:

$$T = T^{(inl)} + \left(T^o - T^{(inl)}\right) \exp\left(\varphi \Delta t\right) \tag{A.4}$$

Appendix B

Contents of the CD-ROM

1. Eletronic version of this work;
2. Eletronic version of the articles submitted for publication and already published;
3. Animations of the following chapters:
   (a) Chapter 3: Heat transfer investigation in 2-D gas-solid fluidized beds;
   (b) Chapter 4: Heat transfer mechanisms in the wake of bubbles;
   (c) Chapter 5: Modelling coupled multiphase-flow and neutron-radiation;
   (d) Chapter 9: Mixing dynamics of particle clusters in risers.

Bibliography

[1] *Ullmann's Encyclopedia of Industrial Chemistry*. Wiley, 2003.

[2] Chaplin M. Water Structure and Behaviour. http://www.martin.chaplin.btinternet.co.uk/index.html.

[3] Lin J. S.; Chen M. M.; Chao B. T. A novel radioactive particle tracking facility for measurement of solids motion in gas fluidized beds. *AIChE Journal*, 31:465–473, 1985.

[4] Kunii D.; Levenspiel O. *Fluidization Engineering*. Butterworth-Heinemann Series Editor, 1991.

[5] Davidson J. F. *Fluidization*. Cambridge University Press, 1978.

[6] Thonglimp V. *Contribuition à l'étude Hydrodynamique des couches. Fluidisées par an gaz. Vitesse minimale de fluidization et expansion*. PhD thesis, Institut National Polytechnique, Toulouse, 1981.

[7] Crowe C.; Sommerfield M.; Tsuiji Y. *Multiphase Flows with Droplets and Particles*. CRC Press, 1998.

[8] Neri A.; Gidaspow D. Riser hydrodynamics: Simulations using kinetic theory. *AIChE Journal*, 46:52–67, 2000.

[9] Gidaspow D.; and Huilin L. Equation of state and radial distribution function of FCC particles in a CFB. *AIChE Journal*, 44:279–293, 1998.

[10] Huilin L.; Gidaspow D.; Bouillard J.;Wentie L. Hydrodynamics of binary fluidization in a riser: Cfd simulation using two granular temperatures. *Chemical Engineering Science*, 58:3777–3792, 2003.

[11] Pain C. C.; Mansoorzadeh S.; Gomes J. L. M. A.; de Oliveira C. R. E. A numerical investigation of bubbling gas-solid fluidized bed dynamics in 2-d geometries. *Powder Technology*, 128:56–77, 2002.

[12] Wirth K. E. Heat transfer in circulating fluidized beds. *Chemical Engineering Science*, 50 (13):2137–2151, 1995.

[13] Lim K. S.; Zhu J. X.; Grace J. R. Hydrodynamics of gas-solid fluidization. *International Journal of Multiphase Flow*, 21:141–193, 1995.

[14] Smith D. H.; Grimm U.; Haddad G. Composition and chemistry of particulates from tidd clean coal demonstration plant pressurized fluidized bed combustors, cyclone and filter vessel. *Proceedings of the International Ash Symposium*, Lexington, Kentucky, 1995.

[15] Sotudeg-Gharebaagh R.; Cheouki J.; Legros R. Natural gas combustion in a turbulent fluidized bed of inert particles. *Chemical Engineering Science*, 54:2029–2037, 1999.

[16] Kehlenbeck R.; Yates J.; Di Felice R.; Hofbauer H.; Rauch R. Novel scalling parameter for circulationg fluidized beds. *AIChE Journal*, 47(3):582–589, 2001.

[17] Kinoshita C. M.; Turn S. Q.; Overhend R. P.; Bain R. L. Power generation potential of biomass gaseification systems. *Journal of Energy Engineering*, 123:88–99, 1997.

[18] Han I. S.; Chung C. B. Dynamic modeling and simulation of a fluidized catalytic cracking process. *Chemical Engineering Science*, 56:1951–1990, 2001.

[19] Shreve R. N. *Chemical Process Industries*. McGraw-Hill, 1977.

[20] Kaneko Y.; Shiojima T.; Horio M. Dem simulation of fluidized beds for gas-phase olefin polymerization. *Chemical Engineering Science*, 54:5809–5821, 1999.

[21] Mortense M.; Minet R. G.; Tsotsis T. T.; Benson S. W. The development of a dual fluidized-bed reactor system for the conversion of hydrogen chloride to chlorine. *Chemical Engineering Science*, 54:2131–2139, 1999.

[22] Levenspiel O. *Chemical Reaction Engineering*. John Wiley and Sons, 1999.

[23] Huang S.; Wang Z.; Jin Y. Studies on gas-solid circulating fluidized bed reactors. *Chemical Engineering Science*, 54:2067–2075, 1999.

[24] Shook C. A.; Roco M. C. *Slurry Flow - Principles and Practice*. Butterworth-Heinemann, 1981.

[25] Christi M. Y. *Airlift Bioreactors*. Elsevier Applied Science, 1989.

[26] IEA Clean Coal Center. *Pressurized Fluidized Bed Combustion (PFBC)*. http://www.iea-coal.co.uk, 2000.

[27] Chandler A. J.; Eihmy T. T.; Hartlen J.; Hjelmar O.; Kosson D. S.; Sawell S. E.; van der Sloot H. A.; Vehlow J. *Municipal Solid Wasteincinerator and residues. The International Ash Working Group*. E;sevier Science, Amsterdam, 1997.

[28] Zhou H.; Abanades S.; Flamant; Gauthier D.; Lu J. Simulation of heavy metal vaporization dynamics in a fluidized bed. *Chemical Engineering Science*, 57:2603–2614, 2002.

[29] Werther J. Fluidization technology development - the industry/academia collaboration issue. *Powder Technology*, 113:230–241, 2000.

[30] Cundal P. A. A computer model for simulating progressive, large-scales moviments in block rock systems. *Proceedings of the Symposium of the International Society of Rock Mechanics*, 2(8), 1971.

[31] Strack O. D. L.; Cundal P. A. A discrete numerical model for granular assemblies. *Geotechnique*, 29:47–65, 1979.

[32] Tsuji Y.; Kawaguchi T. Discrete particle simulation of two dimensional fluidized bed. *Powder Technology*, 77:79–87, 1993.

[33] Wu Y.; Gidaspow D. Hydrodynamic simulation of methanol synthesis in gas-liquid slurry bubble column reactors. *Chemical Engineering Science*, 55:573–587, 2000.

[34] Schmidt A.; Renz U. Eulerian computation of heat transfer in fluidized beds. *Chemical Engineering Science*, 54:5515–5522, 1999.

[35] Schmidt A.; Renz U. Numerical prediction of heat transfer in fluidized beds by a kinetic theory of granular flows. *International Journal Therm. Sci.*, 39:871–885, 2000.

[36] Hu H. H. Direct simulation of flows of solid-liquid mixtures. *International Journal of Multiphase Flow*, 22:335–352, 1996.

[37] Drew D. A.; Passman S. L. *Theory of Multicomponent Fluids*. Springer-Verlag, 1998.

[38] Gidaspow D. *Multiphase Flow and Fluidization - Continuum and Kinetic Theory Descriptions*. Academic Press, 1994.

[39] Soo S. L. *Fluid Dynamics of Multiphase Systems*. Blaisdell Press, 1967.

[40] Kuipers J. A. M.; van Duin K. J.; van Beckum F. P. H. and van Swaaij W. P. M. A numerical model of gas-fluidized beds. *Chemical Engineering Science*, 47:1913–1924, 1992.

[41] Ding J.; Gidaspow D. A bubbling fluidization model using kinetic theory of granular flow. *AIChE Journal*, 36:523–538, 1990.

[42] Bai D.; Bi H. T.; Grace J. R. Chaotic behavior of fluidized beds based on pressure and voidage fluctuations. *AIChE Journal*, 43:1357–1361, 1997.

[43] Huilin L.; Gidaspow D.; Bouillard J. X. Dimension measurements of hydrodynamic attractors in circulating fluidized beds. *AIChE Symposium Series*, 91:103–111, 1995.

[44] van der Stappen M. L. M.; Schouten J. C.; van der Bleek C. M. Application of deterministic chaos theory in understanding the fluid dynamic behavior of gas-solids fluidization. *AIChE Symposium Series*, 89:91–102, 1993.

[45] Cassanello M.; Larachi F.; Marie M. N.; Guy C.; Chauki J. Experimental characterization of the solid phase chaotic dynamics in three phase fluidization. *Industrial Engineering Chemical Research*, 34:2971–2980, 1995.

[46] Tsonis A. *Chaos: From Theory to Applications*. Plenum Press, 1992.

[47] Anishchenko V. S. *Dynamical Chaos - Models and Experiments: Appearance Routes and Strutucture of Chaos in Simple Dynamical Systems*. World Scientific, 1995.

[48] Briggs K. Simple experiments in chaotic dynamics. *American Journal of Physics*, 55:1083–1089, 1987.

[49] Hilborn R. C. *Many dimensions and multifractals in chaos and nonlinear dynamics*. Oxford University Press, 1994.

[50] Small M.; Ya D.; Harrison R. G.; Clayton R.; Eftestol T.; Sunde K.; Steen P. A. Temporal evolution of nonlinear dynamics in ventricular arrhythmia. *International Journal of Bifurcation and Chaos*, 11:2531–2548, 2001.

[51] Moody; Darken. Fast learning in networks of locally-tuned processing units. *Neural Computation*, 1:281–294, 1989.

[52] R. Olea. *Geostatistics for engineers and earth scientists*. Kluwer Academic Publishers, 1999.

[53] Levenspiel O. Gas-solid reactor models: packed models, bubbling fluidised beds, turbulent fluidised beds and circulating (fast) fluidised beds. *Powder Technology*, 122:1–9, 2002.

[54] Khan A. R.; Elkamel A. Mathematical model for heat transfer mechanism for particulate system. *Applied Mathematics and Computation*, 129:295–316, 2002.

[55] Haid M.; Martin H.; Muller-Steinhagen H. Heat transfer to liquid-solid fluidized beds. *Chemical Engineering Science*, 33:211–225, 1994.

[56] Gunn D. J. Transfer of heat or mass to particles in fixed and fluidized beds. *International Journal of Heat and Mass Transfer*, 21:467–476, 1978.

[57] Molerus O. Heat transfer in gas fluidized beds - Part 1. *Powder Technology*, 70:1–14, 1992.

[58] Molerus O. Heat transfer in gas fluidized beds - Part 2: Dependence of heat transfer on gas velocity. *Powder Technology*, 70:15–20, 1992.

[59] Wasmund L.; Smith J. W. The mechanism of wall to fluid heat transfer in particulate fluidized beds. *The Canadian Journal of Chemical Engineering*, 43:246–251, 1965.

[60] Mickley H. S.; Fairbanks D. F. Mechanism of heat transfer to fluidized beds. *AIChE Journal*, 1:374–384, 1955.

[61] Molerus O.; Wirth K. E. *Heat Transfer in Fluidized Beds*. Chapman & Hall, 1997.

[62] Sunderesan S. R.; Clark N. N. Local heat transfer coefficients on the circumference of a tube in a gas fluidized bed. *International Journal Multiphase Flow*, 21:1003–1024, 1995.

[63] Kuipers J. A. M.; Prins W.; van Swaaij W. P. M. Numerical calculation of wall-to-bed heat-transfer coefficients in gas-fluidized beds. *AIChE Journal*, 38(7):1079–1091, 1992.

[64] Hsiau S. S. Effective thermal conductivities of a single species and a binary mixture of granular materials. *International Journal Multiphase Flow*, 26:83–97, 2000.

[65] Zeher P.; Schlunder E. U. Warmeleitfahigkeit von schttungen bei mßigen temperaturen. *Chimie Ing. Techn.*, 42(14):933–941, 1970.

[66] Hunt M. L. Discrete element simulations for granular material flows: Effective thermal conductivity and self-difusity. *International Journal Heat Mass Transfer*, 40:3059–3068, 1997.

[67] Hsiau S. S.; Hunt M. L. Kinetic theory analysis of flow-induced particle diffusion and thermal conduction in granular material flows. *Transactions of ASMEC: Journal of Heat Transfer*, 115:541–548, 1993.

[68] Natarajan V. V. R.; Hunt M. L. Kinetic theory analysis of heat transfer in granular flows. *International Journal Heat Mass Transfer*, 41:1929–1944, 1998.

[69] Oran E. S.; Boris J. P. *Numerical Simulation of Reactive Flow*. Cambridge University Press, 2001.

[70] Bear J.; Bachmat Y. *Introduction to Modeling of Transport Phenomena in Porous Media*. Kluwer Academic Press, 1991.

[71] Aris R. *Vectors, Tensors and the Basic Equations of Fluid Mechanics*. Prentice-Hall Inc., 1962.

[72] Jenkins J. T.; Savage S. B. A theory for the rapid flow of identical smooth, nearly elastic, spherical particles. *Journal of Fluid Mechanics*, 130:187–202, 1983.

[73] Gombosi T. I. *Gaskinetic Theory*. Cambridge University Press, 1994.

[74] Bouilard J. X.; Lyczkowski R. W.; Gidaspow D. Porosity distributions in a fluidized bed with an immersed obstacle. *AIChE Journal*, 35:908–922, 1989.

[75] van Wachem B. *Derivation, Implementation and Validation of Computer Simulation Models for Gas-Solid Fluidized Beds*. PhD thesis, Delft University of Technology, 2000.

[76] Wen C. Y.; Yu Y. H. Mechanics of fluidization. *Chem. Eng. Symp. Ser.*, 62:100–111, 1966.

[77] Rowe P. N. Drag forces in a hydraulic model of a fluidized bed, Part II. *Transactions Inst. Chem. Engs.*, 39:175–180, 1961.

[78] Pain C. C.; Mansoorzadeh S.; de Oliveira C. R. E.; Goddard A. J. H. Numerical modelling of gas-solid fluidized beds using the two-fluid approach. *International Journal of Numerical Methods in Fluids*, 36:91–124, 2001.

[79] Enwald H.; Peirano E.; Almstedt A. E. Eulerian two-phase flow theory applied to fluidization. *International Journal of Multiphase Flow*, 22:21–66, 1997.

[80] Jenkins J. T. Boundary conditions for rapid granular flow: flat, frictional walls. *Transactions ASME*, 59:120–127, 1992.

[81] Jackson R. The mechanics of fluidized beds - Part 1. *Transactions Inst. Chem. Eng.*, 41:13–21, 1963.

[82] Jackson R. The mechanics of fluidized beds - Part 2. *Transactions Inst. Chem. Eng.*, 41:22–48, 1963.

[83] Jenkins J. T.; Mancini F. Balance law and constitutive relation for plane flows of a dense, binary mixture of smooth, nearly elastic, circular disks. *Journal of Applied Mechanics*, 54:27–34, 1987.

[84] Jenkins J. T.; Mancini F. Kinetic theory for binary mixtures of smooth, nearly elastic, spherical particles. *Physics of Fluids A*, 1:2050–2057, 1989.

[85] Lun C. K. K.; Savager S. B.; Jefferey D. J.; Chepurniy N. Kinetic theories for granular flow: Inelastic particles in couette flow and slightly inelastic particles in a general flowfield. *Journal of Fluid Mechanics*, 140:223–256, 1984.

[86] Syamlal M.; Gidaspow D. Hydrodynamics of fluidization: prediction of wall to bed heat transfer coefficients. *AIChE Journal*, 31:127–135, 1985.

[87] Gomes J. L. M. A.; Pain C. C.; de Oliveira C. R. E.; Goddard A. J. H. Heat transfer models for gas-solid fluidized beds with internals. *Proceedings of the First MIT Conference on Computational Fluid and Solid Mechanics - Cambridge; USA*, pages 1194–1204, 2001.

[88] Bi H. T.; Ellis N.; Abba I. A.; Grace J. R. A state-of-art review of gas-solid turbulent fluidization. *Chemical Engineering Science*, 55:4789–4825, 2000.

[89] Yates J. G. Effects of temperature and pressure on gas-solid fluidization. *Chemical Engineering Science*, 51:167–205, 1996.

[90] Lettieri P.; Newton D.; Yates J. G. High temperature effects on the dense phase properties of gas fluidized beds. *Powder Technology*, 120:34–40, 2001.

[91] Lettieri P.; Brandini S.; Yates J. G.; Newton D. A generalization of foscolo and gibilaro particle-bed model to predict the fluid bed stability of some fresh fcc catalysts at elevated temperature. *Chemical Engineering Science*, 56:5401–5412, 2001.

[92] Foscolo P. U.; Gibilaro L. G. Fluid dynamic stability of fluidized suspensions. *Chemical Engineering Science*, 39:1485–1500, 1987.

[93] Leva M.; Grummer M.; Weintraub M.; Pollchik M. Introduction to fluidization. *Chemical Engineering Progress*, 44:511–520, 1948.

[94] Levenspiel O.; Walton J. S. Bed-wall heat transfer in fluidized systems. *Chemical Engineering Symposium Series*, 50:1–13, 1954.

[95] Wasan D. T.; Ahluwalia M. S. Consecutive film and surface renewal mechanism for heat and mass transfer from a wall. *Chemical Engineering Science*, 24:1535–1542, 1969.

[96] George A. H.; Smalley J. L. Instrumented cylinder for the measurement of instantaneous local heat flux in high temperature fluidized beds. *International Journal of Heat and Mass Transfer*, 34:3025–3036, 1991.

[97] Botterill J. S. M.; Williams J. R. The mechanism of heat transfer to gas fluidized beds. *Transactions of the Institute of Chemical Engineering*, 41:217–230, 1963.

[98] Gabor J. D. Wall to bed heat transfer in fluidized and packed beds. *Chemical Engineering Progr. Symp.*, 68:76–86, 1970.

[99] Mickley H. S.; Fairbanks D. F.; Hawthorn R. D. The relation between transfer coefficient and thermal fluctuations in fluidized bed heat transfer. *Chemical Engineering Prog. Symp. Ser.*, 57:51–60, 1961.

[100] Pain C. C.; Gomes J. L. M. A.; Eaton M. D.; de Oliveira C. R. E.; Goddard A. J. H.; Umpleby A. P. Numerical transport methods for multi-phase fluid flow and radiation modelling. *International Journal of Numerical Methods in Fluids*, Submitted, 2003.

[101] Schlichting H.; Kestin J. *Boundary-layer theory*. McGraw-Hill, 1968.

[102] Nguyen A. V.; Fletcher C. A. J. Particle interaction with the wall surface in two-phase gas-solid particle flow. *International Journal of Multiphase Flow*, 25:139–154, 1999.

[103] Goldschmidt M. J. V.; Kuipers J. A. M.; van Swaaij W. P. M. Hydrodynamic modelling of dense gas-fluidises beds using the kinetic theory of granular flow: effect of coefficient of restitution on bed dynamics. *Chemical Engineering Science*, 56:571–578, 2001.

[104] Salman A. D. Kharaz A. H., Gorham D. A. Accurate measurement of particle impact parameters. *Measurement Science and Technology*, 10:31–35, 1999.

[105] Balzer G. Gas-solid flow modelling based on kinetic theory of granular media: validation, applications and limitations. *Powder Technology*, 113:299–309, 2000.

[106] Noymer P. D.; Glicksman L. R. Cluster motion and particle-convective heat transfer at the wall of a circulated fluidized bed. *International Journal of Heat and Mass Transfer*, 41:147–158, 1997.

[107] Yates J. G.; Chessman D. J.; Sergeev Y. A. Experimental observations of voidage distribution around bubbles in a fluidized bed. *Chemical Engineering Science*, 49:1885–1895, 1994.

[108] Fan Z.;Chen G. T.;Chen B. C.;Yuan H. Analysis of pressure fluctuations in a 2d fluidized bed. *Powder Technology*, 62:139–145, 1990.

[109] Buyevich Y. A.;Yates J. G.;Chessman D. J.;Wu K. T. A model for the distribution of voidage around bubbles in a fluidized bed. *Chemical Engineering Science*, 50:3155–3162, 1995.

[110] Collins R. A model for the effects of the voidage distribution around a fluidization bubble. *Chemical Engineering Science*, 44:1481–1487, 1989.

[111] Pain C. C.; Gomes J. L. M. A.; Eaton M. D.; de Oliveira C. R. E.; Goddard A. J. H.; Umpleby A. P.; van Dam H.; van der Hagen T. H. J. J.; Lathouwers D. Space-dependent kinetics simulation of a gas-cooled fluidized bed nuclear reactor. *Nuclear Engineering and Design*, 219:225–245, 2003.

[112] Gomes J. L. M. A.;Pain C. C.;de Oliveira C. R. E.; Goddard A. J. H. An evaluation of two-fluid heat transfer models for gas-solid fluidized beds. *International Journal of Multiphase Flow*, Submitted, 2003.

[113] Johnsson F.; Zijerveld R. C.; Schouten J. C.; van der Bleek C. M.; Leckner B. Characterization of fluidization regimes by time-series analysis of pressure fluctuations. *International Journal of Multiphase Flow*, 26:663–715, 2000.

[114] van Dam H.; van der Hagen T.H.J.J.; Hoogenboom J.E.; Khotylev V.A.; Mudde R.F. Statics and dynamics of a fluidized bed fission reactor. *Proceedings of the International Conference of Emerging Nuclear Energy Systems*, pages 609–616, 1997.

[115] Gerwin H.; Scherer W. Treatment of the upper cavity in a pebble-bed high temperature gas-cooled reactor by diffusion theory. *Nuclear Science and Engineering*, 97:9–19, 1987.

[116] Gulden T. D.; Nickel H. Preface coated particle fuels. *Nuclear Technology*, 35:206–213, 1977.

[117] Golovko V.V.; Kloosterman J.L.; van Dam H.; van der Hagen T.H.J.J. Fuel particle design for a fluidized bed reactor. *Proceedings of Jahrestagung Kerntechnik '99, Annual meeting on nuclear technology '99*, pages 625–628, 1999.

[118] Sefidvash F. Status of the small modular fluidized bed light water nuclear reactor. *Nuclear Engineering Design*, 167:203–214, 1996.

[119] Hetrick D.L. *Dynamics of Nuclear reactors*. American Nuclear Society, 1993.

[120] Mather D.; Buckley A.; Prescott A. Critex - a code to calculate the fission release arising from transient criticality. *AEA Report CS/R1007/R*, 1994.

[121] Mather D.; Barbry F. Examination of some fissile solution scenarios using critex. *Proceedings of the Fourth International Conference on Nuclear Criticality Safety*, 1991.

[122] D.E. Kimpland R.H.; Korneich. A two-dimensional multi-region computer model for predicting nuclear excursions in aqueous homogeneous assemblies. *Nuclear Science and and Engineering*, 122:204–211, 1996.

[123] Yamamoto Y. Space-dependent kinetics analysis of a hypothetical array criticality accident involving units of aqueous uranyl fluoride. *Proceedings of the Fifth International Conference on Nuclear Criticality Safety*, pages 10–19, 1995.

[124] Rifat M.; Al-Chalabi R.M.; Turinsky P.J.; Faure F.X.;Sarsour H.N.; Engrand P.R. Nestle: A nodal kinetics code. *Transactions of the American Nuclear Society*, 68:432–433, 1993.

[125] Basoglu B.; Brewer R.W.; Haught C.F.; Hollenbach A.; Wilkenson A.D.; Dodds H.L.; Pasqua P. F. Simulation of hypothetical criticality accidents involving homogeneous damped low-enriched uo_2 powder systems. *Nuclear Technology*, 105:14–30, 1994.

[126] T.H.J.J. Golovko V.V.; Kloosterman J.L.; van Dam H.; van der Hagen. Investigation of a hypothetical start-up transient of a fluidized bed nuclear reactor. *Proceedings of Jahrestagung Kerntechnik 2000, Annual meeting on nuclear technology 2000*, 2000.

[127] Golovko V.V.; Kloosterman J.L.; van Dam H.; van der Hagen T.H.J.J. Analysis of transients in a fluidized bed nuclear reactor. *Proceedings of PHYSOR 2000*, 2000.

[128] Golovko V.V.; Kloosterman J.L.; van Dam H.; van der Hagen T.H.J.J. Dynamic core stability analysis of a fluidized bed nuclear reactor. *Proceedings of PHYSOR 2000*, 2000.

[129] Pain C.C.; de Oliveira C.R.E.; Goddard A.J.H.; Umpleby A.P. Transient criticality in fissile solutions - compressibility effects. *Nuclear Science and Engineering*, 138:78–95, 2001.

[130] A.J.H. de Oliveira C.R.E.; Pain C.C.; Goddard. The finite element method for time-dependent radiation transport applications. *Proceedings of the 1998 Radiation Protection and Shielding Topical Conference*, page 343, 1998.

[131] Pain C.C.; de Oliveira C.R.E.; Goddard A.J.H.; Umpleby A.P. Criticality behaviour of dilute plutonium solutions. *Nuclear Science and Technology*, 2001.

[132] Pain C.C.; de Oliveira C.R.E.; Goddard A.J.H. Non-linear space-dependent kinetics for criticality assessment of fissile solutions. *Progress in Nuclear Energy*, 39:53–114, 2001.

[133] Pain C.C.; Goddard A.J.H; de Oliveira C.R.E. Finite element transient criticality code fetch - verification and validation. *Proceedings of the Second NUCEF International Symposium on Nuclear Fuel Cycle*, 1998.

[134] Pain C. C.; Mansoorzadeh S.; de Oliveira C. R. E.; Goddard A. J. H. A study of bubbling and slugging fluidised beds using the two-fluid granular temperature model. *International Journal Multiphase Flow*, 27:527–551, 2001.

[135] Johnson P. C.; Jackson R. Frictional-collisional constitutive relations for granular materials with application to plane shearing. *Journal Fluid Mechanics*, 176:67–93, 1987.

[136] Samuelsberg A.; Hjertager B. H. An experimental and numerical study of flow patterns in a circulating fluidized bed reactor. *International Journal of Multiphase Flow*, 22:575–591, 1996.

[137] AEA Technology Report ANSWERS/WIMS. *WIMS8A: User Guide for Version*, 1999.

[138] Duderstadt J. J.; Hamilton L. J. *Nuclear reactor analysis*. Wiley, 1976.

[139] Leonard B. P. The ultimate conservative difference scheme applied to unsteady one-dimensional advection. *Computing Methods in Apllied Mechanics and Engineering*, 88:17–24, 1991.

[140] Baskakov A. P. ; Tuponogov V. G.; Filippovsky N. F. A study of pressure fluctuations in a bubbling fluidized bed. *Powder Technology*, 45:113–117, 1986.

[141] Yaffee R.A.; McGee M. *Introduction to Time Series Analysis and Forecasting with Applications of SAS and SPSS*. Academic Press, 2000.

[142] Yu D.; Lu W.; Harrison R. G. Space time index plots for probing dynamical nonstationarity. *Physical Letters A*, 250:323–327, 1998.

[143] Kantz H.; Schreiber T. *Nonlinear time series analysis*. Cambridge Univeristy Press, 2002.

[144] Kennel M. B. Statiscal test for dynamical nonstationary in observed time-series data. *Physical Review E*, 56:316–321, 1997.

[145] Schreiber T. Detecting and analyzing nonstationarity in a time series using nonlinear cross predictions. *Physical Review Letters*, 78:843–846, 1997.

[146] Casdagli M. C. Recurrence plots revisited. *Physica D*, 108:812–844, 1997.

[147] Schouten J. C.; van der Bleek C. M. *RCHAOS, A Menu Driven Software Package for Chaotic Time Series Analysis*. Reactor research Foundation, 1993.

[148] Grassberger P.; Procaccia I. Characterization of strange attractors. *Physical Review Letters*, 50:346–349, 1983.

[149] Schouten J. C.; Takens F.; van der Bleek C. M. Estimation of the dimension of a noisy attractor. *Physical Review E*, 50:1851–1861, 1994.

[150] Schouten J. C.; Takens F.; van der Bleek C. M. Maximum-likelihood estimation of the entropy of an attractor. *Physical Review E*, 49:126–129, 1994.

[151] I. Grassberger, P.; Procaccia. Estimation of the kolmogorov entropy from a chaotic signal. *Physica Review A*, 28:2591–2598, 1983.

[152] Platt J. A resource-allocating network for function interpolation. *Neural Computation*, 3:213–225, 1991.

[153] M. L. Stein. *Interpolation of Spatial Data: Some Theory for Kriging*. Verlag-Stein, 1999.

[154] Hegger R; Kantz H.; Schreiber T. Practical implementation of nonlinear time series methods: the tisean package. *Chaos*, 9:413–445, 1999.

[155] Oey R. S.; Mudde R. F.; Portela L. M.; van den Akker H. E. A. Simulation of a slurry airlift using a two-fluid model. *Chemical Engineering Science*, 56:673–681, 2001.

[156] Van den Akker H. E. A. Mudde R. F. 2d and 3d simulations of an internal airlift loop reactor on the basis of a two-fluid model. *Chemical Engineering Science*, 56:6351–6358, 2001.

[157] Meng A. X.; Hill G. A.; Dalai A. K. Hydrodynamic characteristics in an external loop airlift bioreactor containing a spinning sparger and a packed bed. *Industral and Chemicstray Engineering Research*, 41, 2002.

[158] Sajc L.; Obradovic B.; Vukovic D.; Bugarski B. Hydrodynamics and mass transfer in a four-phase, external loop air lift bioreactor. *Biotechnology Progress*, 11:420–428, 1995.

[159] Lauschke G.l; Gilles E. D. Circulating reaction zones in a packed-bed loop reactor. *Chemical Engineering Science*, 49:5359–5375, 1994.

[160] Dluska E.; Wroński S.; Hubacz R. Mass transfer in gas-liquid couette-taylor flow reactor. *Chemical Engineering Science*, 56:1131–1136, 2001.

[161] S.; Dluska E.; Hubacz R.; Molga E. Wroński. Mass transfer in gas liquid couette-taylor flow membrane reactor. *Chemical Engineering Science*, 54:2963–2967, 1999.

[162] Lu X.-X.; Boyes A. P.; Winterbottom J. M. Operating and hydrodynamic characteristics of a cocurrent downflow bubble column reactor. *Chemical Engineering Science*, 49:5719–5733, 1994.

[163] Becker S.; Sokolichin A.; Eigenberger G. Gas-liquid flow in bubble columns and loop reactors: Part 2. comparison of detailed experiments and flow simulations. *Chemical Engineering Science*, 49:5747–5762, 1994.

[164] Sokolichin A.; Eigenberger G. Gas-liquid flow in bubble columns and loop reactors: Part 1. detailed modelling and numerical simulation. *Chemical Engineering Science*, 49:5735–5746, 1994.

[165] Olmos E.; Gentric C.; Vial C.; Wild G.; Midoux N. Numerical simulation of multiphase flow in bubble column reactors. influence of bubble coalescence and break-up. *Chemical Engineering Science*, 56:6359–6365, 2001.

[166] Gidaspow D. Hydrodynamics models for slurry bubble column reactors - final report. *http://63.241.183.24/DOE/DOE_reports/94208/94208_toc.htm*, 1997.

[167] Clark N.N.; Flemmer R. L. C.; Van Egmond J. Non-newtonian two-phase circulation in bubble columns. *Canadian Journal of Chemical Engineering*, 67:862–865, 1989.

[168] Huang H. C.; Li Z. H.; Usmani A. S. *Finite Element Analysis of Non-Newtonian Flow : Theory and Software*. Springer-Verlag, 1999.

[169] Chhabra R. P.; Comiti J.; Machac I. Flow of non-newtonian fluidis in fixed and fluidised beds. *Chemical Engineering Science*, 56:1–27, 2001.

[170] Grund G.; Schumpe A.; Deckwer W.-D. Gas-liquid mass transfer in a bubble column with organic liquids. *Chemical Engineering Science*, 47:3509–3516, 1992.

[171] Muller F. L.; Davidson J. F. On the contributions of small bubbles to mass transfer in bubble columns containing highly viscous liquids. *Chemical Engineering Science*, 47:3525–3532, 1992.

[172] Merchuk J. C.; Ben-Zvi S. A novel approach to the correlations of mnass transfer rates in bubble columns with non-newtonian liquids. *Chemical Engineering Science*, 47:3517–3523, 1992.

[173] Haar L.; Gallagher J. S.; Kell G. *NBS/NRC Steam Tables - Thermodynamic and Transport Properties and Computer Programs for Vapor and Liquid States of Water in SI Units*. McGraw-Hill International Book Company, 1975.

[174] Halbach H.; Chatterjee N. D. An empirical Redlich-Kwong-type equation of state for ater to 1000^{o}C and 200 kbar. *Contributions to Mineralogy and Petrology*, 79:337–345, 1982.

[175] Callen H. B. *Thermodynamics and an Introduction to Thermostatistics*. John Wiley and Sons, 1985.

[176] Gibbs J. W. *Elementary Principles of Statistical Mechanics*. Ox Bow Press, 1981.

[177] Modell M.; Reid R. C. *Thermodynamics and Its Applications*. Prentice-Hall, Inc., 1983.

[178] Sandler S. I. *Chemical and Engineering Thermodynamics*. Wiley Series in Chemical Engineering, 1989.

[179] Smith J. M.; Van Ness H. C.; Abbott M. M. *Introduction to Chemical Engineering Thermodynamics*. McGraw-Hill, 2001.

[180] Gomes J. L. M. A. Modelagem Computacional do Equilíbrio Liquido-Vapor de Soluções Poliméricas usando uma Equação de Estado Cúbica. Master's thesis, Universidade do Estado do Rio de Janeiro, Instituto Politécnico, 1999.

[181] Gomes J. L. M. A.; Henderson L. N.; Guimaraes Rocha M. C. Modelling the vapor-liquid equilibrium of polymer solutions using a cubic equation of state. *Macromolecular Theory and Simulations*, 10:816–826, 2001.

[182] Henderson L. N.; de Oliveira Jr J. R.; Amaral Souto H. P.; Pitanga Marques R. Modeling and analysis of the isothermal flash problem and its calculation with the simulated annealing algorithm. *Industrial & Engineering Chemistry Research*, 40:6028–6038, 2001.

[183] Michelsen M. L. The isothermal flash problem: Stability. *Fluid Phase Equilibria*, 9:1–19, 1982.

[184] Michelsen M. L. The isothermal flash problem: Phase-split calculation. *Fluid Phase Equilibria*, 9:21–40, 1982.

[185] Chou G. F.; Praunitz J. M. A phenomenological correction to an equation of state for the critical region. *AIChE Journal*, 35:1487–1496, 1989.

[186] Jeffery C. A.; Austin P. H. A new analytic equation of state for liquid water. *Journal of Chemical Physics*, 110:484–496, 1999.

[187] Wiryana S.; Slutsky L.J.; Brown J. M. The equation of state of water to 200^{o}c and 3.5 gpa: model potentials and the experimental pressure scale. *Earth and Planetary Science Letters*, 163:123–130, 1998.

[188] Kirschen M; Pichavanti M. A thermodynamic model for hydrous sicate melting in system $NaAlSi_3O_8$-$KAlSi_3O_8$-SiP_4O_8-H_2O. *Chemical Geology*, 174:103–114, 2001.

[189] Pain C.C.; de Oliveira C.R.E.; Goddard A.J.H. Modelling the criticality consequences of free surface motion in fissile liquids. *Proceedings of the Second NUCEF International Symposium on Nuclear Fuel Cycle*, 1998.

[190] Chapman S.; Cowling T.G. *The Mathematical Theory of Non-Uniform Gases*. Cambridge University Press, 1970.

[191] de Oliveira C.R.E. An arbitrary geometry finite element method for multi-group neutron transport equation. *Progress in Nuclear Energy*, 18:227–238, 1986.

[192] Roth M. J. *The WIMS-E Module of W-PROC.* AEE Winfrith Report, 1980. AEEW-R 1365.

[193] Pain C.C.; Gomes J.L.M.A.; Eaton M.D.; de Oliveira C.R.E.; Goddard A.J.H.; Umpleby A.P. A model of heat transfer dynamics of coupled multiphase-flow and neutron-radiation: Application to a nuclear fluidized bed reactor. *International Journal of Computational Methods in Fluids*, Submitted, 2003.

[194] Davidson J.F. Symposium on fluidization-discussion. *Transactions Inst. Chem. Eng.*, 39:230–232, 1961.

[195] Jackson R. *Hydrodynamic stability of fluid-particle systems*. Academic Press, 1985.

[196] Pritchett J. W.; Blake T. R.; Garg S. K. A numerical model of gas fluidized beds. *AIChE Symposium Series*, 74:134–148, 1978.

[197] Gera D.; Gautam M.; Tsuji T.; Gawaguchi T.; Tanaka T. Computer simulation of bubbles in large-particle fluidized beds. *Powder Technology*, 98:38–47, 1998.

[198] Gidaspow D.; Ettehadieh B. Fluidization in two dimensional beds with a jet. Part II: Hydrodynamic modelling. *Industrial and Engineering Chemistry Fundamentals*, 22:193–201, 1983.

[199] Harris P. J. A numerical method for modelling the motion of a spherical bubble. *International Journal of Numerical Methods in Fluids*, 22:1125–1134, 1996.

[200] Richner D. W.; Minoura T.; Pritchett J. W.; Blake T. R. Computer simulation of isothermal fluidization in large-scale laboratory rigs. *AIChE Journal*, 36:361–369, 1990.

[201] Christie I.; Ganser G. H.; Wilder J. W. Numerical solution of a two dimensional fluidized bed model. *International Journal of Numerical Methods in Fluids*, 28:381–394, 1998.

[202] Gidaspow D. Hydrodynamics of fluidization and heat transfer: Super-computer modeling. *Applied Mechanics Review*, 39:1–23, 1986.

[203] Lyczkowski R. W.; Gamwo I. K.; Dorban V.; Ai Y. H.; Chao B. T.; Chen M.; Gidaspow D. Validation of computed solids hydrodynamics and pressure oscillations in a bubbling atmospheric fluidized bed. *Powder Technology*, 76:65–77, 1993.

[204] Savage S. B. *Granular flows at high shear rates. Theory of dispersed multiphase flow*. Academic Press, 1983.

[205] Shahinpoor M.; Ahmadi G. *A kinetic theory for the rapid flow of rough identical spherical particles and the evolution of fluctuation*. In Advances in mechanics and the flow of granular materials, II. Transactions Tech. Pub., 1983.

[206] Ocone R.; Astarita G. A pseudo-thermodynamic theory of granular flow rheology. journal of rheology. *Journal of Rheology*, 37:727–74, 1993.

[207] Cao J.; Ahmadi G. Gas-particle two-phase turbulent flow in a vertical duct. *International Journal of Multiphase Flow*, 21:1203–1228, 1995.

[208] Ryuji K.; Tsushi A.; Yoshida K. Chaotic characteristic of three-phase fluidization. *AIChE Symp. Series*, 92:60–65, 1996.

[209] Hay J. M.; Nelson B. H.; Briens C. L.; Bergougnou M. A. The calculation of the characteristics of a chaotic attractor in a gas-solid fluidized bed. *Chemical Engineering Science*, 50:373–380, 1995.

[210] Cody G. D.; Goldfarb D. J.; Storch Jr G. V.; Norris A. N. Particle granular temperature in gas fluidized beds, fluidization and fluid particle system. *AIChE Symposium Series*, 92:31–35, 1996.

[211] Geldart D. *Gas Fluidization Technology*. Wiley, 1986.

[212] Couderc J. P. *Fluidization*. Academic Press, 2 edition, 1985.

[213] Davies R. M.; Taylor G. I. The mechanics of large bubbles rising through extended liquids and through liquids in tubes. *Proceedings of the Royal Society of London. Series A: Mathematical and Physical Sciences*, 200:375–390, 1950.

[214] Takens F. Dynamical systems and turbulence. In L.S. Young D.A. Rand, editor, *Lecture Notes in Mathematics*, volume 898. Springer Verlag, 1981.

[215] Nguyen K.; Daw C. S.; Chakka P.; Cheng M.; Bruns D. D.; Finney C. E. A.; Kennel M. B. Spatio-temporal dynamics in a train of rising bubbles. *The Chemical Engineering Journal*, 65:191–197, 1996.

[216] Kersten S. R. A.; Prins W.; van der Drift B.;van Swaaij W. P. M. Principles of a novel multistage circulating fluidized bed reactor for biomass gasification. *Chemical Engineering Science*, 58:725–731, 2003.

[217] Lathouwers D.; Bellan J. Modelling of dense gas-solid reactive mixtures applied to biomass pyrolisis in a fluidized bed. *International Journal of Multiphase Flow*, 27:2155–2187, 2001.

[218] Chaouki J.; Gonzalez A.; Guy C. Klvana D. Two-phase model for a catalytic turbulent fluidized-bed reactor: application to ethylene synthesis. *Chemical Engineering Science*, 54:2039–2045, 1999.

[219] Davidson J. F. Circulating fluidised bed hydrodynamics. *Powder Technology*, 113:249–260, 2000.

[220] Kunii D.; Levenspiel O. The k-l reactor model for circulating fluidized beds. *Chemical Engineering Science*, 55:4563–4570, 2000.

[221] Harris A. T.; Davidson J. F.; Thorpe R. B. Influence of exit geometry in circulating fluidized-bed risers. *AIChE Journal*, 49:52–64, 2003.

[222] Hyre M.; Glicksman L. R. Particle dispersion and gas phase hydrodynamics in circulating fluidized beds. In *Proceedings of the 4th World Conference on Particle Technology*, Sydney, Australia, 2002.

[223] Glicksman L. R.; Moran J. C.; Hyre M. Gas phase turbulence in circulating fluidized beds. In *Proceedings of the 4th World Conference on Particle Technology*, Sydney,Australia, 2002.

[224] Tanaka T.; Noma K.; Ide Y.; Tsuji Y. Particle clusters formed in dispersed gas-solid flows: simulation and experiment. In *Proceedings of the 4th World Conference on Particle Technology*, Sydney, Australia, 2002.

[225] Namkung W.; Kim S. D. Radial gas mixing in a circulating fluidized bed. *Powder Technology*, 113:23–29, 2000.

[226] Fligner M.; Schipper P. H.; Sapre A. V.; Krambeck F. J. Two phase cluster model in riser reactors: impact of radial density distribution on yields. *Chemical Engineering Science*, 49:5813–5818, 1994.

[227] Malcus S.; Cruz E.; Rowe C.;Pugsley T. S. Radial solid mass flux profiles in a high-dispersion density circulating fluidized bed. *Powder Technology*, 125:5–9, 2002.

[228] Nieuwland J. J.; Huizenga P.; Kuipers J. A. M.; van Swaaij W. P. M. Hydrodynamic modelling of circulating fluidised beds. *Chemical Engineering Science*, 49:5803–5811, 1994.

[229] Helland E.; Occelli R.; Tadrist L. Computational study of fluctuating motion and cluster structures in gas-particle flows. *International Journal of Multiphase Flow*, 28:199–223, 2002.

[230] Horio M.; Kuroki H. Three dimensional flow visualization of dilutely dispersed solids in bubbling and circulating fluidized beds. *Chemical Engineering Science*, 49:2413–2421, 1994.

[231] Kwauk M. Li Y. The dynamics of fast fluidization in fluidization. In Grace R. and J. M. Matsen, editors, *Fluidization*, pages 537–544. Plenum, New York, USA, 1980.

[232] Marzocchella A.; Zijerveld R. C.; Scouten J. C.; van der Bleek C. M. Chaotic behavior of gas-solids flow in the riser of a laboratory-scale circulating fluidized bed. *AIChE Journal*, 43:1458–1468, 1997.

[233] van der Schaaf J.; Johnsson F.; Schouten J. C.; van der Bleek C. M. Fourier analysis of non-linear pressure fluctuations in gas-solids flow in cfb risers - observing solid strutures and gas/particles turbulence. *Chemical Engineering Science*, 54:5541–5546, 1999.

[234] Sagaut P. *Large Eddy Simulation for Incompressible Flows. An Introduction*. Springer, 2001.

[235] Sundaresan R.; Kolar A. K. Core heat transfer studies in a circulating fluidized bed. *Powder Technology*, 124:138–151, 2002.

Index